

MODELING OF RADIATIVE HEAT TRANSFER IN STRONGLY FORWARD
SCATTERING MEDIA OF BUBBLING FLUIDIZED BED COMBUSTOR
WITH AND WITHOUT RECYCLE

A THESIS SUBMITTED TO
THE GRADUATE SCHOOL OF NATURAL AND APPLIED SCIENCES
OF
MIDDLE EAST TECHNICAL UNIVERSITY

BY

ÖZGE ŞEN

IN PARTIAL FULFILLMENT OF THE REQUIREMENTS
FOR
THE DEGREE OF MASTER OF SCIENCE
IN
CHEMICAL ENGINEERING

AUGUST 2017

Approval of thesis:

**MODELING OF RADIATIVE HEAT TRANSFER IN STRONGLY
FORWARD SCATTERING MEDIA OF BUBBLING FLUIDIZED BED
COMBUSTOR WITH AND WITHOUT RECYCLE**

submitted by **ÖZGE ŞEN** in partial fulfillment of the requirements for the degree of **Master
of Science in Chemical Engineering Department, Middle East Technical University** by,

Prof. Dr. Gülbin Dural Ünver
Dean, Graduate School of **Natural and Applied Sciences**

Prof. Dr. Halil Kalıpçılar
Head of Department, **Chemical Engineering**

Assoc. Prof. Dr. Görkem Külah
Supervisor, **Chemical Engineering Dept., METU**

Prof. Dr. Nevin Selçuk
Co-Supervisor, **Chemical Engineering Dept., METU**

Examining Committee Members:

Prof. Dr. İlker Tarı
Mechanical Engineering Dept., METU

Assoc. Prof. Dr. Görkem Külah
Chemical Engineering Dept., METU

Prof. Dr. Murat Köksal
Mechanical Engineering Dept., Hacettepe University

Assoc. Prof. Dr. Serkan Kınca
Chemical Engineering Dept., METU

Asst. Prof. Dr. İnci Ayrancı
Chemical Engineering Dept., METU

Date: 14.08.2017

I hereby declare that all information in this document has been obtained and presented in accordance with academic rules and ethical conduct. I also declare that, as required by these rules and conduct, I have fully cited and referenced all material and results that are not original to this work.

Name, Last Name: Özge ŞEN

Signature:

ABSTRACT

MODELING OF RADIATIVE HEAT TRANSFER IN STRONGLY FORWARD SCATTERING MEDIA OF BUBBLING FLUIDIZED BED COMBUSTOR WITH AND WITHOUT RECYCLE

Şen, Özge

M.Sc., Department of Chemical Engineering

Supervisor: Assoc. Prof. Dr. Görkem Külâh

Co-Supervisor: Prof. Dr. Nevin Selçuk

August 2017, 123 pages

Predictive accuracy and CPU efficiency of geometric optics approximation (GOA) and scattering phase function simplifications in the freeboard of lignite-fired METU 0.3 MW_t ABFBC Test Rig were tested by applying them to the modeling of radiative heat transfer and comparing their predictions against measurements and benchmark solutions. The freeboard was treated as 3-D rectangular enclosure containing grey, absorbing, emitting gas with grey, absorbing, emitting, non/isotropically/anisotropically scattering particles surrounded by diffuse grey/black walls.

A three-dimensional radiation model based on Method of Lines (MOL) solution of Discrete Ordinates Method (DOM) coupled with Grey Gas (GG) for gases and Mie theory / GOA for fly ash particles in rectangular coordinates was extended for incorporation of anisotropic scattering by using normalized Henyey-Greenstein (HG) for the phase function. The input data required for the model and its validation were provided from the experimental data, which was previously taken from METU 0.3 MW_t ABFBC Test Rig operating with and without recycle of fine particles.

Assessment of GOA in terms of predictive accuracy reveals that applicability limit of GOA should be based on cumulative cross sectional area distribution rather than surface mean diameter or cumulative weight distribution of particles. From the

viewpoints of computational economy, GOA was found to improve CPU efficiency of the solution with increasing optical thickness.

Predictive accuracy and computational efficiency of scattering phase function simplifications were tested by comparing their predictions with those of forward scattering with HG. Comparisons reveal that phase function simplifications have insignificant effect on incident heat fluxes whereas source terms were found to be sensitive to phase function simplifications and the sensitivity increases with increasing optical thickness. Improvement in CPU efficiency of phase function simplifications is observed in only combusting systems involving high particle loads; however, in those systems, accurate representation of particle scattering that is forward scattering is vital.

Keywords: MOL solution of DOM, Particle radiation, Geometric optics approximation, Anisotropic scattering, Normalized Henyey Greenstein phase function, Bubbling Fluidized Bed Combustor.

ÖZ

KUVVETLİ İLERİ SAÇINIMLI ORTAM İÇEREN GERİ ÇEVİRİMLİ VE ÇEVİRİMSİZ KABARCIKLI AKIŞKAN YATAKLI YAKICIDA IŞINIM ISI AKTARIMININ MODELLENMESİ

Şen, Özge

Yüksek Lisans, Kimya Mühendisliği Bölümü

Tez Yöneticisi: Doç. Dr. Görkem Külâh

Ortak Tez Yöneticisi: Prof. Dr. Nevin Selçuk

Ağustos 2017, 123 sayfa

Geometrik optik yaklaşımının ve saçılım faz fonksiyonu basitleştirmelerinin linyit kömürü yakan 0.3 MW_t ODTÜ atmosferik kabarcıklı akışkan yataklı yakıcının serbest bölgesinde öngörme doğruluğu ve hesaplama verimliliği açısından test edilmesi için, geometrik optik yaklaşımı ve saçılım faz fonksiyonu basitleştirmeleri ışınım ısı aktarımını modellemek için uygulanmış ve ürettikleri öngörüler ölçümlerle ve kıyaslama çözümlerle karşılaştırılmıştır. Bu modelde, serbest bölge, üç boyutlu, dikdörtgen şeklinde, gri ve siyah yüzeylerle çevrelenmiş; gri, soğuran, yayan gaz ve gri, soğuran, yayan ve izotropik /izotropik olmayan saçılım yapan ya da saçılım yapmayan parçacıklar olarak muamele edilmiştir.

Belirli yönler yönteminin çizgiler yoluyla çözümünün gazlar için gri gaz ve uçan kül parçacıkları için Mie teori ve geometrik optik yaklaşımı ile birleşimine dayanan kartezyen koordinatlarındaki üç boyutlu ışınım modeli, normalize edilmiş Henyey Greenstein faz fonksiyonu kullanılarak izotropik olmayan saçılım ile birleştirilerek genişletilmiştir. Modelleme ve model verilerini doğrulama için gerekli girdi verileri, geri çevrimli ve çevrimsiz olarak çalışan ODTÜ 0.3 MW_t atmosferik kabarcıklı akışkan yataklı yakıcıdan daha önce alınmış deneysel verilerden sağlanmıştır.

Geometrik optik yaklaşımının öngörme doğruluğunun değerlendirmesi, geometrik optik yaklaşımının uygulanabilirlik limitinin parçacıkların yüzey ortalama çapına ya

da toplam ağırlık dağılımına dayanmaktansa, parçacıkların toplam kesit alanı dağılımına dayanması gerektiğini göstermiştir. Geometrik optik yaklaşımının artan optik kalınlıkla birlikte hesaplama verimliliğini arttırdığı bulunmuştur.

Saçılım faz fonksiyonu basitleştirmelerinin öngörme doğruluğu ve hesaplama verimliliği açısından test edilmesi için, saçılım faz fonksiyonu basitleştirmelerinin ürettikleri öngörüler Henyey Greenstein faz fonksiyonu kullanılarak ileri saçılım yapan öngörülerıyla karşılaştırılmıştır. Karşılaştırmalar, faz fonksiyonu basitleştirmelerinin serbest bölge duvarlarına gelen ısı akısına etkisinin önemli ölçüde olmadığını ama kaynak teriminin faz fonksiyonu basitleştirmelerine hassas olduğunu ve bu hassasiyetin artan optik kalınlıkla birlikte arttığını göstermiştir. Saçılım faz fonksiyonu basitleştirmelerinin sadece yüksek parçacık yüklü yanma sistemlerinde hesaplama verimliliğini arttırdığı gözlenmiştir ancak bu sistemlerde parçacık saçılımının doğru temsil edilmesi, ileri saçılım, önemlidir.

Anahtar kelimeler: Belirli yönler yönteminin çizgiler metoduyla çözümü, Parçacık ışınlama, Geometrik optik yaklaşımı, İzotropik olmayan saçılım, Normalize edilmiş Henyey Greenstein faz fonksiyonu, Kabarcıklı akışkan yataklı yakıcı.

To my precious family

ACKNOWLEDGEMENTS

I would like to express my deepest gratitude to my co-supervisor Prof. Dr. Nevin Selçuk for her guidance, advices and encouragement throughout the development of this study. I also would like to thank to my supervisor Assoc. Prof. Dr. Görkem Külâh for her precious discussions, comments and supports during the progress of this work.

Special thanks to Cihan Ateş for his friendship, unquestioning support, encouragement and utmost contributions till the end. His knowledge and experience are very valuable during this study and my entire graduate study.

I owe my particular and lovely thanks to my beloved friends Nazlı Bülbül, Ayça Karatepe, İpek Çınar, Salim Şimşek and Volkan Işık for their precious friendship and moral supports. They are always with me whenever I needed.

I would like to thank to Berrak Erkmen, Merve Sarıyer and Özge Batır for their motivation and advices they provided. I am also thankful for them to being always together and trying to overcome all problems together during all the study. I would also like to thank to Merve Özkutlu and Fatma Şahin Çakanyıldırım for their precious supports for completion of the study.

Last but not the least, I would like to present my sincerest thanks to my mom, Ayşegül Şen, my dad, Haluk Şen, and my lovely sister, Gökçe Şen, for their unconditional love, encouragement and endless support over my whole life. They are the best and I owe so much to them. Without them, I could not be the person I am right now. Thank you for everything...

TABLE OF CONTENTS

ABSTRACT	v
ÖZ.....	vii
ACKNOWLEDGEMENTS	x
TABLE OF CONTENTS	xi
LIST OF TABLES	xiv
LIST OF FIGURES.....	xvi
LIST OF SYMBOLS	xviii
CHAPTERS	
1. INTRODUCTION.....	1
2. THE METHOD OF LINES SOLUTION OF DISCRETE ORDINATES METHOD.....	15
2.1. Radiative Transfer Equation.....	15
2.2. Discrete Ordinates Method.....	18
2.2.1. Parameters Affecting Accuracy of DOM.....	20
2.3. Method of Lines Solution of Discrete Ordinate Method.....	24
2.3.1. Parameters Affecting Accuracy of MOL Solution of DOM.....	25
2.4. Structure and Operation of Computer Code.....	27
3. RADIATIVE PROPERTY ESTIMATION TECHNIQUES	33
3.1. Property Estimation of Gases	33
3.1.1. Grey Gas Model	34
3.2. Property Estimation of Grey Particles.....	34

3.2.1. Mie Theory	34
3.2.2. Geometric Optics Approximation (GOA)	39
3.2.3. Scattering Phase Function and Its Normalization	42
3.2.3.1. Scattering Phase Function Approximations	44
3.2.3.2. Scattering Phase Function Normalization Techniques	51
4. 0.3 MW _t METU ABFBC TEST RIG	57
4.1. Description of the Test Rig	57
4.2. Operating Conditions	60
4.3. Approximation of the Freeboard as a 3 – D Radiation Problem	66
4.4. Input Data for the Radiation Model	70
5. RESULTS AND DISCUSSION	73
5.1. Angular and Spatial Discretization Refinement	74
5.2. Validation of the Model against Experimental Data	82
5.3. Assessment of Accuracy of Scattering Phase Function Simplifications	89
6. CONCLUSIONS	95
6.1. Suggestions for Future Work	97
REFERENCES	99
APPENDICES	
A. ORDINATES AND WEIGHTS FOR S _N APPROXIMATION	111
B. CALCULATION OF ABSORPTION COEFFICIENT OF GASES USING LECKNER'S CORRELATIONS	113
C. TABULATED SIZE DISTRIBUTIONS OF SOLID STREAMS	115
D. CALCULATION OF PARTICLE REFLECTIVITY USING FRESNEL'S RELATIONS	119
E. SCATTERING REGIME MAP FOR INDEPENDENT AND DEPENDENT SCATTERING	121

F. INITIAL PARAMETERS FOR THE ODE SOLVER (ROWMAP)	
SUBROUTINE.....	123

LIST OF TABLES

TABLES

Table 2.1 Total number of discrete directions used for S_N approximation	22
Table 2.2 Spatial differencing schemes.....	26
Table 4.1 Characteristics of Beypazarı Lignite	60
Table 4.2 Operating conditions of the experiments	62
Table 4.3 Properties of fly ash streams	63
Table 4.4 Fly ash compositions.....	63
Table 4.5 Polynomials for temperature profiles	65
Table 4.6 Radiative properties of the surrounding surfaces	66
Table 4.7 Input data for calculation of radiative properties of the participating combustion gases.....	68
Table 4.8 Radiative properties of the gases.....	69
Table 4.9 Radiative properties of the fly ash particles predicted by Mie theory....	70
Table 4.10 Radiative properties of the fly ash particles predicted by GOA	70
Table 4.11 Input data for radiation model with Mie theory	71
Table 4.12 Input data for radiation model with GOA	72
Table 5.1 Effect of angular discretization on predictive accuracy and CPU efficiency for test case 2 at spatial grid of 5x5x35.....	76
Table 5.2 Effect of spatial discretization on predictive accuracy and CPU efficiency for test case 2.....	79
Table 5.3 Effect of angular discretization on predictive accuracy and CPU efficiency for test case 2 at spatial grid of 13x13x96.....	81
Table 5.4 Incident radiative heat fluxes on freeboard side walls for test case 1 and test case 2.....	84
Table 5.5 Effect of GOA on incident heat fluxes and source terms for test case 1 and test case 2.....	87

Table 5.6 Effect of phase function simplifications on incident heat fluxes and source terms for test case 1 and test case 2.....	93
Table A.1 Discrete ordinates for the S_N approximation for 3-D geometry.....	111
Table A.2 Discrete ordinates for the S_N approximation for 3-D geometry (cont'd)	112
Table B.1 Leckner's correlation constants for water vapor and carbon dioxide..	114
Table C.1 Size distribution of cyclone ash of test case 1	115
Table C.2 Size distribution of baghouse filter ash of test case 1	116
Table C.3 Size distribution of cyclone ash of test case 2.....	117
Table C.4 Size distribution of baghouse filter ash of test case 2	118
Table F.1 Initial parameters utilized for ROWMAP subroutine for the system under consideration	123

LIST OF FIGURES

FIGURES

Figure 1.1 Possible ways of scattering from a large particle.....	3
Figure 1.2 Schematic view of isotropic and anisotropic scattering.....	8
Figure 2.1 Rectangular coordinate system	17
Figure 2.2 Orders of approximation	21
Figure 2.3 Flowchart for MOLSDOM - AESM.....	30
Figure 2.4 Algorithm of the subroutine DERV_RAD	31
Figure 3.1 Phase function for linear anisotropic scattering.....	45
Figure 3.2 Polar plot for linear anisotropic scattering.....	46
Figure 3.3 Henyey-Greenstein phase function	50
Figure 4.1 Flow sheet of 0.3 MW _t METU ABFBC Test Rig.....	59
Figure 4.2 Particle size distribution for test case 1 and test case 2	62
Figure 4.3 Temperature profiles along the freeboard for (a) test case 1 and (b) test case 2	64
Figure 4.4 Treatment of freeboard as a 3-D enclosure and solution domain	67
Figure 5.1 Effect of angular discretization on (a) incident wall heat flux and (b) source term predictions for test case 2	75
Figure 5.2 Comparison of average relative % error in source term predictions for test case 2 at spatial grid of 5x5x35	76
Figure 5.3 Effect of spatial discretization on (a) incident wall heat flux and (b) source term predictions for test case 2.....	78
Figure 5.4 Effect of angular discretization on (a) incident wall heat flux and (b) source term predictions for test case 2	80
Figure 5.5 Comparison of average relative % error in source term predictions for test case 2 at different spatial grids	81

Figure 5.6 Measured and predicted incident radiative heat fluxes for (a) test case 1 and (b) test case 2	83
Figure 5.7 Effect of utilizing GOA as particle property model on radiative energy source term for (a) test case 1 and (b) test case 2.....	86
Figure 5.8 Applicability of GOA limit based on cumulative cross sectional area for test case 1 and test case 2	88
Figure 5.9 Cumulative particle size distribution for test case 1 and test case 2.....	89
Figure 5.10 Effect of phase function simplifications on incident heat fluxes for (a) test case 1 and (b) test case 2.....	91
Figure 5.11 Effect of phase function simplifications on radiative source terms for (a) test case 1 and (b) test case 2	92
Figure E.1 Scattering regime map for independent and dependent scattering.....	121

LIST OF SYMBOLS

a	radius of the spherical particle
a_n	Mie scattering coefficient, (-)
A	forward scattering normalization factor
A_c	total cross sectional area of the particles, ()
B	particle load, (kgm^{-3})
B	backward scattering normalization factor
B_i	mass retained in sieve i , (kg)
b_n	Mie scattering coefficient, (-)
C	cross-section
D	logarithmic derivative
d_p	particle diameter
e_i	unit vector in the coordinate direction i , (-)
E	error due to numerical smearing
E_s	scattered energy
f	forward scattering fraction, (-)
g	asymmetry factor
g'	expansion coefficient, (-)
G	incident radiation, (Wm^{-2})
I	radiative intensity, ($\text{Wm}^{-2}\text{sr}^{-1}$)

I_b	black-body intensity, ($\text{Wm}^{-2}\text{sr}^{-1}$)
J_1	1 st order Bessel function, (-)
k	imaginary part of complex refractive index, (-)
k_t	time constant, (m/s) ⁻¹
L	total number of directions in an ordinate, (-)
L_m	mean beam length, (m)
m	complex refractive index, (-)
M	order of approximation in delta–M phase function, (-)
M	total number of ordinates, (-)
\mathbf{n}	unit normal vector, (-)
n	order of accuracy of the chosen spatial differencing scheme, (-)
n	real part of complex refractive index, (-)
N	order of approximation of S_N angular quadrature scheme, (-)
$n(d_p)$	particle size distribution function
NB	number of wide bands for particles, (-)
ND	number of octants, (-)
NM	number of ordinates specified by the order of angular quadrature, (-)
NX, NY, NZ	number of nodes along x, y and z directions, (-)
P	pressure, (bar)
P_n	Legendre polynomial of degree n, (-)
\mathbf{q}	radiative heat flux, (Wm^{-2})
q^+	incoming wall heat flux, (Wm^{-2})
q^-	leaving wall heat flux, (Wm^{-2})

Q_{abs}	absorption efficiency, (-)
Q_{ext}	extinction efficiency, (-)
Q_{scat}	scattering efficiency, (-)
\mathbf{r}	position vector, (-)
t	time
T	total number of particle sizes under consideration, (-)
T	temperature, (K)
TF	final time of integration, (s)
TP	print interval, (s)
w	quadrature weight, (-)
x	size parameter, (-)
x, y, z	cartesian coordinates, (m)

Greek symbols

α	absorptivity, (-)
β	extinction coefficient, (m^{-1})
ε	emissivity, (-)
ϵ	error tolerance, (-)
η	direction cosine in y, (-)
θ	polar angle, (rad)
Θ	scattering angle, (rad)
κ	absorption coefficient, (m^{-1})
λ	wavelength, (μm)

μ	direction cosine in x, (-)
ξ	direction cosine in z, (-)
ξ_n	Ricatti-Bessel function
ψ_n	Ricatti-Bessel function
ρ	reflectivity, (-)
ρ_{\perp}	normal reflectivity, (-)
$\bar{\rho}$	average reflectivity, (-)
ρ_p	particle density, (kgm^{-3})
σ	Stefan-Boltzmann constant = 5.67×10^{-8} ($\text{Wm}^{-2}\text{K}^{-4}$)
σ_s	scattering coefficient, (m^{-1})
τ	optical thickness, (-)
τ_g	transmissivity of gas, (-)
ϕ	azimuthal angle, (rad)
Φ	scattering phase function, (sr^{-1})
Φ^*	approximated scattering phase function, (sr^{-1})
ω	single scattering albedo, (-)
Ω	direction of radiation intensity, (-)
$d\Omega$	solid angle, (sr)
Ω_m	ordinate direction, (-)

Subscripts

abs	absorption
D	diffraction

ext	extinction
g	gas
HG	Henyey – Greenstein function
ℓ'	incoming discrete direction
ℓ	index for a discrete direction
ℓ'^-	discrete backward direction
LA	modified parameter in linear anisotropic approximation
m	medium
m	ordinate index
m'	incoming ordinate
NS	numerical smearing
p	particle
r	radiative
R	reflection
s	scattering
scat	scattering
tr	modified parameter in transport approximation
w	wall
δE	modified parameter in delta – Eddington approximation
δM	modified parameter in delta – M approximation
'	incoming

Superscripts

m	ordinate index
m'	incoming ordinate
'	incoming

Abbreviations

1-D	One-Dimensional
2-D	Two-Dimensional
3-D	Three-Dimensional
6-D	Six-Dimensional
ABFBC	Atmospheric Bubbling Fluidized Bed Combustor
CFBC	Circulating Fluidized Bed Combustor
CFD	Computational Fluid Dynamics
DDS	Diamond Differencing Scheme
DOM	Discrete Ordinates Method
DSS012	Two-Point Upwind Differencing Scheme
DSS014	Three-Point Upwind Differencing Scheme
FBC	Fluidized Bed Combustion
FC	Fixed Carbon
FDM	Finite Difference Method
GG	Grey Gas
GOA	Geometric Optics Approximation
HG	Henyeey-Greenstein
LHV	Lower Heating Value

MC	Monte Carlo
MOL	Method of Lines
ODE	Ordinary Differential Equation
PDE	Partial Differential Equation
PSD	Particle Size Distribution
RSS	Root-Sum-Squares
RTE	Radiative Transfer Equation
SLW	Spectral Line-Based Weighted Sum of Grey Gases
VM	Volatile Matter
WSGG	Weighted sum of Grey Gases

CHAPTER 1

INTRODUCTION

In Turkey there exist widely spread lignite reserves with an estimated total quantity of 15.6 billion tons [1]. A major proportion of this quantity is characterized by high moisture, sulfur and ash contents with low calorific value. Moreover, ash fusion temperatures of these lignites are significantly lower than those of higher rank coals resulting in slagging at high operating temperatures (1200-1500°C) typical of conventional combustion systems such as pulverized fuel-firing systems. On the other hand, fluidized bed combustion (FBC) systems with lower operating temperatures (750-950°C) not only alleviates slagging problem but also provides in-situ desulfurization by addition of limestone leading to lower SO_x and NO_x emissions. Therefore, FBC technology offers the industry and utilities an alternative method of utilizing indigenous lignite in an efficient and environmentally acceptable manner as confirmed by the results of extensive research carried out on combustion and in-situ desulfurization characteristics of these lignites in pilot scale fluidized bed combustors [2-16].

Technical, economical and environmental feasibility of FBC technology together with its fuel flexibility have led to steady increase in its commercial use over the past decades. Increasing number of fluidized bed combustor installations has necessitated development of mathematical models for improvement of thermal and emission performances over a broad range of operating conditions. Modeling of fluidized bed combustors has mainly focused on heat transfer in the bed section since this region is the dominant source where heat of combustion is liberated.

However, it was found that the contribution of freeboard region to total heat transfer in fluidized bed combustors was of comparable magnitude to that of the bed region and the radiation of particle laden combustion gases constitutes major portion of heat transfer due to the presence of higher particle loads in freeboard [17-19].

Therefore, modeling of radiative heat transfer in such systems is of considerable importance and necessitates not only accurate but also computationally efficient methods for (i) solution of radiative transfer equation (RTE) in conjunction with the time dependent conservation equations for mass, momentum, energy, and chemical species and (ii) radiative property estimation of particle laden combustion gases. The computational effort associated with coupled solution of these governing equations can be minimized by using efficient and compatible solution techniques together with computationally feasible radiative property models for particle laden combustion gases.

Previous work regarding the search for the most accurate and computationally efficient solution method in the freeboard of fluidized bed combustors revealed that Method of Lines (MOL) solution of Discrete Ordinates Method (DOM) meets all the requirements [20-22]. Assessment of accuracy of this solution method was previously validated against exact solutions, Monte Carlo (MC) and zone method solutions, as well as measurements on a wide range of one-dimensional and multidimensional problems in rectangular and cylindrical coordinates including absorbing, emitting, strongly anisotropically scattering and grey media bounded by grey, diffuse walls [23-27].

With respect to radiative property of particle laden combustion gases, they contribute to radiative heat exchange by emitting, absorbing and scattering radiation in the entire spectrum. Radiative properties of both participating gases and particles are needed to be accounted for accurate modeling of radiation.

Regarding to radiative property modeling of gases, they absorb and emit radiation in specific spectral bands. The properties of gases are best represented by considering their spectral dependency; however, it requires extensive computational

effort. Therefore, grey approximation is often preferred. In an attempt to investigate the sensitivity of radiative heat transfer predictions to grey approximation for gas radiative property estimation, several studies have recently been carried out on radiation models based on Zone Method, DOM and MOL solution of DOM coupled with Grey Gas model, Spectral Line-Based Weighted Sum of Grey Gas (SLW) model and Weighted Sum of Grey Gases (WSGG) model. Predictive accuracy and CPU efficiency of grey approximation were investigated by applying it to the prediction of radiative heat flux and source term on pulverized fuel-fired furnaces and circulating fluidized bed combustors (CFBC) containing grey/non-grey, absorbing, emitting gas with grey, absorbing, emitting and scattering particles and comparing grey predictions with those of non-grey [28-30]. Comparisons reveal that grey approximation for gases provides accurate and computationally efficient solutions in the presence of particles as the particle radiation dominates total radiation [31-34].

With regard to radiative property modeling of particles, when a ray is incident on a large particle, it may be absorbed, diffracted, refracted and reflected. The direction of a ray may be changed due to diffraction, refraction and reflection as illustrated in Figure 1.1. The change in the direction of a ray is known as scattering.

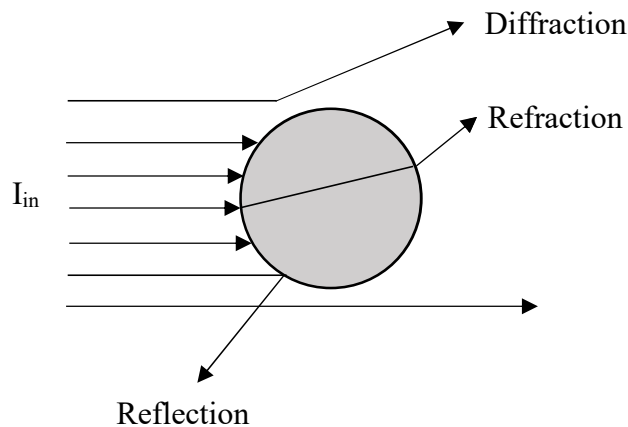


Figure 1.1 Possible ways of scattering from a large particle

Particles not only emit and absorb radiation in the entire spectrum but also scatter radiation depending on their size. Therefore, particle radiation depends on its

absorption coefficient, scattering coefficient and scattering phase function. Mie theory is used to estimate radiative properties of the particles and it is computationally demanding as it provides solutions in the form of infinite series. Mie theory requires wavelength of incident radiation, size of the particle and complex refractive index, $m = n - ik$, as input parameters. The value of complex refractive index is specific to the particle considered and it is wavelength dependent. Thus, Mie theory calculations should be performed for each wavelength of interest within the region of thermal radiation, which leads to computationally demanding calculations. This is why it is common to use grey approach deploying representative complex refractive index values for particles [35].

Butler *et al.* [36] investigated the effect of utilizing grey properties by comparing its predictions with those of spectral solutions and measurements in a laboratory scale pulverized coal-fired reactor. For spectral solutions, radiative properties of the combustion gases were calculated from the Edward's wide band model, those of char and fly ash particles were estimated by using Mie theory whereas radiative property of soot was calculated from extensively used correlation based on soot volume fraction and wavelength [37]. Grey radiation predictions were estimated by using spectrally averaged Planck and Patch mean properties for particles and Leckner's correlations for gases. Grey model predictions using Planck mean properties were found to be in agreement with measurements and those of spectral solution.

Ruan and his colleagues [38] studied the effect of several grey approximation methods on radiative heat transfer in one-dimensional parallel plane system containing nonparticipating gases and absorbing, emitting and anisotropically scattering monodisperse fly ash particles by benchmarking grey predictions of dimensionless emissive power and heat flux against those of non-grey. Rosseland mean is suggested as an appropriate method to calculate extinction coefficient for the system under consideration.

Recently, the predictive accuracy of grey particle assumption in the presence of grey absorbing, emitting gas was investigated in a one-dimensional slab containing

grey/non-grey absorbing, emitting coal and fly ash particles surrounded by cold, black walls [39]. Grey properties of the particles were estimated by utilizing geometric optics approximation (GOA) without considering diffraction and Buckius-Hwang correlations were used to predict non-grey particle properties [40]. For calculation of non-grey particle properties, particle size parameter was assumed to depend on the wavelength; however, spectral dependency of complex refractive index of particles was neglected. With those assumptions, the influence of spectral fly ash properties on source term was found to be insignificant for the system under consideration.

Johansson *et al.* [41] carried out a study in a one-dimensional infinitely long cylinder, which has conditions relevant to pulverized coal combustion, containing non-grey gas with grey/non-grey absorbing, emitting and isotropically scattering fly ash and coal particles to analyze the effect of complex index of refraction on particle scattering and absorption efficiencies by using Mie theory for non-grey particles and Planck mean for grey particles. In the case of non-grey particles, the efficiencies of large particles ($d_{p,ash} = 10 \mu\text{m}$ and $d_{p,coal} = 10 \mu\text{m}$ & $40 \mu\text{m}$) were found not to vary considerably with the change in the complex index of refraction in the wavelength of interest for combustion.

In the work of Ates and co-workers [42], grey solution of RTE was compared with spectrally banded particle solution in dilute zone of 150 kW_t METU CFBC Test Rig containing grey absorbing, emitting gas with absorbing, emitting and anisotropically scattering fly ash particles. Comparisons reveal that heat flux and source term predictions with grey assumption are in good agreement with those of the spectrally banded particle solution in the optically thick media of CFBC.

There also exist recent studies involving solutions with grey/non-grey gas and grey particle radiative properties [23, 43-45] where predictions were found to be in agreement with measurements. However, in these studies, effect of spectral particle properties were not investigated.

Despite the implementation of grey approach, the radiative property estimation through Mie theory may become impractical if particle size distribution (PSD) in the medium is wide since the property calculations should be performed for each size. Furthermore, numerical solution of Mie theory becomes computationally demanding with increasing particle size because number of terms required in the series is as high as particle size parameter. Therefore, in order to obtain CPU efficient solutions, some approximate property estimation models can be used by considering particle size parameter, x , which is the relative size of the particles compared with wavelength of incident radiation [35]. If particle size parameter is much less than one ($x \ll 1$), Rayleigh scattering gives accurate results whereas geometric optics is a very useful approximation if particle size parameter is much larger than unity ($x \gg 1$). Considering large particles encountered in fluidized bed combustors, geometric optics approximation (GOA) can be utilized for the estimation of the radiative properties. In GOA calculations, reflectivity is only input parameter to calculate radiative properties and if it is not known, it can be evaluated from Fresnel's relations using the complex refractive index at spectral range of interest.

Zedtwitz *et al.* carried out a study in a tubular reactor that is directly exposed to concentrated thermal radiation [46]. In the study, non-grey gas with non-grey activated charcoal particles with an average diameter of 1.2 mm were considered. Radiative flux distributions in the medium were calculated by Monte Carlo method coupled with GOA for particles and a correlation proposed by Adzerikho *et al.* [47] for gases. The model predictions were found to be in good agreement with the measurements. The shortcoming of the study is that it does not consider particle size distribution and utilizes average particle diameter.

The accuracy of utilizing GOA was previously assessed in a freeboard of METU 0.3 MW_t Atmospheric Bubbling Fluidized Bed Combustor (ABFBC) containing non-grey absorbing, emitting gas with grey absorbing, emitting and isotropically scattering fly ash particles [44]. Model predictions based on MOL of DOM coupled with spectral line-based weighted sum of grey gases (SLW) for gas and GOA for

particles were found to be in reasonable agreement with measurements. However, the accuracy of model predictions with regard to source term distribution were not reported.

Accuracy of heat flux and source term predictions obtained from utilization of the MOL of DOM coupled with Grey Gas for gas and grey GOA for fly ash particles in optically thick media of CFBC was recently investigated by benchmarking their predictions against those of grey Mie theory [28]. According to their research, utilizing GOA with reflectivity averaged over the hemisphere, which is referred as GOA2 in the study, was found to be an accurate approximation to Mie theory. The shortcoming of the study is that it does not involve measurements for validation of the model predictions.

In another study of Ates and co-workers [42], GOA with Fresnel solution for particle reflectivity, which is referred as GOA3 in the publication, was proposed as an improved alternative to GOA2 for estimation of the radiative properties of grey fly ash particles. The predictive accuracy and computational efficiency of GOA3 were assessed by comparing its predictions with those of spectral particle solution in optically thick medium of CFBC. This comparison indicates that GOA3 provides acceptable accuracy with less CPU time for both heat fluxes and source terms. However, there is no comparison of model predictions with measurements in the study.

In particle radiation, knowing the amount of absorbed and scattered radiation by the particles is not enough to fully describe particle radiation interactions. Scattering phase function, which gives the probability that light incident on a particle in a given direction to be scattered into any other direction, is also required. In general, the scattering phase function is obtained from Mie theory; however, with the oscillatory nature of the phase function, computations become impractical especially for large size parameters. This is why approximated phase functions are usually preferred. This simplification is based on averaging cosine of the scattering angle, known as asymmetry factor, g , which varies between -1, referring to purely backward, and +1, referring to purely forward scattering. The

simplest approximation is the case where $g = +1$ which corresponds to nonscattering particles. The second widely used approximation is isotropic scattering in which equal amounts of radiation are scattered into all directions as shown in Figure 1.2 and asymmetry factor is equal to zero. When asymmetry factor is not equal to 0 or +1, it corresponds to anisotropic scattering. If asymmetry factor varies between 0 and +1, particles scatter in the forward direction whereas if asymmetry factor changes from -1 to 0, particles scatter in the backward direction. Schematic view of the anisotropic scattering is also illustrated in Figure 1.2.

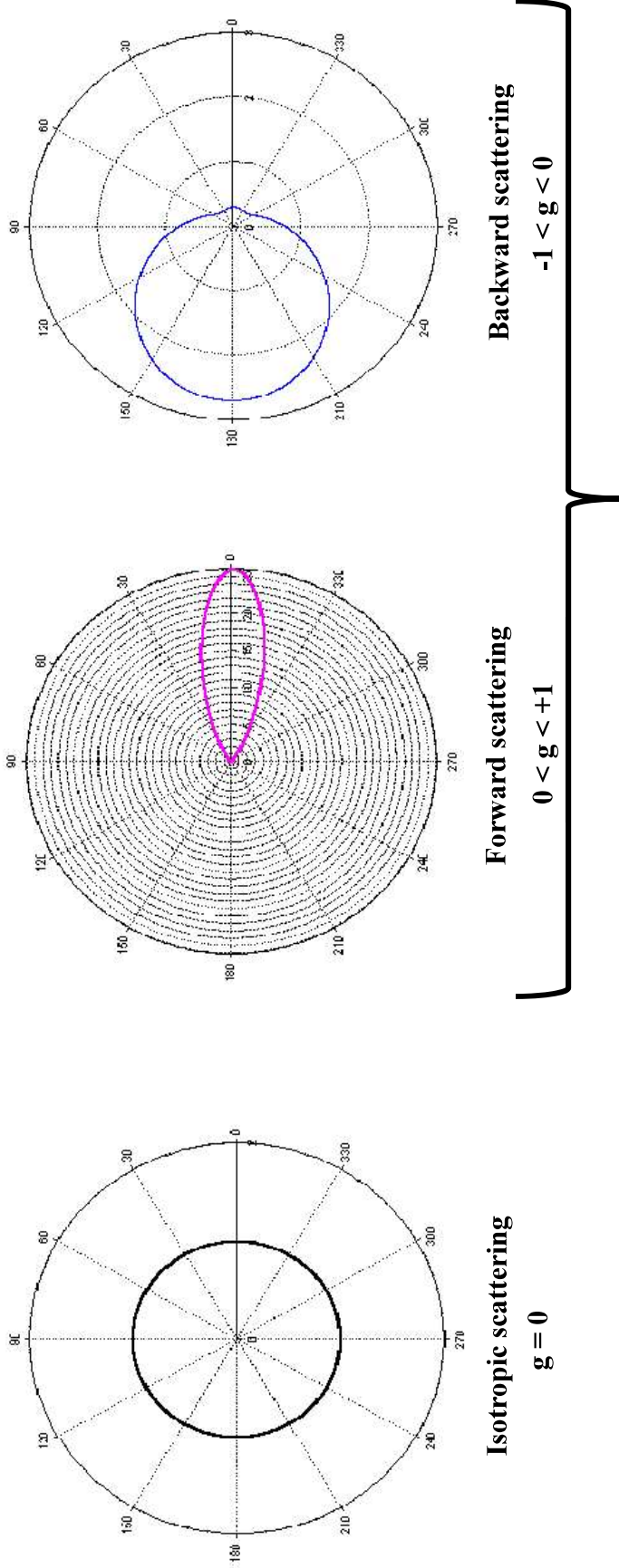


Figure 1.2 Schematic view of isotropic and anisotropic scattering [48]

In coal combustion systems, isotropic scattering and nonscattering assumptions are usually made to simplify the radiative heat transfer problem as well as to reduce the computational effort. However, these assumptions may not represent the highly forward anisotropic scattering behaviour of large coal and ash particles.

One of the earliest studies on the phase function simplification was carried out by Yuen and Wong [49]. They investigated radiative heat transfer in one-dimensional parallel plate test case containing grey, absorbing, emitting and anisotropically scattering particles surrounded by isothermal, grey and diffuse walls. In the model, anisotropic scattering of radiation by the particles were taken into consideration by deploying two term Legendre polynomial expansion. Heat flux predictions of isotropic scattering were compared with those of forward scattering. Comparisons reveal that the importance of deploying anisotropic scattering increases with increasing optical thickness. The shortcoming of this study is that it only provides a parametric study for a simple one-dimensional enclosure and the implemented phase function may not be able to represent the strong forward peak of the particles.

A similar study to that of Yuen *et al.* was also carried out by Mengüç and Viskanta [50], who investigated the effect of phase function simplifications on radiative heat transfer in pulverized coal-fired furnace. A two-dimensional axi-symmetric radiation model based on third order spherical harmonics approximation (P_3) was implemented for the solution of RTE. The medium consists of grey participating gases and particles including pulverized coal, char, fly ash and soot. Delta-Eddington phase function was used to model anisotropic scattering of particles. Heat flux predictions with isotropic and nonscattering assumptions were compared with those of anisotropic scattering. Isotropic and nonscattering assumptions were found to yield inaccurate predictions. The drawback of the study is that it does not involve measurements for validation of the model predictions and does not include the effect of phase function simplifications on source term distributions.

Marakis and his colleagues [51] evaluated total heat flux predictions of isotropic scattering and nonscattering assumptions against those of anisotropic scattering in a pulverized coal-fired furnace considering two different particle loads. Both P_1 and

MC methods were implemented for solution of the RTE. The medium was assumed to be comprised of coal, char and fly ash particles which absorb, emit, and anisotropically scatter radiation. The delta-Eddington phase function was used to represent the highly forward scattering behaviour of the particles and Mie theory was applied to estimate absorption and scattering coefficients of the particles. Discrepancy between the heat flux predictions was found to increase with increasing particle load and the use of anisotropic scattering is recommended for accurate modeling of particle radiation. This study lacks validation of model predictions with measurements and investigation of effect of particle radiation on source term predictions.

Although it is obviously stated in above studies to consider anisotropic scattering of particles, some contrary opinions have been reported. In a study carried out by Liu and Swithenbank [52], the influence of particle scattering on dimensionless heat flux and source term distributions was analyzed by using first order spherical harmonics approximation (P_1) in optically thin medium of three-dimensional furnace. The medium with a given temperature distribution was treated as grey absorbing, emitting, anisotropically scattering fly ash particles. The strong forward scattering behaviour of the particles was represented by delta-Eddington phase function. They concluded that results of forward scattering are closer to those of nonscattering hence if there is a necessity for a phase function simplification, nonscattering assumption yields accurate results for the optically thin medium.

Selçuk and co-workers [21] performed a parametric study to analyze the effects of particle load and anisotropic scattering on the incident wall heat fluxes in the freeboard of METU 0.3 MW_t ABFBC by comparing model predictions with those of the zone method and measurements. The freeboard region was considered as a 3-D rectangular enclosure containing grey absorbing, emitting gas with grey absorbing, emitting and isotropically/anisotropically scattering particles. Leckner's correlations were used to determine gas radiative property and Mie theory was employed to evaluate absorption and scattering coefficients of the fly-ash particles. The case with isotropic scattering assumption was taken as basis and

three different cases were generated by increasing the particle load to three orders of magnitude and/or by incorporating anisotropy into the problem. 1000-fold increase in particle load was found to increase the fluxes both for isotropic and anisotropic scattering treatments. On the other hand, comparison between anisotropic and isotropic scattering reveals that anisotropy has negligible effect on predicted radiative fluxes for both particle loads concerned. Isotropic scattering assumption was found to produce reasonably accurate predictions. This is considered to be due to the smoothness of the linear anisotropic phase function utilized in this study, which may not be able to represent the strong forward scattering of the particles.

Radiative heat exchange in the freeboard of METU 0.3 MW_t ABFBC was also modelled by Kozan *et al.* [20] and Selçuk and co-workers [53]. In these studies, freeboard region was considered as a 3-D rectangular enclosure containing grey absorbing, emitting gas with grey absorbing, emitting and isotropically scattering particles. Leckner's correlations were used for gas radiative property estimation and Mie theory was employed to evaluate absorption and scattering coefficients of the fly-ash particles. In the studies, incident radiative heat fluxes on side walls of the freeboard were predicted and the accuracy of the predictions were assessed by comparing model predictions with measurements. Model predictions were found to be in good agreement with the measurements. This agreement may be attributed to low particle load observed in the freeboard region.

Caliot and co-workers [54] investigated the effect of particle scattering on total heat flux. Monte Carlo method was used to solve radiative transfer. The medium was treated as one-dimensional and consists of participating non-grey gases and grey particles, which have monodispersed distribution with a diameter of 1 μ m. Absorption and scattering coefficients of the particles were calculated by using Planck mean and Henyey-Greenstein phase function was utilized for modeling of anisotropic scattering behaviour. 5 % difference between the predictions of anisotropic scattering and nonscattering was observed for the system under

consideration. Due to one-dimensional treatment of the system and monodispersed approximation of particles, reasonably good agreement was achieved.

There exist recent studies in which use of isotropic assumption has been found to lead to fairly accurate results [32, 44, 45, 55-62] for combusting systems involving low particle loads such as pulverized fuel and bubbling fluidized bed furnaces. In some of these studies, however, isotropic scattering was found to underestimate wall heat fluxes compared to measurements [55-57], which is due to the dominant role of fly ash particles compared to gas and soot radiation [55].

In a recent study, Ates and co-workers [28] investigated the influence of scattering on radiative heat transfer in the dilute zone of CFBC. The dilute zone was treated as two dimensional axisymmetric enclosure containing grey absorbing, emitting gas with grey absorbing, emitting, non/isotropically/anisotropically scattering fly ash particles surrounded by grey diffuse walls. MOL solution of DOM coupled with Grey Gas model for gas and GOA2 for particles were utilized to predict the radiative heat flux and source term distributions. Anisotropic scattering was represented by deploying Henyey-Greenstein phase function. They emphasized that the strong forward scattering behaviour of the fly ash particles must be considered. If the phase function is needed to be simplified for the sake of computational economy, nonscattering assumption is a much better approximation than isotropic scattering for the optically thick media of CFBC.

Despite 40 years of intensive study of scattering phase function simplifications, there are still many uncertainties and disagreements on the subject. Therefore, more detailed studies of particle scattering in combusting systems involving different optical thicknesses are considered to be significantly important for combustion community. Furthermore, a survey of literature revealed that there is a lack of particle radiation modeling studies based on measured input data required for the application of radiation model, which are pressure distributions, gas and wall temperatures, gas compositions, particle size distributions and chemical composition of all solid streams and particle densities, and measured data required

for validation of radiation model, which is wall radiative heat fluxes, obtained from the combusting system operating under steady state conditions.

Therefore, the objective of the present study is to utilize full experimental data available in the literature to investigate the predictive accuracy and computational efficiency of isotropic scattering and nonscattering assumptions by comparing their heat flux and source term predictions with those of anisotropic scattering for different optical thicknesses. An additional objective is to assess the accuracy of grey GOA by benchmarking its predictions against grey Mie solutions for particle property estimation.

In an attempt to achieve these objectives, radiative heat transfer in a fluidized bed combustor with and without recycle is investigated for which complete experimental data are available in literature [63]. The experiments were performed in lignite-fired METU 0.3 MW_t ABFBC Test Rig where radiation is modelled in the freeboard of the combustor by extending a previously developed three-dimensional radiation code based on MOL of DOM in FORTRAN language for the prediction of radiative heat fluxes and source terms along the freeboard of the combustor.

CHAPTER 2

THE METHOD OF LINES SOLUTION OF DISCRETE ORDINATES METHOD

In this chapter, method of lines (MOL) solution of discrete ordinates method (DOM) is described for mathematical modeling of radiative heat transfer in a three-dimensional rectangular enclosure. The physical situation to be considered is that of a uniform, radiatively grey, absorbing, emitting, scattering medium surrounded by grey, diffuse walls. Based on this physical problem, equations representing MOL solution of DOM are derived starting from the radiative transfer equation (RTE) for three-dimensional rectangular coordinate system. This is followed by the numerical solution procedure utilized for the MOL solution of DOM.

2.1. Radiative Transfer Equation

The basis of all methods for the solution of radiation problems is the radiative transfer equation, which is derived by writing a balance equation for radiant energy passing in a specified direction through a small volume element in a uniform, absorbing, emitting, scattering, grey medium and can be written in the form

$$\begin{aligned} \frac{dI}{ds} &= \boldsymbol{\Omega} \cdot \nabla I(\mathbf{r}, \boldsymbol{\Omega}) \\ &= -(\kappa_g + \kappa_p + \sigma_s)I(\mathbf{r}, \boldsymbol{\Omega}) + (\kappa_g + \kappa_p)I_b(\mathbf{r}) + \frac{\sigma_s}{4\pi} \int_{4\pi} I(\mathbf{r}, \boldsymbol{\Omega}') \Phi(\boldsymbol{\Omega}', \boldsymbol{\Omega}) d\boldsymbol{\Omega}' \end{aligned} \quad (2.1)$$

where $I(\mathbf{r}, \boldsymbol{\Omega})$ is the radiation intensity at position \mathbf{r} in the direction $\boldsymbol{\Omega}$ defined as the quantity of radiant energy passing in a specified direction $\boldsymbol{\Omega}$ along a path s per unit solid angle $d\boldsymbol{\Omega}'$, per unit area normal to the direction of travel, per unit time. κ_g , κ_p and σ_s are the gas absorption coefficient, particle absorption coefficient and particle scattering coefficient, respectively. $I_b(\mathbf{r})(\equiv \sigma T^4(\mathbf{r})/\pi)$ is the black-body radiation intensity and $\Phi(\boldsymbol{\Omega}', \boldsymbol{\Omega})$ is the phase function for scattering which describes the fraction of energy scattered from incoming direction $\boldsymbol{\Omega}'$ to the outgoing direction $\boldsymbol{\Omega}$. The expression on the left - hand side represents the change of intensity in the specified direction $\boldsymbol{\Omega}$. The terms on the right - hand side stand for absorption and out-scattering, emission and in-scattering, respectively.

For rectangular coordinate system, the gradient of intensity can be expressed in terms of the derivatives with respect to space coordinates x , y , and z and hence RTE in rectangular coordinates can be written as

$$\begin{aligned} \frac{dI}{ds} &= \mu \frac{\partial I}{\partial x} + \eta \frac{\partial I}{\partial y} + \xi \frac{\partial I}{\partial z} \\ &= -(\kappa_g + \kappa_p + \sigma_s)I(\mathbf{r}, \boldsymbol{\Omega}) + (\kappa_g + \kappa_p)I_b(\mathbf{r}) + \frac{\sigma_s}{4\pi} \int_{4\pi} I(\mathbf{r}, \boldsymbol{\Omega}')\Phi(\boldsymbol{\Omega}', \boldsymbol{\Omega})d\boldsymbol{\Omega}' \end{aligned} \quad (2.2)$$

where the direction cosines can be expressed in terms of the polar angle θ and the azimuthal angle ϕ (Figure 2.1) as $\mu = \cos\theta$, $\eta = \sin\theta \cdot \sin\phi$, and $\xi = \sin\theta \cdot \cos\phi$.

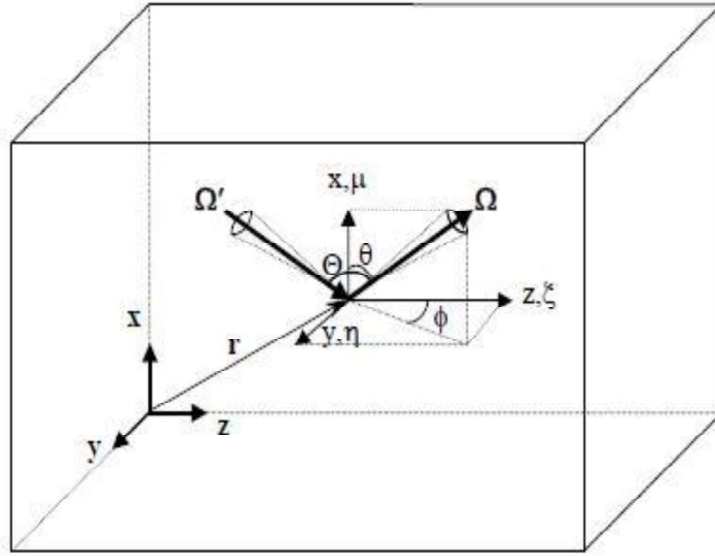


Figure 2.1 Rectangular coordinate system [48]

If the surface bounding the medium is a diffuse and grey wall at specified temperature, then Equation 2.1 is subjected to the boundary condition;

$$I(\mathbf{r}_w, \boldsymbol{\Omega}) = \varepsilon_w \cdot I_{b,w} + \frac{(1 - \varepsilon_w)}{\pi} \int_{\mathbf{n} \cdot \boldsymbol{\Omega}' < 0} |\mathbf{n} \cdot \boldsymbol{\Omega}'| \cdot I(\mathbf{r}_w, \boldsymbol{\Omega}') \cdot d\boldsymbol{\Omega}' \quad \mathbf{n} \cdot \boldsymbol{\Omega} > 0 \quad (2.3)$$

where $I(\mathbf{r}_w, \boldsymbol{\Omega})$ is the radiative intensity leaving the surface at a boundary location, ε_w is the surface emissivity, $I_{b,w} (\equiv \sigma T_w^4 / \pi)$ is the black-body radiation intensity at the surface temperature, \mathbf{n} is the local outward surface normal and $\mathbf{n} \cdot \boldsymbol{\Omega}'$ is the cosine of the angle between incoming direction $\boldsymbol{\Omega}'$ and the surface normal. The first and second terms on the right - hand side of the Equation. 2.3 stand for the contributions to the leaving intensity due to emission from the surface and reflection of the incoming radiation, respectively.

Once the radiation intensities are evaluated by solving Equation 2.2 together with its boundary condition (Equation 2.3), quantities of interest such as radiative flux and energy source term can be readily evaluated. The net radiative heat flux on a surface element is defined as

$$q_{\text{net}} = q^+ + q^- \quad (2.4)$$

where q^+ and q^- are incident and leaving wall heat fluxes, respectively. For a diffuse and grey wall, q^+ and q^- are evaluated from

$$q^+ = \int_{\mathbf{n} \cdot \boldsymbol{\Omega} < 0} |\mathbf{n} \cdot \boldsymbol{\Omega}| \cdot I \cdot d\boldsymbol{\Omega} \quad (2.5)$$

$$q^- = \int_{\mathbf{n} \cdot \boldsymbol{\Omega} > 0} |\mathbf{n} \cdot \boldsymbol{\Omega}| \cdot I \cdot d\boldsymbol{\Omega} \quad (2.6)$$

where $\mathbf{n} \cdot \boldsymbol{\Omega}$ is the cosine of the angle between outgoing direction $\boldsymbol{\Omega}$ and the surface normal. The radiative energy source term, divergence of the total radiative heat flux, for problems where temperature distributions are available is expressed as

$$\nabla \cdot \mathbf{q}_r = \kappa \cdot (4\pi \cdot I_b(\mathbf{r}) - G(\mathbf{r})) \quad (2.7)$$

where \mathbf{q}_r is the radiative heat flux vector, κ is the absorption coefficient of the medium, $I_b(\mathbf{r})(\equiv \sigma T^4(\mathbf{r})/\pi)$ is the black-body radiation intensity and $G(\mathbf{r})$ is the incident radiation defined by

$$G(\mathbf{r}) = \int_{4\pi} I(\mathbf{r}, \boldsymbol{\Omega}) \cdot d\boldsymbol{\Omega} \quad (2.8)$$

2.2. Discrete Ordinates Method

This method is based on representation of continuous angular domain by a discrete set of ordinates with appropriate angular weights, spanning the total solid angle of 4π steradians. The RTE is replaced by a discrete set of equations for a finite number of directions and each integral is replaced by a quadrature summed over the ordinate

directions [64]. The discrete ordinates representation of RTE for a 3-D rectangular enclosure containing a uniform, grey, absorbing, emitting and scattering medium takes the following form:

$$\begin{aligned} \mu_m \frac{\partial I^m}{\partial x} + \eta_m \frac{\partial I^m}{\partial y} + \xi_m \frac{\partial I^m}{\partial z} = & -(\kappa_g + \kappa_p + \sigma_s)I^m + (\kappa_g + \kappa_p)I_b \\ & + \frac{\sigma_s}{4\pi} \sum_{m'=1}^M I^{m'} w_{m'} \Phi(\mathbf{\Omega}_{m'}, \mathbf{\Omega}_m) \end{aligned} \quad (2.9)$$

where $I^m [\equiv I(\mathbf{r}; \mu_m, \eta_m, \xi_m)]$ is the radiation intensity at position $\mathbf{r}(x, y, z)$ in the discrete direction $\mathbf{\Omega}_m$, m denotes the discrete ordinate ($m = 1, 2, \dots, M$), M is the total number of ordinates used in the approximation, μ_m , η_m , and ξ_m are the direction cosines of $\mathbf{\Omega}_m$ with x , y , z axis, respectively and $w_{m'}$ is the angular quadrature weight associated with the incoming direction $\mathbf{\Omega}_{m'}$.

The boundary conditions at the two opposite, diffuse, grey surfaces with normal vectors parallel to x axis can be written as:

at $x = 0$,

$$I^m = \varepsilon_w I_{b,w} + \frac{(1 - \varepsilon_w)}{\pi} \sum_{\mu_{m'} < 0} w_{m'} |\mu_{m'}| I^{m'} \quad \mu_m > 0 \quad (2.10)$$

at $x = L$,

$$I^m = \varepsilon_w I_{b,w} + \frac{(1 - \varepsilon_w)}{\pi} \sum_{\mu_{m'} > 0} w_{m'} |\mu_{m'}| I^{m'} \quad \mu_m < 0 \quad (2.11)$$

where I^m is the intensity of radiation leaving the surface, ε_w is the surface emissivity, $I_{b,w}$ is the total black-body radiation intensity at the temperature of the surface. Similar expressions hold for boundaries in other coordinate directions.

Using the DOM, the RTE is transformed into a set of simultaneous partial differential equations (PDEs) containing only space coordinates as independent variables. Spatial discretization may be accomplished by using a variety of methods

including finite volume, finite element or finite difference techniques. In the classical DOM applications [64-76] spatial differencing is carried out by using standard cell – centred, finite volume technique. In this approach, the discrete ordinates equations are integrated over a typical control volume and interpolation schemes are defined to relate face intensities with cell - centred intensities. An iterative, ordinate sweeping technique described in [76] is applied to solve for the intensities at each ordinate and at each control volume.

Once the intensity distribution is determined by solving Equation 2.9 together with its boundary conditions, the incident radiative flux along a direction i and source term can be obtained from

$$\mathbf{q}_i = \sum_{m'=1}^M w_{m'} \cdot \ell_{m',i} \cdot I^{m'} \quad (2.12)$$

$$\nabla \cdot \mathbf{q}_r = (\kappa_g + \kappa_p) \left(4\pi I_b - \sum_{m,\ell} w_{m,\ell} \cdot I^{m,\ell} \right) \quad (2.13)$$

where $\ell_{m',i}$ is the direction cosine of ordinate $\boldsymbol{\Omega}_{m'}$ with respect to unit vector \mathbf{e}_i , $w_{m'}$ is the angular quadrature weight associated with the incoming direction $\boldsymbol{\Omega}_{m'}$ and $I^{m'}$ is the intensity of radiation incident on the surface.

2.2.1. Parameters Affecting Accuracy of DOM

The accuracy of discrete ordinates method is affected by the accuracy of angular and spatial discretization schemes adopted for the solution. Angular discretization is characterized by the angular quadrature scheme and order of approximation. In an investigation carried out by Selçuk and Kayakol [69] on the assessment of the effect of these parameters on the predictive accuracy of DOM by verification against exact solutions, it was concluded that the order of approximation plays a more significant

role than angular quadrature and spatial differencing schemes in the accuracy of predicted radiative heat fluxes and radiative energy source terms.

The order ($N = 2, 4, 6, 8, 10, 12$) of approximation of DOM, which is also called as S_N method, determines the total number of discrete directions, M . A sketch of the directions used in one octant of a unit sphere for S_2 , S_4 , S_6 , S_8 and S_{10} order of approximations is shown in Figure 2.2. As can be seen from the figure, discrete directions are ordered in levels (constant θ) and number of directions is different at each level. Table 2.1 summarizes the total number of discrete directions used for S_N approximation for one - and multi - dimensional problems.

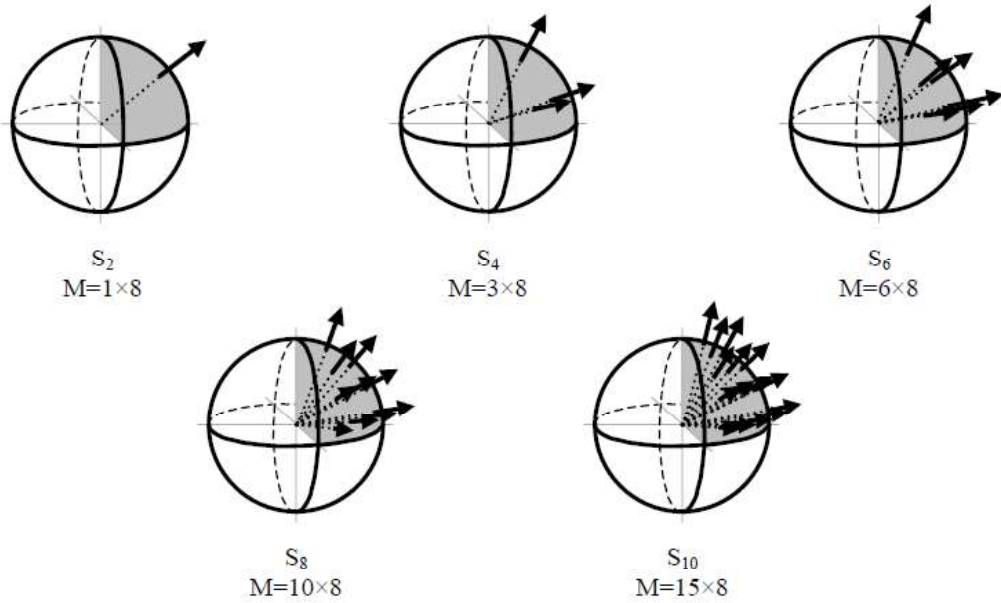


Figure 2.2 Orders of approximation [48]

Table 2.1 Total number of discrete directions used for S_N approximation

S_N approximation	1 – D $M = N$	3 – D $M = 2^D N(N+2) / 8$
S_2	2	8
S_4	4	24
S_6	6	48
S_8	8	80
S_{10}	10	120
S_{12}	12	168

As reported in literature [77-79], once a discrete number of directions is used to approximate a continuous angular variation, ray effect is unavoidable. The increase in the number of discrete directions would alleviate the ray effect at the expense of additional computational time and memory requirement. However, increasing order of angular quadrature scheme may lead to stability problems [67]. Hence, improvement in solution accuracy can only be achieved if finer angular subdivision is accompanied by finer spatial subdivision [80].

The second parameter affecting the accuracy of DOM is the angular quadrature scheme, which defines the specifications of ordinates $\Omega_m (\mu_m, \eta_m, \xi_m)$ and corresponding weights w_m used for the solution of RTE. The choice of quadrature scheme is arbitrary although restrictions on the directions and weights arise from the need to preserve symmetries and invariance properties of the physical system. Completely symmetric angular quadrature schemes, which mean symmetry of the point and surface about the centre of the unit sphere, also about every coordinate axis as well as every plane containing two coordinate axes, are preferred because of their generality and to avoid directionally biasing solutions. Therefore, the description of the points in one octant is sufficient to describe the points in all octants. The quadrature sets are constructed to satisfy key moments of the RTE and its boundary conditions. The quadratures satisfy zeroth, first and second moments

that correspond to incident energy, heat flux and diffusion condition, respectively in addition to higher moments. In practical heat transfer applications, scattering of radiant energy is anisotropic and angular quadrature schemes should satisfy as many moments to accurately integrate the phase function.

The most frequently used angular quadrature scheme is S_N , originally developed by Carlson and Lathrop [81] and extended to higher order of approximations by Fiveland [82] and El Wakil and Sacadura [83]. Therefore, in this study DOM calculations will be based on S_N angular quadrature scheme. The quadrature ordinates and weights for S_N approximations are listed in Appendix A.

The third parameter affecting the accuracy of DOM is the spatial differencing scheme. The conventional spatial discretization technique incorporated with DOM is the finite volume method which makes use of face interpolation schemes that provide assumptions on the form of radiative intensity variation in a control volume. They are based on expressing the downstream (exit) cell boundary intensity as a function of a number of adjacent cell-centre or face intensities depending upon the order of the scheme. The spatial differencing schemes can be basically classified as step (upwind), diamond differencing (DDS, central), variable weight differencing, exponential and high-order, high resolution bounded schemes. Detailed treatment on the first four scheme is presented in [84]. Application of high order, high resolution, bounded schemes such as MINMOD, MUSCL, CLAM and SMART and their applications to DOM can be found in [85] and [86].

As reported in literature [77-79], spatial discretization of the computational domain results in false scattering, which is also referred to as numerical smearing in the radiative transfer community [78]. The use of higher – order spatial schemes or finer spatial grid resolution reduces the numerical smearing error [77, 78]. For prediction of the numerical smearing error, Hunter and Guo [77] has recently developed a proportionality relation expressed by

$$|E_x^{m,n}| \propto \left| \left(\frac{\Delta\tau_x}{\mu^m} \right)^n \left(1 - \frac{\Delta\tau_x}{\mu^m} \right) \right| \quad (2.14a)$$

$$|E_y^{m,n}| \propto \left| \left(\frac{\Delta\tau_y}{\eta^m} \right)^n \left(1 - \frac{\Delta\tau_y}{\eta^m} \right) \right| \quad (2.14b)$$

$$|E_z^{m,n}| \propto \left| \left(\frac{\Delta\tau_z}{\xi^m} \right)^n \left(1 - \frac{\Delta\tau_z}{\xi^m} \right) \right| \quad (2.14c)$$

$$\Delta\tau_j = \beta \times \Delta j \quad \text{for } j = x, y, z \quad (2.15)$$

where E is error due to numerical smearing, m denotes the discrete ordinates, n represents order of accuracy of the chosen spatial differencing scheme, μ , η , ξ are direction cosines in x, y, z directions, respectively and β is the extinction coefficient of the medium. Total numerical smearing error, E_{NS} , can be expressed using the root-sum-squares (RSS) method for 3-D problems as follows [77]:

$$E_{NS} = \sqrt{\sum_{m=1}^M [(E_x^{m,n})^2 + (E_y^{m,n})^2 + (E_z^{m,n})^2]} \quad (2.16)$$

where M is the total number of ordinates used in the approximation.

2.3. Method of Lines Solution of Discrete Ordinate Method

The solution of discrete ordinates equations with MOL is carried out by adoption of the *false – transients* approach which involves incorporation of a pseudo – time derivative of intensity into the discrete ordinates equation [87]. Application of the false – transients approach to Equation 2.9 yields

$$\begin{aligned} k_t \frac{\partial I^m}{\partial t} = & -\mu_m \frac{\partial I^m}{\partial x} - \eta_m \frac{\partial I^m}{\partial y} - \xi_m \frac{\partial I^m}{\partial z} - (\kappa_g + \kappa_p + \sigma_s) \cdot I^m + (\kappa_g + \kappa_p) \cdot I_b \\ & + \frac{\sigma_s}{4\pi} \cdot \sum_{m'=1}^M I^{m'} \cdot w_{m'} \cdot \Phi(\boldsymbol{\Omega}_{m'}, \boldsymbol{\Omega}_m) \end{aligned} \quad (2.17)$$

where t is the pseudo – time variable and k_t is a time constant with dimension $[(m/s)^{-1}]$ which is introduced to maintain dimensional consistence in the equation and it is taken as unity.

The system of PDEs with initial and boundary – value independent variables is then transformed into an ODE initial - value problem by using the method of lines approach [88]. The transformation is carried out by representation of the spatial derivatives with algebraic finite – difference approximations. Starting from an initial condition for radiation intensities in all discrete directions, the resulting ODE system is integrated until steady state by using a powerful ODE solver. The ODE solver takes the burden of time discretization and chooses the time steps in a way that maintains the accuracy and stability of the evolving solution. Any initial condition can be chosen to start the integration, as its effect on the steady-state solution decays to insignificance. To stop the integration at steady state, a convergence criteria was introduced. If the intensities at all nodes and ordinates satisfy the condition given below, the solution at current time is considered to be the steady state solution and the integration is terminated. The condition for steady state is

$$\frac{|I_t - I_{t-1}|}{I_{t-1}} < \epsilon \quad (2.18)$$

where ϵ is the error tolerance, the subscript t denotes the solution at current print time and subscript $t-1$ indicates solutions at previous print time. As a result, evolution of radiative intensity with time at each node and ordinate is obtained. The steady-state intensity values yield the solution to Equation 2.9 because the artificial time derivative vanishes at steady state.

Once the steady state intensities at all grid points are available, the incident radiative heat flux on enclosure boundaries and radiative energy source terms at interior grid points can be evaluated by using Equations 2.12 and 2.13, respectively.

2.3.1. Parameters Affecting Accuracy of MOL Solution of DOM

The accuracy and efficiency of MOL solution of DOM is determined by the following parameters:


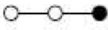
- accuracy of the angular approximation (DOM)

- accuracy of the spatial discretization technique
- the ODE solver utilized for integration in the ‘pseudo-time’ variable.

The accuracy of the angular approximation depends on the angular quadrature scheme and the order of approximation selected for the implementation of the DOM. Therefore, dependence of the accuracy of MOL solution of DOM on the angular approximation is the same as that of DOM (see Section 2.2.1).

The spatial discretization technique used in MOL solution of DOM is the finite-difference method (FDM) unlike the classical DOM which employs finite-volume technique for this purpose. In the FDM, the spatial derivatives are replaced by linear, algebraic approximations derived generally from a Taylor series expansion. The spatial discretization schemes used in this study are the two- and three-point upwind schemes (DSS012 and DSS014) [88, 89]. The reason behind the choice of upwind schemes is as follows. After the implementation of false-transients approach, the discrete ordinates equations take the form of first-order hyperbolic PDEs for which upwind schemes are strongly recommended [88,89] due to consideration of the direction of propagation of the dependent variables which eliminate the numerical oscillations caused by central differencing. The formulation and order of accuracy of the selected schemes are presented in Table 2.2.

Table 2.2 Spatial differencing schemes [88,89]

Name of the scheme	Stencil	Formulation	Order of accuracy
2-point upwind (DSS012)		$(I_i - I_{i-1})/\Delta\lambda$	$O(\Delta\lambda)$
3-point upwind (DSS014)		$(3I_i - 4I_{i-1} + I_{i-2})/2\Delta\lambda$	$O(\Delta\lambda^2)$

The third factor affecting accuracy of MOL solution of DOM is the ODE integrator. In this study, ODE solver utilized is ROWMAP which is based on the ROW-methods of order 4 and uses Krylov techniques for the solution of linear systems. By a special multiple Arnoldi process the order of the basic method is preserved

with small Krylov dimensions. Step size control is done by embedding with a method of order 6. Detailed description of ROWMAP can be found elsewhere [90].

2.4. Structure and Operation of Computer Code

Figures 2.3 and 2.4 show the flow diagram of the computer code Method of Lines Solution of Discrete Ordinates Method for absorbing, emitting and scattering medium in rectangular coordinates (MOLSDOM - AESM). The general steps of the computer code are as follows:

1. Define the subdivision of the enclosure, number of wide bands, order of approximation and number of equations in the system of ODEs.
2. Declare 6-D arrays to store intensities, position derivatives, and time derivatives at each ordinate of each grid point. The 6-D arrays are of dimensions $[NX \times NY \times NZ \times ND \times NM \times NB]$ where NX , NY and NZ are the number of nodes along x , y and z -axes respectively, ND is the number of octants considered in the calculation ($ND=8$ for a 3-D problem), NM is the number of ordinates specified by the order of angular quadrature and NB is the number of wide bands for particles ($NB=1$ for grey particles).
3. Specify parameters for the ODE integrator which are the initial time, final time, print interval and the error tolerance.
4. Specify initial condition for the intensities.
5. Read in input data specifying the physics of the problem which are, the dimensions of the enclosure, emissivities of the walls, gas composition of the medium, temperatures and temperature profiles of the medium and the walls.
6. Specify direction cosines and corresponding weights.
7. Initialize the intensities at all ordinates at all grid points.
8. Print interpolated temperature profiles of the medium and side wall.
9. Read in input data related to radiative properties of the medium which are gas and particle absorption coefficients, particle scattering coefficient and coefficients of the scattering phase function.
10. Calculate the scattering phase function for each incoming and outgoing ordinates.

11. Set boundary conditions for the intensities leaving the boundary surfaces by using Equations 2.10 and 2.11.

Calculation of the Approximations for the Spatial Derivatives:

12. Specify the spatial discretization scheme (DSS012 or DSS014).
13. Specify an octant and ordinate.
14. Specify a discrete location on the y, z plane.
15. Store the values of the intensities (at this direction and location) along x – axis in a 1-D array.
16. Call for spatial discretization subroutine which accepts the 1-D array of intensities as an input and computes the derivative with respect to x – axis as an output over the grid of NX points.
17. Transfer the 1-D array of spatial derivatives into 6-D array of x – derivatives.
18. Repeat steps 13-17 for all discrete locations on y-z plane, all ordinates and all octants.
19. Repeat steps 13-18 for derivative terms with respect to y and z-axes, forming 1-D arrays along y and z – axes.

Calculation of the Time Derivatives:

20. Set the signs of the direction cosines for each octant.
21. Calculate the time derivative of intensity at each node for each ordinate of each octant using Equation 2.17 to form a 6-D array of time derivatives.
22. Set boundary conditions for the intensities leaving the boundary surfaces by using Equation 2.10 and Equation 2.11.
23. Transform the 6-D arrays of intensities and time derivatives into 1-D arrays to be sent to the ODE solver.

Integration of the system of ODEs:

24. Set the initial conditions required for the ODE integrator.
25. Set parameters for the ODE integrator.
26. Call the ODE solver subroutine to integrate the system of ODEs by using a time adaptive method. The ODE propagates in time by solving for the intensities at

a time step j , calculating the time derivatives by performing steps 11 to 23 and integrating again to solve for intensities at the new time step $j+1$.

27. Return to the main program at prespecified time intervals.
28. Check if ODE integration has proceeded satisfactorily.
29. Transfer the solution at current print point from the 1-D array to a 6-D array.
30. Set the boundary conditions at current time step.
31. Check for convergence by comparing the solutions at current time step with those at previous three time steps. If current solution is within the specified range of the previous solution, convergence is established go to step 35.
32. If convergence is not established, save the solution for convergence check.
33. Check end of the run time if final time is not reached go back to step 13.
34. If convergence is established or final time is reached, calculate the parameters of interest such as incident radiative heat flux and radiative energy source term.
35. Print output.
36. Stop.

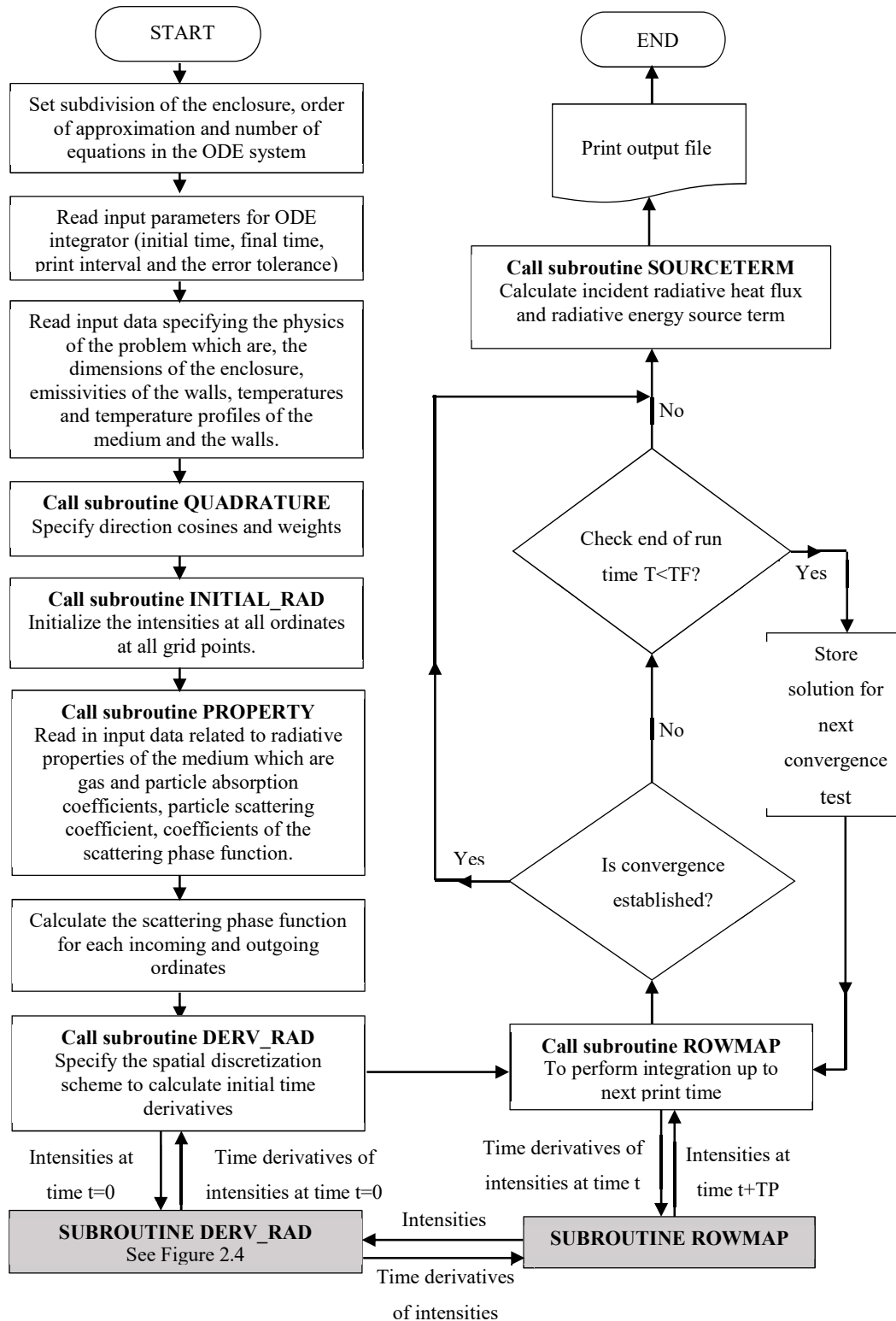


Figure 2.3 Flowchart for MOLSDOM - AESM

CHAPTER 3

RADIATIVE PROPERTY ESTIMATION TECHNIQUES

In order to determine radiative heat transfer accurately, both accurate solution of the RTE and reliable evaluation of radiative properties of the medium and surrounding surfaces are required. In the preceding chapter, MOL solution of DOM as an accurate and CPU efficient technique for the solution of RTE has been explained. In this chapter, Grey Gas (GG) model for gas and Mie theory and geometric optics approximation (GOA) for grey particles are described to estimate radiative property of particle laden combustion gases.

3.1. Property Estimation of Gases

The most fundamental radiative property of participating gases is the absorption coefficient. A number of models with varying degrees of complexity and accuracy has been developed so far for the estimation of the radiative properties. These models can be classified into two main groups, namely grey and non-grey gas radiative property models. Non-grey models take into account wavelength dependency of radiative property whereas grey gas model assumes that radiative property is independent of wavelength. From the view point of accuracy and CPU efficiency, Grey Gas model has previously been found to be sufficient in the presence of particles according to study carried out by Ates *et al.* [28]. Therefore, the details of the grey gas model will be described in the following sub-section.

3.1.1. Grey Gas Model

In Grey Gas model, a single value of the absorption coefficient is used to represent whole spectrum as it assumes that radiative property is independent of wavelength. In this model, radiative properties of participating combustion gases are estimated by Leckner's correlations [35], which require the partial pressures of carbon dioxide and water vapor, the gas temperature and mean beam length, L_m . Calculation of the gas emissivity, ϵ_g , through Leckner's correlations leads to gas absorption coefficient, κ_g , expressed by

$$\kappa_g = -\frac{1}{L_m} \times \ln(1 - \epsilon_g) \quad (3.1)$$

3.2. Property Estimation of Grey Particles

Particles continuously emit and absorb radiation in the entire spectrum and also scatter radiation depending on their size. Therefore, particle radiation depends on its absorption coefficient, scattering coefficient and scattering phase function. As spectral solution of particle radiation is complex and computationally demanding, it is common to use grey approach. Mie theory and geometric optics approximation (GOA) will be described to estimate the radiative properties of grey particles in the following sub-sections.

3.2.1. Mie Theory

Mie theory is used to determine the radiative properties of the particles. For accurate prediction of radiative properties of the particles it is essential to solve Maxwell's equations. The amount of scattering and absorption by a particle is expressed in terms of the scattering cross-section, C_{scat} , and absorption cross-section, C_{abs} . The total amount of absorption and scattering, which is called as extinction, is expressed in terms of the extinction cross-section,

$$C_{ext} = C_{abs} + C_{scat} \quad (3.2)$$

the extinction and scattering cross sections are evaluated by using Mie theory

$$C_{\text{scat}} = \frac{2\pi a^2}{x^2} \sum_{n=1}^{\infty} (2n+1)(|a_n|^2 + |b_n|^2) \quad (3.3)$$

$$C_{\text{ext}} = \frac{2\pi a^2}{x^2} \sum_{n=1}^{\infty} (2n+1)\text{Re}(a_n + b_n) \quad (3.4)$$

where a is the radius of the spherical particle. The Mie scattering coefficient a_n and b_n are complex functions of x and $y = mx$,

$$a_n = \frac{\psi_n'(y)\psi_n(x) - m\psi_n(y)\psi_n'(x)}{\psi_n'(y)\xi_n(x) - m\psi_n(y)\xi_n'(x)} \quad (3.5)$$

$$b_n = \frac{m\psi_n'(y)\psi_n(x) - \psi_n(y)\psi_n'(x)}{m\psi_n'(y)\xi_n(x) - \psi_n(y)\xi_n'(x)} \quad (3.6)$$

The functions ψ_n and ξ_n are known as Ricatti-Bessel functions and related to Bessel and Hankel functions by [35]

$$\psi_n(z) = \left(\frac{\pi z}{2}\right)^{\frac{1}{2}} J_{n+\frac{1}{2}}(z), \quad \xi_n(z) = \left(\frac{\pi z}{2}\right)^{\frac{1}{2}} H_{n+\frac{1}{2}}(z) \quad (3.7)$$

After determining Mie scattering coefficients a_n and b_n , the phase function can be calculated from

$$\Phi(\Theta) = 2 \frac{i_1 + i_2}{x^2 Q_{\text{scat}}} \quad (3.8)$$

where i_1 and i_2 are nondimensional polarized intensities calculated from

$$i_1(x, m, \Theta) = |S_1|^2 \quad \text{and} \quad i_2(x, m, \Theta) = |S_2|^2 \quad (3.9)$$

$S_1(\Theta)$ and $S_2(\Theta)$ are the complex amplitude functions and expressed by

$$S_1(\Theta) = \sum_{n=1}^{\infty} \frac{(2n+1)}{n(n+1)} [a_n \pi_n(\cos \Theta) + b_n \tau_n(\cos \Theta)] \quad (3.10)$$

$$S_2(\theta) = \sum_{n=1}^{\infty} \frac{(2n+1)}{n(n+1)} [b_n \pi_n(\cos \theta) + a_n \tau_n(\cos \theta)] \quad (3.11)$$

where the direction dependent functions π_n and τ_n are related to Legendre polynomials P_n by

$$\pi_n(\cos \theta) = \frac{dP_n(\cos \theta)}{d \cos \theta} \quad (3.12)$$

$$\tau_n(\cos \theta) = \cos \theta \pi_n(\cos \theta) - \sin^2 \theta \frac{d\pi_n(\cos \theta)}{d \cos \theta} \quad (3.13)$$

where Legendre polynomial P_n is expressed by

$$\begin{aligned} P_0(\cos \theta) &= 1 \\ P_1(\cos \theta) &= \cos \theta \\ P_2(\cos \theta) &= \frac{1}{2} (3(\cos \theta)^2 - 1) \\ P_3(\cos \theta) &= \frac{1}{2} (5(\cos \theta)^3 - 3 \cos \theta) \\ &\vdots \\ P_n(i) &= \sum_{k=0}^n \binom{n}{k} \binom{-n-1}{k} \left(\frac{1-i}{2}\right)^2 \end{aligned} \quad (3.14)$$

However, calculation of phase function from Equation 3.8 is tedious due to nature of Equation 3.9 and calculations must be carried out for every scattering angle θ [35]. In order to facilitate the calculations, if the particle is axisymmetric Mie scattering phase function can be expressed by Legendre polynomials

$$\Phi(\theta) = 1 + \sum_{n=1}^{\infty} A_n P_n(\cos \theta) \quad (3.15)$$

where θ is the scattering angle between radiation directions $\Omega_{m',\ell'}$ and $\Omega_{m,\ell}$, A_n is determined by curve fitting to the Mie results as shown by [91] and P_n is the Legendre polynomial of degree n . Although it is possible to calculate numerically exact Mie phase function, it is common to approximate the scattering phase function as a truncated Legendre series:

$$\Phi_L(\theta) = 1 + \sum_{n=1}^N A_n P_n(\cos \theta) \quad (3.16)$$

where N is the chosen order of approximation and is a function of the size parameter ($x = \pi d / \lambda$) and the complex refractive index ($m = n - ik$) [91].

Radiative properties of particles are generally calculated by using the BHMIE code based on Mie theory [92]. In the code, the logarithmic derivative, D_n , is used to evaluate the Mie scattering coefficient a_n and b_n .

$$D_n(z) = \frac{d}{dz} \ln \psi_n(z) \quad (3.17)$$

Then Mie scattering coefficients, Equations 3.5 and 3.6, can be rewritten as

$$a_n = \frac{[D_n(y)/m + n/x] \psi_n(x) - \psi_{n-1}(x)}{[D_n(y)/m + n/x] \xi_n(x) - \xi_{n-1}(x)} \quad (3.18)$$

$$b_n = \frac{[mD_n(y) + n/x] \psi_n(x) - \psi_{n-1}(x)}{[mD_n(y) + n/x] \xi_n(x) - \xi_{n-1}(x)} \quad (3.19)$$

where the recurrence relations are used as

$$\begin{aligned} \psi_n'(x) &= \psi_{n-1}(x) - \frac{n\psi_n(x)}{x}, \\ \xi_n'(z) &= \xi_{n-1}(x) - \frac{n\xi_n(x)}{x} \end{aligned} \quad (3.20)$$

to eliminate ψ_n' and ξ_n' . The logarithmic derivative satisfies the recurrence relation

$$D_{n-1} = \frac{n}{z} - \frac{1}{D_n + \frac{n}{z}} \quad (3.21)$$

$D_n(y)$ in equations 3.18 and 3.19 is computed by the downward recurrence relation between Equation 3.21 beginning with D_{NMX} .

In BHMIE, series are terminated after NSTOP terms, where NSTOP is the integer closest to $x + 4x^{1/3} + 2$ and NMX is taken to be $\text{Max}(\text{NSTOP}, |y|) + 15$ and D_{NMX} starts with $0.0 + i0.0$.

Both ψ_n and $\xi_n (= \xi\psi_n - i\chi_n)$ satisfy

$$\psi_{n+1}(x) = \frac{2n+1}{x} \psi_n(x) - \psi_{n-1}(x) \quad (3.22)$$

and are computed by this upward recurrence relation beginning with

$$\psi_{-1}(x) = \cos x, \quad \psi_0(x) = \sin x, \quad \chi_{-1}(x) = -\sin x, \quad \chi_0(x) = \cos x \quad (3.23)$$

Detailed description of the BHMIE code can be found elsewhere [92]. Moreover, calculation of asymmetry factor, g , is added into BHMIE code to evaluate scattering phase function approximated by the Henyey-Greenstein phase function as [35]

$$g = \frac{4\pi a^2}{x^2 C_{\text{scat}}} \sum_{n=1}^{\infty} \left[\frac{n(n+2)}{n+1} \text{Re}\{a_n a_{n+1}^* + b_n b_{n+1}^*\} + \frac{2n+1}{n(n+1)} \text{Re}\{a_n b^*\} \right] \quad (3.24)$$

BHMIE code based on Mie theory is used to provide particle extinction and scattering efficiencies and asymmetry factor for each particle size. After calculating the efficiencies for each size interval i between $(-d_{p,n+1} + d_{p,n})$ radiative coefficients of the particles can be computed by

$$\kappa_{p,i} = \int_{d_{p,n}}^{d_{p,n+1}} Q_{\text{abs}} \cdot \pi \frac{(d_p)^2}{4} \cdot n(d_p) \cdot dd_p \quad (3.25)$$

$$\sigma_{s,i} = \int_{d_{p,n}}^{d_{p,n+1}} Q_{\text{scat}} \cdot \pi \frac{(d_p)^2}{4} \cdot n(d_p) \cdot dd_p \quad (3.26)$$

where d_p and $n(d_p)$ are particle diameter and particle size distribution function, respectively. After integrating above equations for each size interval, absorption and scattering coefficients can be expressed as

$$K_p = \sum_{i=1}^T (K_p)_i \quad (3.27)$$

$$\sigma_s = \sum_{i=1}^T (\sigma_s)_i \quad (3.28)$$

where T represents the total number of particle sizes under consideration.

Although the total absorption and scattering coefficients of the medium are calculated by summation over radiative properties of all sizes, estimation of the asymmetry factor of the medium is based on surface area weighted average of particles as shown below

$$g = \sum \frac{\pi \frac{(d_{p,i})^2}{4}}{A_c} \cdot g_i \cdot n(d_{p,i}) \quad (3.29)$$

where A_c represents total cross sectional area of the particles.

3.2.2. Geometric Optics Approximation (GOA)

If a particle is relatively large compared to wavelength of incident radiation ($x \gg 1$), Mie theory calculations for property estimation do not provide CPU efficient predictions because the series expansions used to evaluate the expressions in the full Mie theory converge very slowly [93]. Therefore, some approximations are used in order to provide CPU efficient property estimation by considering particle size parameter which is defined as

$$x = \frac{\pi d_p}{\lambda} \quad (3.30)$$

where d_p and λ represents diameter of spherical particle and wavelength of incident radiation, respectively.

For GOA to be applicable, size parameter of the particles are expected to be larger than 25 [35]. For particles which are large, opaque and reflect radiation diffusely, the extinction efficiency can be expressed by

$$Q_{\text{ext}} = 2 \quad (3.31)$$

In the above extinction efficiency expression the half is due to diffraction and the other half is due to absorption and reflection. Refraction is not taken into consideration since the particles are large and opaque; that is, any ray refracted into the particle will be totally absorbed [35]. Absorption and scattering efficiencies of the particle are calculated by using the reflectivity of the particle;

$$Q_{\text{abs}} = \alpha = 1 - \rho \quad (3.32)$$

$$Q_{\text{scat}} = Q_{\text{ext}} - Q_{\text{abs}} \quad (3.33)$$

where α and ρ represents absorptivity and reflectivity, respectively.

Fresnel's relations are used to estimate reflectivity of the particles using the complex refractive index, $m=n-ik$, within the spectral range of interest. For directional-hemispherical reflectivity in normal direction, the simplest approximation to Fresnel's relations is obtained if the absorption index is much smaller than the real part ($k^2 \ll (n-1)^2$). [35]:

$$\rho_{\perp} = \left(\frac{n-1}{n+1} \right)^2 \quad (3.34)$$

where ρ_{\perp} and n are reflectivity in normal direction and the refractive index of particle, respectively. It should be noted that Equation 3.34 is valid only for normal direction. However, it is a good approximation as emissivity (so does reflectivity for an opaque medium) is almost constant between 0-60°, which is acceptable for

furnace applications as the incident radiation [35] is expected to fall within this range. On the other hand, this assumption may lead to a considerable error for high values of the scattering albedo of the medium. For higher accuracy, reflectivity averaged over the hemisphere can be used [94]:

$$\bar{\rho} = \frac{1}{2} + \frac{(3n+1)(n-1)}{6(n+1)^2} + \frac{n^2(n^2-1)^2}{(n^2+1)^3} \ln\left(\frac{n-1}{n+1}\right) - \frac{2n^3(n^2+2n-1)}{(n^2+1)(n^4-1)} + \frac{8n^4(n^4+1)}{(n^2+1)(n^4-1)^2} \ln n \quad (3.35)$$

Nevertheless, utilizing the reflectivity averaged over the hemisphere may result in incorrect predictions since it neglects angular dependency of reflectivity in absorption index [42]. Another approach for calculating reflectivity, which is referred as GOA3 in previous publication [42], is to integrate directional-hemispherical reflectivities obtained with the Fresnel's relations over all directions. Integration is performed numerically with 1° intervals between 0-180° [42].

After calculating the reflectivity, absorption and scattering efficiencies can be calculated from equations 3.32 and 3.33. By using these efficiencies, absorption and scattering coefficients of particles for a discrete mass size distribution, can be expressed by

$$\kappa_p = \int_{d_{p,\min}}^{d_{p,\max}} Q_{\text{abs}} \cdot \pi \frac{(d_p)^2}{4} \cdot n(d_p) \cdot dd_p \quad (3.36)$$

$$\sigma_s = \int_{d_{p,\min}}^{d_{p,\max}} Q_{\text{scat}} \cdot \pi \frac{(d_p)^2}{4} \cdot n(d_p) \cdot dd_p \quad (3.37)$$

where d_p and $n(d_p)$ are particle diameter and particle size function, respectively. Unlike Mie theory, scattering and absorption efficiencies of the particle do not depend on particle size in GOA. Hence, if particle size function is substituted into above equations, the radiative coefficients can be calculated by

$$\kappa_{p,i} = \frac{1.5Q_{abs}\Delta B_i}{\rho_p(\Delta d_p)_i} \int_{d_{p,n}}^{d_{p,n+1}} \frac{dd_p}{d_p} \quad (3.38)$$

$$\sigma_{s,i} = \frac{1.5Q_{scat}\Delta B_i}{\rho_p(\Delta d_p)_i} \int_{d_{p,n}}^{d_{p,n+1}} \frac{dd_p}{d_p} \quad (3.39)$$

where ρ_p is particle density and ΔB_i is the mass retained in interval i between ($-d_{p,n+1} + d_{p,n}$). After the integration with respect to particle diameter, absorption and scattering coefficients of the particles expressed as summation over all intervals are found as;

$$\frac{\kappa_p}{\alpha} = \sum_{i=1}^T \left(\frac{\kappa_p}{\alpha} \right)_i \quad (3.40)$$

$$\frac{\sigma_s}{\rho} = \sum_{i=1}^T \left(\frac{\sigma_s}{\rho} \right)_i \quad (3.41)$$

where T represents the total number of particle sizes under consideration.

Sauter mean diameter of particle size distribution is used in Mie theory in order to calculate the asymmetry factor of the medium as it eliminates the necessity for evaluation of asymmetry factor by Mie theory for each particle size in the distribution.

3.2.3. Scattering Phase Function and Its Normalization

In addition to estimation of absorption and scattering coefficients of the particles accurately, it is important to account for scattering properly while modeling the radiative heat transfer in particle laden combustion gases. Scattering is represented by scattering phase function, which is the probability distribution of radiation propagating in a given direction scattered into another direction due to the presence of particles along its path. Scattering of radiation can be determined from

the Mie theory provided that the complex refractive index and the size parameter of the particles are known. If the particle is axisymmetric, the phase function is represented by Legendre polynomials of the n^{th} order (Equation 3.16). In the numerical solution, the phase function is approximated by finite series and number of terms required is around the size parameter of the particle. With the oscillatory nature of the phase function, computations become impractical especially for large size parameters. Therefore, approximated phase functions are usually preferred by averaging cosine of the scattering angle, known as asymmetry factor:

$$g = \overline{\cos(\Theta)} = \frac{1}{4\pi} \int_{4\pi} \Phi(\Theta) \cos(\Theta) d\Omega \quad (3.42)$$

which changes from -1 to +1 representing purely backward scattering and purely forward scattering, respectively. The simplest approximations are the cases where g is either 0 or +1. In the former case, equal amounts of radiation are scattered into all directions (i.e. $\Phi = 1$) giving isotropic scattering while in the latter medium becomes nonscattering. In coal combustion systems it is observed that large coal and ash particles predominantly have strong forward scattering peaks leading to g values in the range of 0.5 - 1. As exact numerical solution of Mie scattering phase function is computationally demanding, some approximations are usually preferred in the combustion community.

Furthermore, the conservation of both scattered energy and shape of the asymmetry factor is as important as the implementation of proper phase function approximation to eliminate changes in the scattering properties of the particles. It is widely known that DOM discretization of the continuous angular variation of radiative intensity results in inaccurate radiative heat transfer predictions or does not converge for cases where scattering is highly anisotropic due to violation of scattered energy conservation and distortion in shape of the asymmetry factor. In order to alleviate these problems, phase function normalization techniques have been developed. These phase function approximations and normalization techniques are described in detail in the following sub- sections.

3.2.3.1. Scattering Phase Function Approximations

Acute forward scattering peaks of particles lead to difficulties in numerical solution of RTE due to highly oscillatory behaviour and extensive computational requirement of Mie phase function. In order to overcome these difficulties, it is useful to represent the phase function with approximations. In this section, commonly known anisotropic scattering phase function approximations are described.

Linear Anisotropic Phase Function

It is the simplest approximation to Mie scattering phase function. The number of terms, N in Equation 3.16, required in the series is set to 1 and only first two terms of Equation 3.16 are included to simplify scattering phase function. The phase function can be expressed by

$$\Phi_{LA}(\theta) = 1 + g \cdot \cos \theta \quad (3.43)$$

where g and θ are the asymmetry factor and scattering angle, respectively. Integration over all solid angles shows that this phase function is normalized for any value of g [95]. Figure 3.1 shows linear anisotropic scattering phase function and unfortunately there is not significant discrepancy between forward scattering peak of the particles as the particles become highly anisotropic because of the smoothness of the function. As asymmetry factor of the medium increases the particles are expected to have strong forward scattering peaks; however, the linear anisotropic approximation does not represent the strong forward peaks, as seen in Figure 3.2, even for asymmetry factor of 0.9. Therefore, it is not a good approximation of scattering for the systems containing particles with acute forward scattering peaks. As also shown in Figure 3.2, radiation scattering for high anisotropy is not much different than that of isotropic scattering, for which g is 0.

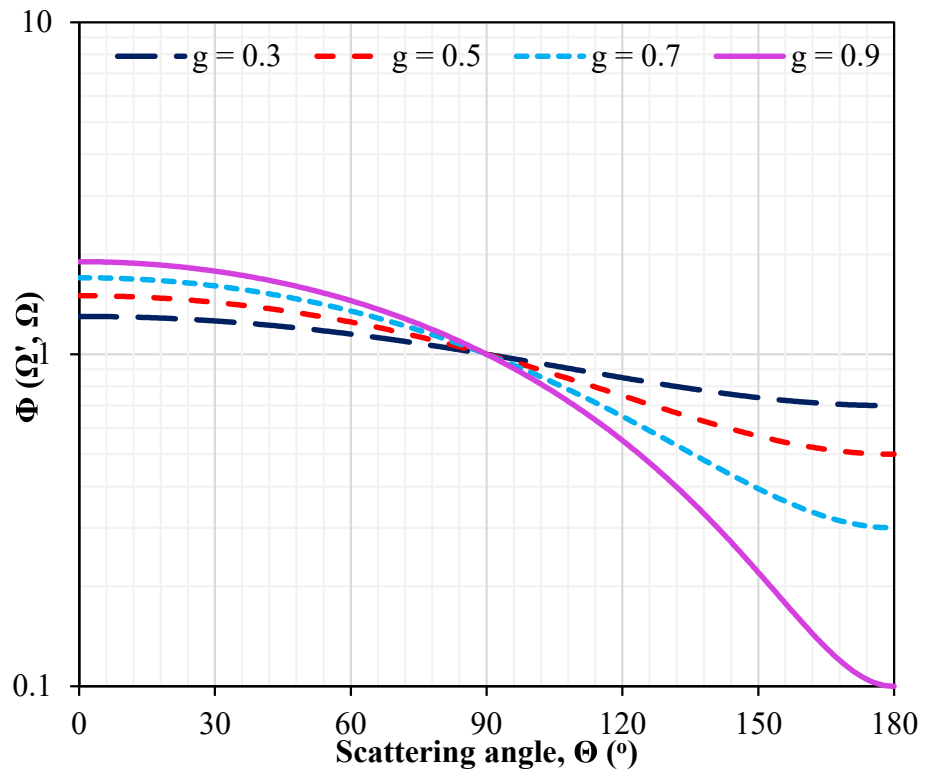


Figure 3.1 Phase function for linear anisotropic scattering

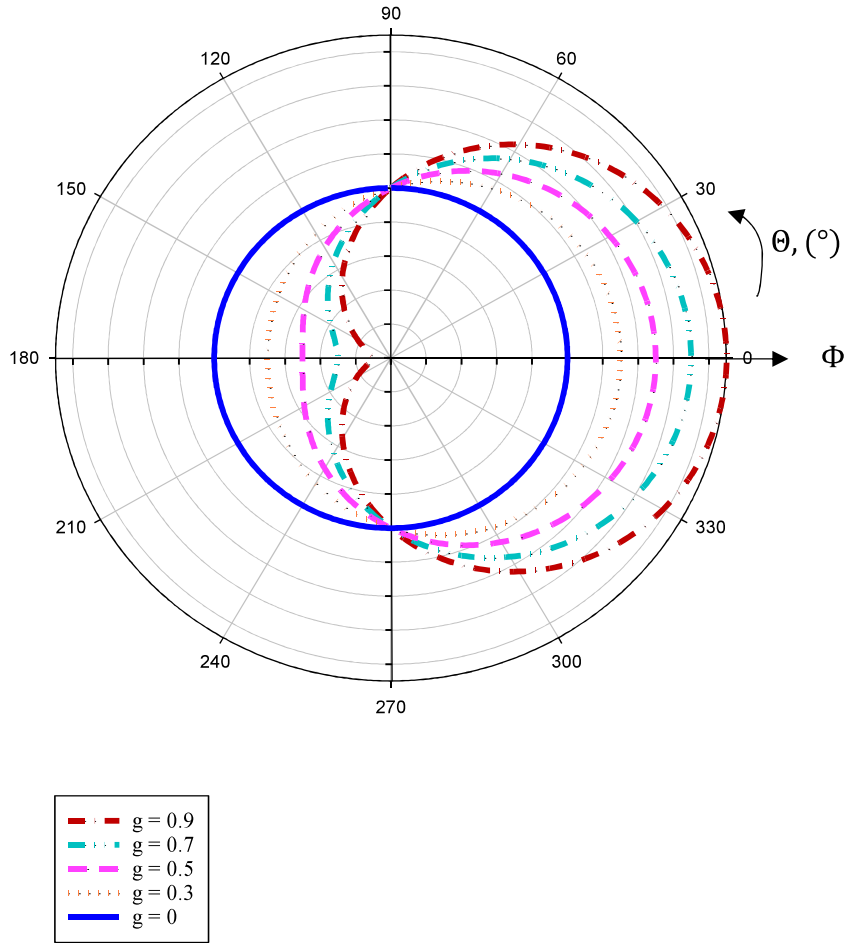


Figure 3.2 Polar plot for linear anisotropic scattering

Geometric Optics Phase Function

From the geometric optics view point, contribution of the diffraction and reflection to the scattering are calculated separately and then summed up to obtain overall scattering phase function. The part that is due to diffraction can be expressed by in terms of Bessel functions as follows:

$$\Phi_D(\Theta) = x^2 \left(\frac{2J_1(x \sin \Theta)}{x \sin \Theta} \right)^2 \quad (3.44)$$

where x , Θ and J_1 are size parameter, scattering angle and the 1st order Bessel function, respectively. Diffraction contribution to the scattering phase function is independent of the optical constants of the particle and is exclusively in the forward direction ($\Theta \sim 0$ to 6° depending on x) [93].

The contribution of reflection from large, opaque, diffusely reflecting and absorbing spheres is predominantly in the backward hemisphere and can be expressed by [95,96]

$$\Phi_R(\Theta) = \frac{8}{3\pi} (\sin \Theta - \Theta \cos \Theta) \quad (3.45)$$

Yu *et al.* [97] highlighted that agreement between GOA and Mie theory depends on particle size parameter. Predictions of scattered light intensity with GOA were benchmarked against those of Mie theory and were found to be in good agreement for large particles whereas GOA performs rather poor for particles with small size parameter. Therefore, GOA may lead to inaccurate representation of particle scattering when medium consists of both fine and coarse particles simultaneously.

Transport Approximation

According to this approximation, the forward scattering peak is represented by a Dirac delta function and the rest of the scattering is taken as isotropic. The phase function is obtained as

$$\Phi_{tr}(\Theta) = 2g\delta(1 - \cos \Theta) + (1 - g) \quad (3.46)$$

where g represents asymmetry factor. With the use of transport approximation, the RTE can be written in the same way as that for isotropic scattering; i.e. $\Phi = 1$ [94]. This is achieved by solving RTE as if the phase function is isotropic with the modified scattering coefficient:

$$\sigma_p^{tr} = \sigma_p(1 - g) \quad (3.47)$$

where σ_p is the particle scattering coefficient. It has been shown by Granate *et al.* [98] that transport approximation may lead to under prediction of the heat fluxes

with the increase in asymmetry factor since the phase function is treated as if it is isotropic and isotropic scattering is not capable of representing the acute forward scattering peaks of the particles sufficiently.

Delta – Eddington Phase Function

One of the widely used simplification is delta – Eddington. The approximation uses a two term Legendre polynomial expansion of the actual phase function plus a Dirac delta function in the forward direction and the phase function is obtained by

$$\Phi_{\delta E}(\theta) = 2f\delta(1 - \cos \theta) + (1 - f)(1 + 3g' \cos \theta) \quad (3.48)$$

where f and g' are forward scattering fraction and expansion coefficients, respectively and defined as

$$f = g^2 \quad \text{and} \quad g' = \frac{g - f}{1 - f} \quad (3.49)$$

Delta – Eddington phase function does not require normalization when DOM is implemented. The DOM predictions of the incident heat flux normalized by the emissive power with delta – Eddington approximation was investigated in a 3-D cubic enclosure containing purely scattering medium [98]. It is concluded that when the medium has an asymmetry factors up to 0.9 delta - Eddington performs better than transport approximation as in the latter scattering is treated as if it is isotropic with utilization of modified particle scattering coefficient in the RTE. Although delta - Eddington is widely used to represent acute forward scattering, Boulet *et al.* [99] showed that discrepancies between heat flux predictions of delta Eddington and Monte Carlo solutions are about 15%.

Delta – M Phase Function

Delta – M phase function is an extension of delta – Eddington approximation to higher orders of M . According to this approximation, strong forward scattering peak is represented by the Dirac delta function. Delta – M phase function [100] is expressed by

$$\Phi_{\delta M}(\theta) = 2f\delta(1 - \cos \theta) + (1 - f)\Phi^*(\theta) \quad (3.50)$$

where f is forward scattering fraction and $\Phi^*(\theta)$ is approximated phase function expressed by

$$\Phi^*(\theta) = \left(\sum_{n=0}^M A_n^* P_n(\cos \theta) \right) \quad (3.51)$$

In the above equation M represents the order of approximation. The value of f , M and A_n^* is important to represent the actual phase function because if the values of f and A_n^* are not found in a proper way, the phase function may become negative for some scattering angles, which is physically impossible [35]. Therefore, according to the order of approximation limiting conditions related to f and A_n^* are enforced to avoid negative scattering phase function and as the order of approximation increases criteria to be utilized would be complicated and so utilization of limiting conditions becomes tedious [101]. Moreover, the value of M is chosen arbitrarily for each system under consideration ($M = 1$ leads to delta – Eddington approximation). However, the choice should be made carefully. If M is too small, differences between the approximated and actual phase function are observed. Also any large value of M does not provide compatible representation of phase function with Mie theory and the detailed study related to proper M value selection was carried out by Granate *et al.* [98]. They also concluded that increase in M necessitates normalization of phase function with increasing asymmetry factor when DOM is used for RTE solution. Furthermore, M may be different for each system so it should be selected by comparing delta – M phase function prediction with that of Mie theory to ensure its accuracy. Therefore, ensuring the accuracy of this approximation without any doubt requires much more effort than utilization of a conventional phase function model.

Heney-Greenstein Phase Function

Another renowned phase function simplification is Heney-Greenstein as it provides good representation of Mie phase function when used together with

discrete ordinates and spherical harmonics methods [37, 95, 102]. It is only a function of scattering angle, Θ , and asymmetry factor, g , and is expressed by

$$\Phi_{\text{HG}}(\Theta) = \frac{1 - g^2}{(1 + g^2 - 2g \cos \Theta)^{1.5}} \quad (3.52)$$

Figure 3.3 shows scattering phase function approximated by Henyey Greenstein function. As can be seen from the figure, acute forward scattering peak of particles is well represented as the asymmetry factor is getting larger. Although Henyey Greenstein phase function needs to be normalized for large values of asymmetry factor when DOM discretization is implemented, CPU times required for the normalization of the scattering phase function are negligible even for optically thick medium [98].

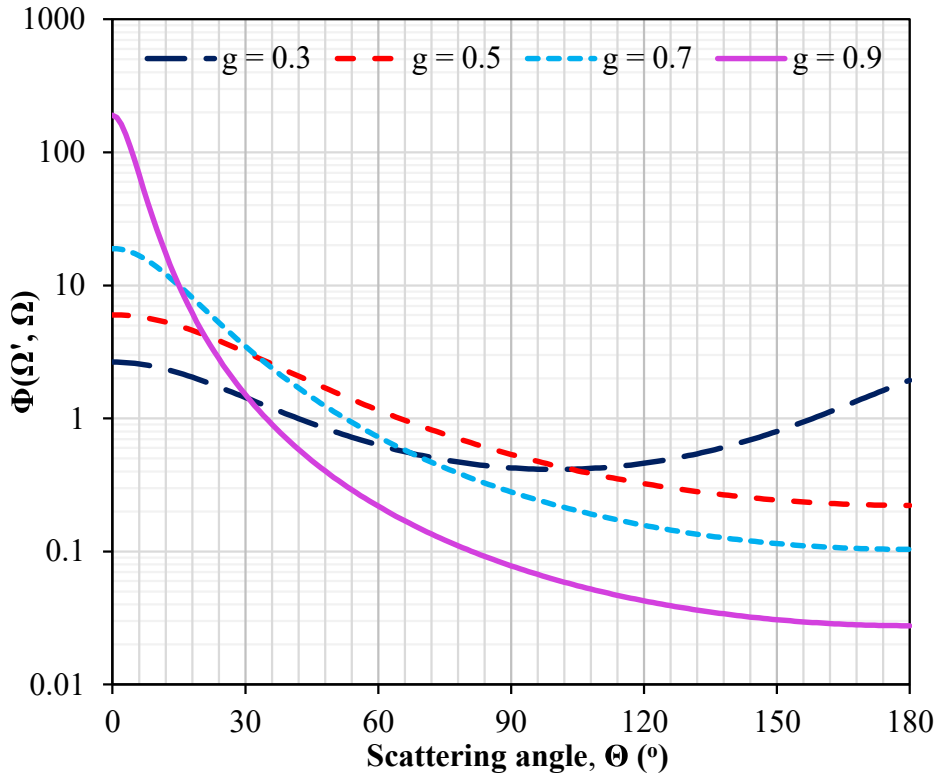


Figure 3.3 Henyey-Greenstein phase function

3.2.3.2. Scattering Phase Function Normalization Techniques

It is widely known that scattered energy in the system should be conserved after implementation of DOM discretization of the continuous angular variation of radiative intensity. In order to eliminate deviations in the conservation of scattered energy, the following criteria must be satisfied.

$$E_S = \frac{1}{4\pi} \sum_{m,\ell} \Phi(\boldsymbol{\Omega}_{m',\ell'}, \boldsymbol{\Omega}_{m,\ell}) w_{m,\ell} = 1 \quad (3.53)$$

where Φ and w represent scattering phase function and quadrature weight, respectively. When scattering is isotropic (i.e. $\Phi = 1$) equal amounts of radiation are scattered into all directions and the criteria for scattered energy conservation (Equation 3.53) is satisfied properly. However, as the scattering is getting strongly anisotropic it is known that DOM discretization violate scattered energy conservation criteria and hence results in incorrect radiation predictions or convergence problems in numerical solution of RTE.

Alteration in shape of the asymmetry factor changes the particle scattering properties and leads to incorrect radiation predictions. Not only scattered energy but also shape of the asymmetry factor should be preserved to represent the scattering behaviour of the particles accurately after the discretization. Thus, discretized phase function must satisfy the following criteria as well:

$$g = \frac{1}{4\pi} \sum_{m,\ell} \Phi(\boldsymbol{\Omega}_{m',\ell'}, \boldsymbol{\Omega}_{m,\ell}) w_{m,\ell} \cos \Theta (\boldsymbol{\Omega}_{m',\ell'}, \boldsymbol{\Omega}_{m,\ell}) \quad (3.54)$$

where Θ is the scattering angle between discrete directions $\boldsymbol{\Omega}_{m',\ell'}$ and $\boldsymbol{\Omega}_{m,\ell}$.

Therefore, normalization techniques have been developed in order to maintain conservation of both scattered energy and shape of the asymmetry factor.

Normalization of Wiscombe

The very first normalization method was proposed by Wiscombe [103]. Specific corrective factors for each individual direction is used in order to provide conservation of the scattered energy and the phase function is normalized as

$$\tilde{\Phi}(\mathbf{\Omega}_{m',\ell'}, \mathbf{\Omega}_{m,\ell}) = (1 + \gamma_{m,\ell} + \gamma_{m',\ell'}) \times \Phi(\mathbf{\Omega}_{m',\ell'}, \mathbf{\Omega}_{m,\ell}) \quad (3.55)$$

where $\gamma_{m,\ell}$ and $\gamma_{m',\ell'}$ are solutions to the system of equations

$$\frac{1}{4\pi} \sum_{m,\ell} (1 + \gamma_{m,\ell} + \gamma_{m',\ell'}) \Phi(\mathbf{\Omega}_{m',\ell'}, \mathbf{\Omega}_{m,\ell}) w_{m,\ell} = 1 \quad (3.56)$$

Boulet *et al.* [99] showed that this normalization technique leads to over prediction of the heat fluxes when compared with finite volume method and Monte Carlo solutions for highly anisotropic scattering as preservation of asymmetry factor is not considered.

Normalization of Kim and Lee

One of the commonly known method to conserve scattered energy was proposed by Kim and Lee [68]. According to this normalization method, scattering phase function is multiplied by a normalization coefficient that is inverse of scattered energy conservation criteria for the specific radiation direction $\mathbf{\Omega}_{m',\ell'}$ and as a result new phase function is obtained by,

$$\tilde{\Phi}(\mathbf{\Omega}_{m',\ell'}, \mathbf{\Omega}_{m,\ell}) = \Phi(\mathbf{\Omega}_{m',\ell'}, \mathbf{\Omega}_{m,\ell}) \times \left(\frac{1}{4\pi} \sum_{m,\ell} \Phi(\mathbf{\Omega}_{m',\ell'}, \mathbf{\Omega}_{m,\ell}) w_{m,\ell} \right)^{-1} \quad (3.57)$$

Although the normalization technique satisfies Equation 3.53, it has been shown that implementation of Kim and Lee's normalization does not necessarily conserve the phase function asymmetry factor for strongly forward scattering hence leads to poor radiative heat transfer predictions [98, 99, 104-106].

Normalization of Mishchenko et al.

Mishchenko and his coworkers proposed another normalization method for conservation of scattered energy. Considering that the magnitude of the forward scattering term (where $\cos\theta=1$) was significantly larger than the remaining discrete phase function directions for strong forward scattering Henyey-Greenstein phase function [107], they suggested that rather than normalizing every direction of scattering phase function, normalization of only forward scattering term is sufficient for scattering energy preservation. The normalized value of the forward scattering phase function is expressed by

$$\tilde{\Phi}(\mathbf{\Omega}_{m',\ell'}, \mathbf{\Omega}_{m',\ell'}) = (1 + A_{m',\ell'}) \times \Phi(\mathbf{\Omega}_{m',\ell'}, \mathbf{\Omega}_{m',\ell'}) \quad (3.58)$$

where $A_{m',\ell'}$ is the forward – scattering normalization vector parameter and expressed as follows [108]:

$$A_{m',\ell'} = \frac{4\pi - \sum_{m,\ell} \Phi(\mathbf{\Omega}_{m',\ell'}, \mathbf{\Omega}_{m,\ell}) W_{m,\ell}}{\Phi(\mathbf{\Omega}_{m',\ell'}, \mathbf{\Omega}_{m',\ell'}) W_{m',\ell'}} \quad (3.59)$$

However, this normalization technique does not guarantee conservation of phase function asymmetry factor hence leads to incorrect radiation predictions as noted by [107]. Another drawback of the method is that it is only valid for forward scattering phase functions ($g > 0$). For backward scattering problems ($g < 0$) Equation 3.59 must be re-derived so that the backward scattering phase function term is normalized [107]. Hence, it is just a simpler alternative of Kim and Lee normalization method since only forward scattering term is conserved [107].

Normalization of Kamden Tagne

Kamden Tagne proposed another normalization procedure by extending the normalization procedure of Mishchenko *et al.* in order to conserve asymmetry factor after discretization. Similar to Mishchenko *et al.*, only forward scattering term conservation was thought to be sufficient, as shown in Equation 3.58. The asymmetry factor conservation condition, Equation 3.54, is taken as basis for

calculation of the normalization parameters. After implementation of normalization, Equation 3.54 is expressed as:

$$\begin{aligned} & \frac{1}{4\pi} \sum_{m,\ell} \Phi(\boldsymbol{\Omega}_{m',\ell'}, \boldsymbol{\Omega}_{m,\ell}) w_{m,\ell} \cos \Theta(\boldsymbol{\Omega}_{m',\ell'}, \boldsymbol{\Omega}_{m,\ell}) + \\ & \frac{1}{4\pi} (1 + A_{m',\ell'}) \times \Phi(\boldsymbol{\Omega}_{m',\ell'}, \boldsymbol{\Omega}_{m',\ell'}) w_{m',\ell'} \cos \Theta(\boldsymbol{\Omega}_{m',\ell'}, \boldsymbol{\Omega}_{m',\ell'}) = g \end{aligned} \quad (3.60)$$

where $A_{m',\ell'}$ is the forward – scattering normalization vector parameter and expressed by

$$A_{m',\ell'} = \frac{(4\pi g - \sum_{m,\ell} \Phi(\boldsymbol{\Omega}_{m',\ell'}, \boldsymbol{\Omega}_{m,\ell}) w_{m,\ell} \cos \Theta(\boldsymbol{\Omega}_{m',\ell'}, \boldsymbol{\Omega}_{m,\ell}))}{\Phi(\boldsymbol{\Omega}_{m',\ell'}, \boldsymbol{\Omega}_{m',\ell'}) w_{m',\ell'}} \quad (3.61)$$

where the denominator is simplified by the fact that $\cos \Theta(\boldsymbol{\Omega}_{m',\ell'}, \boldsymbol{\Omega}_{m,\ell}) = 1$. Although this technique has an advantage over the previous normalization methods by conserving the asymmetry factor, preservation of scattered energy is not guaranteed and hence it could result in inaccurate radiative heat transfer predictions [107].

Normalization of Hunter and Guo

In an optimal normalization procedure, both conservation of scattered energy and phase function asymmetry factor should be satisfied simultaneously to eliminate the errors in radiative heat transfer predictions. All above normalization methods are capable of conserving either scattered energy or phase function asymmetry factor; that is, the both quantities cannot be preserved simultaneously. Therefore, Hunter and Guo proposed another normalization procedure to eliminate both deviations in the conservation of scattered energy and alterations in asymmetry factor at the same time. In this normalization technique scattering phase function values are normalized as

$$\tilde{\Phi}(\boldsymbol{\Omega}_{m',\ell'}, \boldsymbol{\Omega}_{m,\ell}) = (1 + A_{m',\ell',m,\ell}) \times \Phi(\boldsymbol{\Omega}_{m',\ell'}, \boldsymbol{\Omega}_{m,\ell}) \quad (3.62)$$

where the normalization parameter $A_{m',\ell',m,\ell}$ are determined such that $\tilde{\Phi}(\mathbf{\Omega}_{m',\ell'}, \mathbf{\Omega}_{m,\ell})$ satisfies the Equations 3.53 and 3.54 simultaneously, as well as a directional symmetry condition ($\tilde{\Phi}(\mathbf{\Omega}_{m',\ell'}, \mathbf{\Omega}_{m,\ell}) = \tilde{\Phi}(\mathbf{\Omega}_{m,\ell}, \mathbf{\Omega}_{m',\ell'})$) [107]. The validity of DOM predictions with this normalization procedure is shown in literature by comparing predictions of finite volume method (FVM) [98, 104, 109] and Monte Carlo (MC) solutions [98, 110, 111]. However, this normalization method requires predetermination of normalization parameter which necessitates more computational effort [106] and does not take into account backward scattering term. Therefore, Hunter and Guo have recently suggested a new normalization technique in which backward scattering term is normalized in addition to the forward scattering term to provide conservation of the scattered energy and phase function asymmetry factor simultaneously [107]. According to the method, Equations 3.53 and 3.54 are still valid but only the forward and backward scattering terms are normalized with normalization parameters $A_{m',\ell'}$ and $B_{m'^-, \ell'^-}$ expressed as follows:

$$\tilde{\Phi}(\mathbf{\Omega}_{m',\ell'}, \mathbf{\Omega}_{m',\ell'}) = (1 + A_{m',\ell'})\Phi(\mathbf{\Omega}_{m',\ell'}, \mathbf{\Omega}_{m',\ell'}) \quad (3.63)$$

$$\tilde{\Phi}(\mathbf{\Omega}_{m',\ell'}, \mathbf{\Omega}_{m'^-, \ell'^-}) = (1 + B_{m'^-, \ell'^-})\Phi(\mathbf{\Omega}_{m',\ell'}, \mathbf{\Omega}_{m'^-, \ell'^-}) \quad (3.64)$$

where

$$A_{m',\ell'} = \frac{1}{2\Phi(\mathbf{\Omega}_{m',\ell'}, \mathbf{\Omega}_{m'^-, \ell'^-})W_{m',\ell'}} \times \left(4\pi(1 + g) - \sum_{m,\ell}^{M,L} \Phi(\mathbf{\Omega}_{m',\ell'}, \mathbf{\Omega}_{m,\ell})W_{m,\ell} (1 + \cos \Theta(\mathbf{\Omega}_{m',\ell'}, \mathbf{\Omega}_{m,\ell})) \right) \quad (3.65)$$

$$B_{m',\ell'} = \frac{1}{2\Phi(\boldsymbol{\Omega}_{m',\ell'}, \boldsymbol{\Omega}_{m',\ell'})W_{m',\ell'}} \times \quad (3.66)$$

$$\left(4\pi(1 - g) - \sum_{m,\ell}^{M,L} \Phi(\boldsymbol{\Omega}_{m',\ell'}, \boldsymbol{\Omega}_{m,\ell})W_{m,\ell}(\cos \Theta(\boldsymbol{\Omega}_{m',\ell'}, \boldsymbol{\Omega}_{m,\ell}) - 1) \right)$$

Predictions of DOM with this normalization technique were benchmarked against those of Monte Carlo and finite volume method and were found to be in good agreement with benchmark solutions [107]. Moreover, the normalization technique is tested for an axisymmetric cylindrical enclosure with optically thin and thick media [98]. The results with this normalization are benchmarked against finite volume method and the results are in good agreement with each other for various asymmetry factor. It is also shown that CPU times required for the normalization of scattering phase function are negligible.

CHAPTER 4

0.3 MW_t METU ABFBC TEST RIG

In this chapter, 0.3 MW_t Middle East Technical University (METU) Atmospheric Bubbling Fluidized Bed Combustor (ABFBC) Test Rig and its operating conditions are described to provide necessary parameters for radiative property estimation of the medium. The input data required for the model and its validation were provided from the experimental data, which was previously taken from METU 0.3 MW_t ABFBC Test Rig operating with and without recycle of fine particles.

4.1. Description of the Test Rig

The main body of the test rig is a modular combustor formed by five modules of internal cross section of 0.45 m × 0.45 m and 1 m height. Inner walls of the modules are lined with alumina based refractory bricks of 6 cm thickness and insulated. The first and fifth modules from the bottom refer to bed and cooler, respectively, and the ones in between are the freeboard modules. There exist two cooling surfaces in the modular combustor, one in the bed and the other in the cooler, providing 0.35 m² and 4.3 m² of cooling surfaces, respectively. There are 14 ports for thermocouples and 10 ports for gas sampling probes along the combustor. In order to measure concentrations of O₂, CO, CO₂, SO₂ and NO_x along the combustor at steady state, combustion gas is sampled from the combustor via gas sampling probes and is transferred through a heated line to the gas conditioning system, where the sample is filtered, dried and cooled to be fed to analyzers. After measurement of species concentration, sample gas is vented to the atmosphere. In addition to thermocouple and gas sampling probes, two ports for feeding coal/limestone mixture are provided

in the bed module, one 0.22 m and the other 0.85 m above the distributor plate. The process values such as flow rates and temperatures of each stream, gas composition and temperature along the combustor are logged to a PC by means of a data acquisition and control system, Bailey INFI 90. The flow sheet of 0.3 MW_t METU ABFBC test rig is shown in Figure 4.1 and further details of the test rig can be found in elsewhere [20,63,112].

Radiative heat fluxes incident on the refractory side walls of the freeboard were measured by water cooled radiometer with Medtherm 48P-20-22K heat flux transducer during the steady state operation of the test rig. Details of transducer are available in elsewhere [20]. The radiometer eliminates the effects of convection and measures only the incident radiative heat flux. The radiometer probe was inserted into the gas sampling ports at five different heights along freeboard flush with the inner surface of the refractory side wall. The radiometer output for incident radiative heat flux was read by using Medtherm H-201 digital heat flux meter with certified calibration

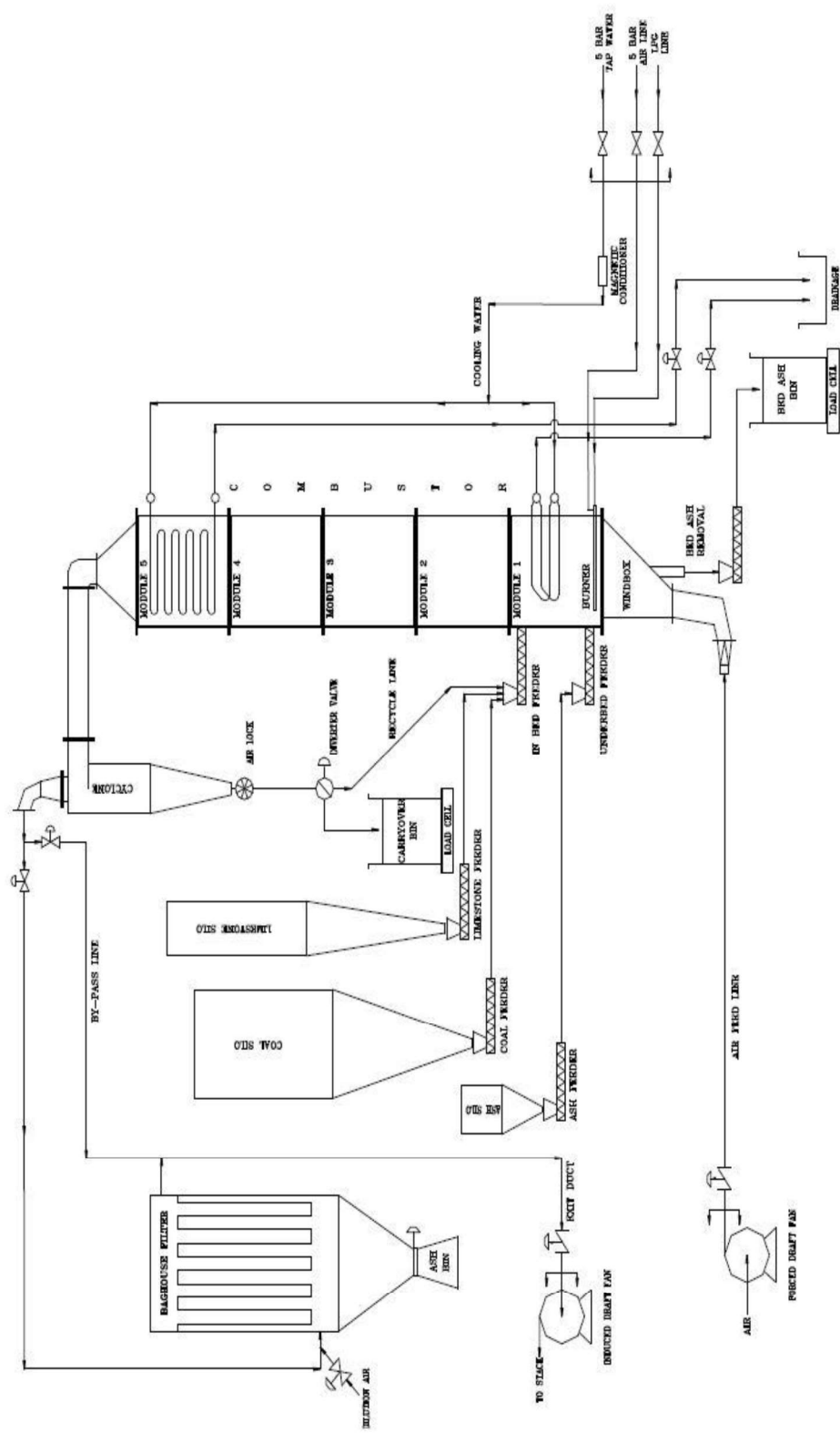


Figure 4.1 Flow sheet of 0.3 MW_t METU ABFBC Test Rig [63]

4.2. Operating Conditions

Experiments were carried out with typical low calorific value, high volatile matter/fixed carbon (VM/FC) ratio and high ash content Beypazarı lignite in two sets; one without and the other with addition of limestone [113]. In both sets, the lignite was burnt in its own ash. Experiments conducted without limestone addition are taken into consideration in this study. Representative samples from the coal were subjected to sieve analyses and proximate and ultimate analyses. The results of these analyses are shown in Table 4.1.

Table 4.1 Characteristics of Beypazarı Lignite

Sieve Analysis		Proximate Analysis (as received)		Ultimate Analysis (dry)	
Size (mm)	Weight (%)	Component	Weight (%)	Component	Weight (%)
4.000 – 3.350	11.5	Moisture	13.7	C	38.1
3.350 – 2.360	20.2	Ash	36.4	H	3.2
2.360 – 2.000	17.7	VM	32.7	O	12.4
2.000 – 1.700	16.8	FC	17.2	N	1.4
1.700 – 1.180	15.7	LHV =12.5 MJ/kg $\rho_{\text{bulk}} = 905 \text{ kg/m}^3$		S _{combustible}	2.7
1.180 – 0.710	12.2			S _{total}	4.5
0.710 – 0.000	5.9			Ash	42.2

Radiative heat flux measurements were carried out in two combustion tests, one without (test case 1) and the other (test case 2) with recycle of fine particles. Freeboard fly ash particle load is taken as the sum of the particles collected by cyclone and baghouse filter. Particle load determination in the test with recycle needs further elaboration of the recycling system of the combustor under consideration as follows. Cyclone catch particles pass through an air lock (i.e., a rotary valve) and fall onto a diverter. Depending on the position of the diverter, particles are either discharged from the system to a continuously weighted ash storage bin (load cell) for experiments without recycle or flow back to the combustor for re-firing. The fraction of a short time interval over which the position of diverter

remains on the recycle mode determines the recycle ratio. Continuity of flow is provided by repeating this time interval periodically. In order to provide a wider range of recycle ratio and yet not to disturb the steady state conditions within the combustor, a periodic time interval of 10 s was selected. For experiment with recycle (test case 2), the diverter remains nine units of time on the recycle mode and one unit of time on no recycle mode. Cyclone flow rate (26.58 kg/h) shows the flow rate of particles in no recycle mode for one unit of time, which gives the recycle flow rate when multiplied by 9. Recycle flow rate of 239.22 kg/h leads to an order of magnitude increase in particle loading. Table 4.2 lists some of the operating conditions of the two experiments at steady-state. Further experimental details of the test cases can be found in elsewhere [63].

For radiative property estimation of particle laden combustion gases, particles collected from both cyclone and baghouse downstream of the freeboard are subjected to sieve analysis and laser light scattering technique for particle size distribution. Additive rule is applied to obtain actual size distribution in the freeboard and final particle size distributions (PSD) for both combustion tests are shown in Figure 4.2. The properties of the cyclone and baghouse filter streams required for the radiative property estimation are presented in Table 4.3. Mineral composition of the fly ash particles for both test cases are shown in Table 4.4. Temperature measurements were conducted on a discrete grid of points along the freeboard at steady state operation. Figure 4.3 shows the temperature profiles along the freeboard region for test case 1 and 2, respectively. In order to facilitate the use of these measurements as input data in the calculation of radiative exchange, the experimental data were represented by high order polynomials given in Table 4.5.

Table 4.2 Operating conditions of the experiments

	Test case 1	Test case 2
Coal flow rate (kg/h)	101	101
Cyclone ash flow rate (kg/h)	23.65	26.58
Baghouse filter ash flow rate (kg/h)	1.08	3.43
Recycle ratio*	0.0	2.37
Air flow rate (kmol/h)	22	21
Excess air (%)	43	36
Superficial velocity (m/s)	3.0	2.8
Particle load, B (kg/m ³)	0.011	0.131
Average bed temperature (K)	1148	1119
Average freeboard temperature (K)	1120	1178
Average H ₂ O concentration (%)	10	10
Average CO ₂ concentration (%)	10	11

*Recycle ratio = (Recycle flow rate)/(Coal flow rate)

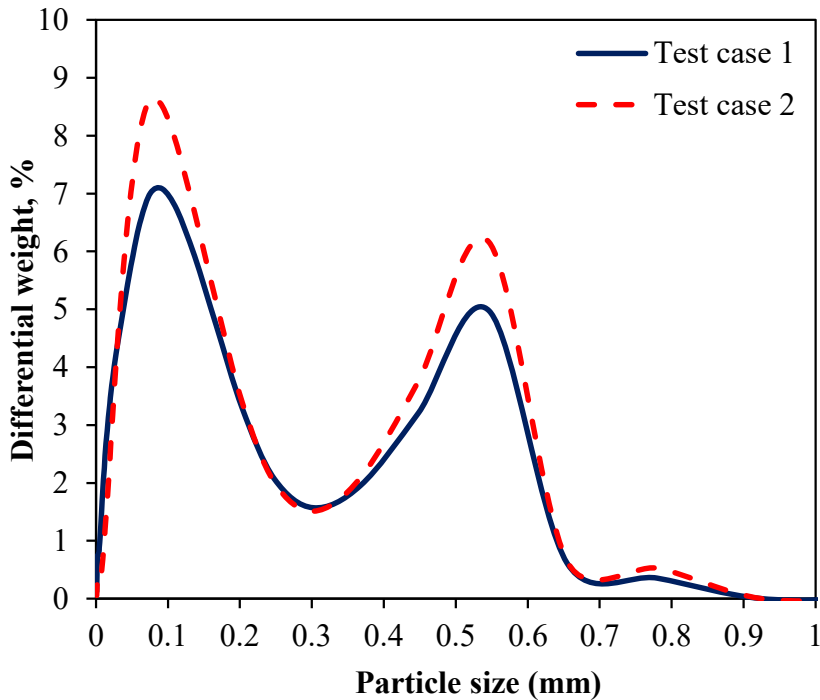


Figure 4.2 Particle size distribution for test case 1 and test case 2

Table 4.3 Properties of fly ash streams

	Test case 1	Test case 2
Cyclone		
Particle density (kg/m ³)	1029	931
Particle size range (µm)	0.5<d _p <850	0.5<d _p <850
Particle load (kg/m ³)	0.011	0.129
Baghouse filter		
Particle density (kg/m ³)	536	633
Particle size range (µm)	0.5<d _p <124	0.5<d _p <68
Particle load (kg/m ³)	0.0005	0.0017

Table 4.4 Fly ash compositions

Component	Weight (%)	
	Test case 1	Test case 2
SiO ₂	45.71	47.26
Al ₂ O ₃	16.42	16.87
Fe ₂ O ₃	13.46	13.16
CaO	0.40	0.44
MgO	1.00	1.01
TiO ₂	5.06	3.62
K ₂ O	2.25	1.89
SO ₃	8.87	8.72
Na ₂ O	6.82	7.03

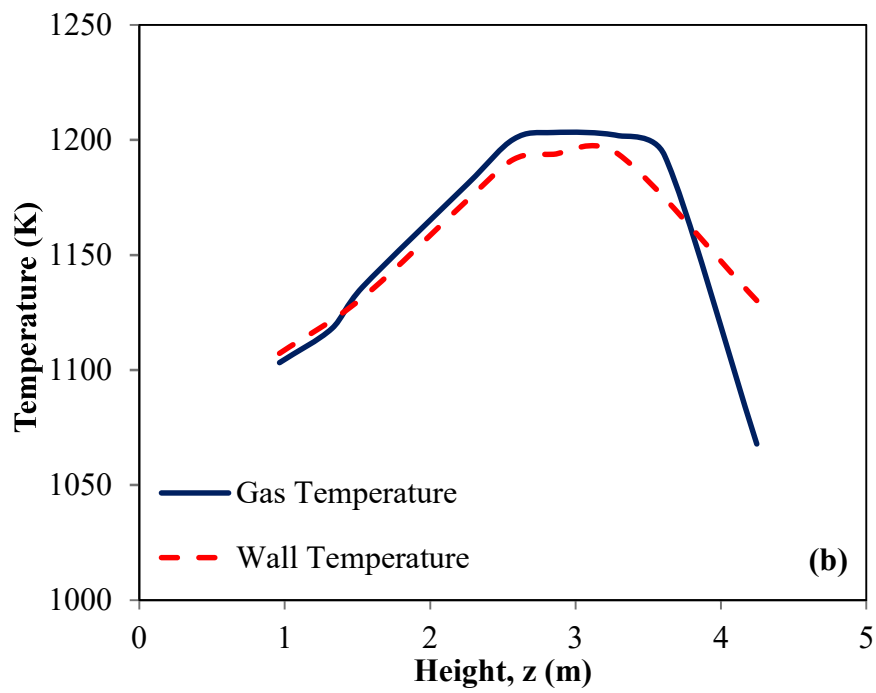
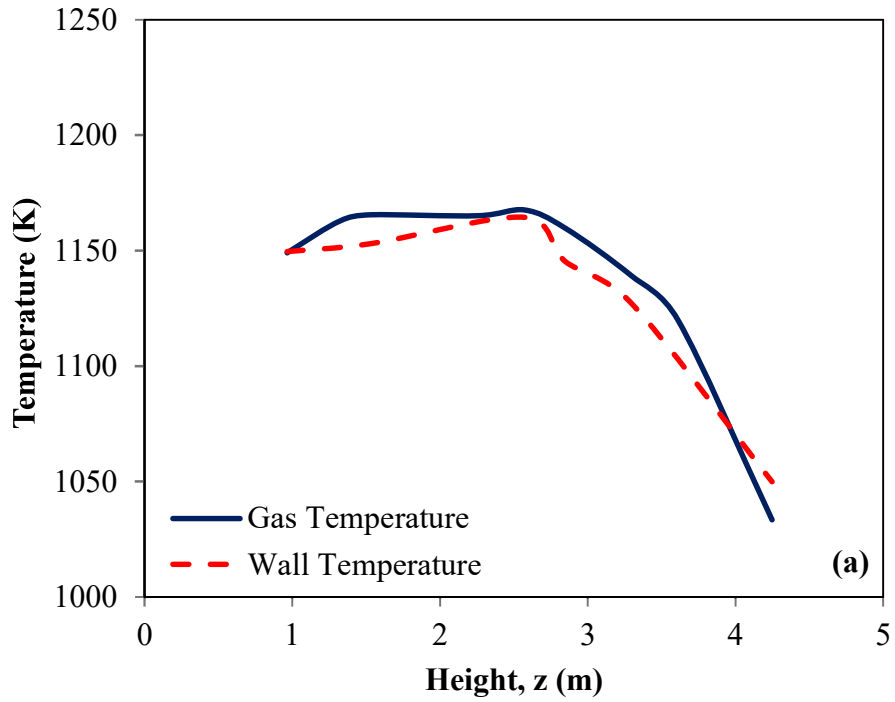


Figure 4.3 Temperature profiles along the freeboard for (a) test case 1 and (b) test case 2

Table 4.5 Polynomials for temperature profiles

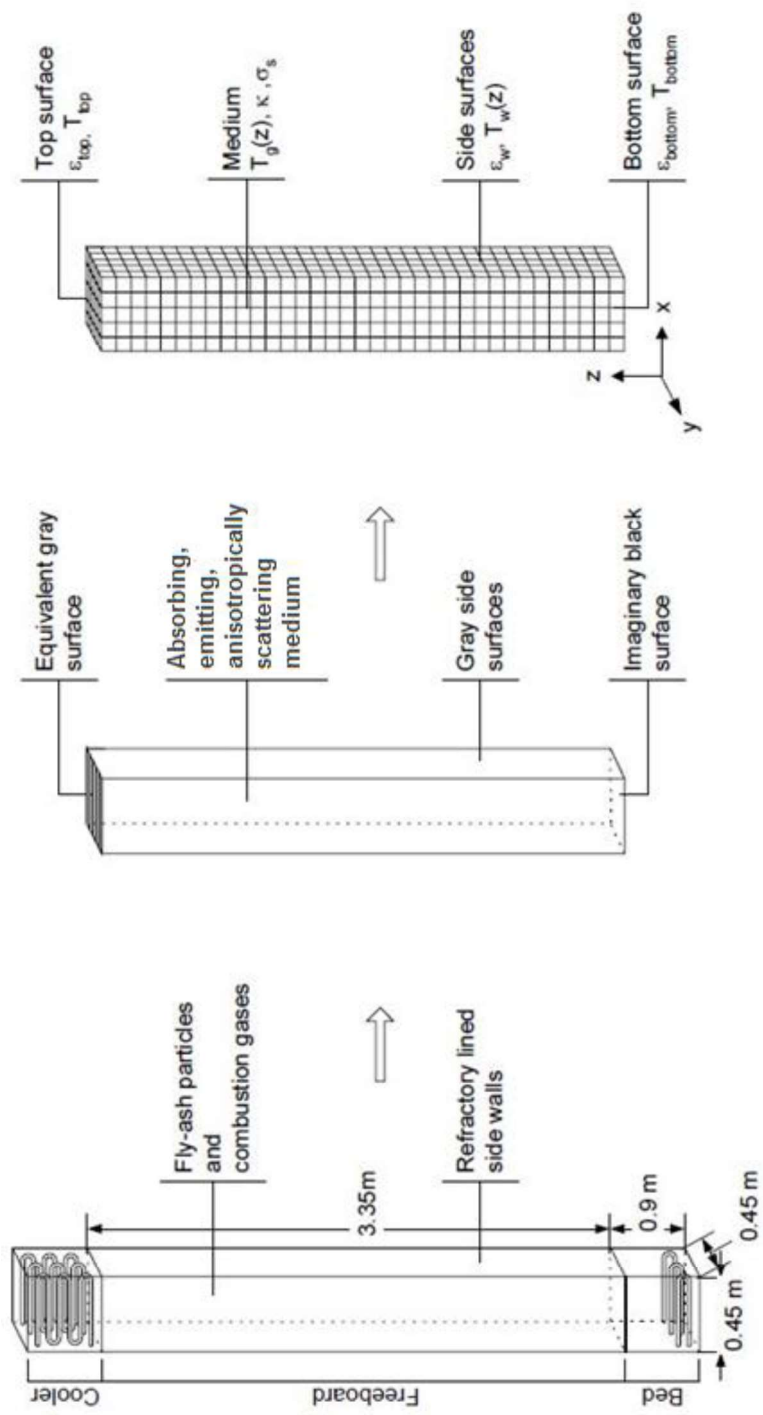
	Test case 1	Test case 2
<p>Medium temperature profile (K)</p> $T_m(z) = \sum_{i=0}^6 a_i z^i$	<p>$a_0 = 1149.66$</p> <p>$a_1 = -15.50$</p> <p>$a_2 = -1.351$</p> <p>$a_3 = 42.65$</p> <p>$a_4 = -30.56$</p> <p>$a_5 = 7.84$</p> <p>$a_6 = -0.71$</p>	<p>$a_0 = 1106.52$</p> <p>$a_1 = 16.62$</p> <p>$a_2 = -90.85$</p> <p>$a_3 = 116.33$</p> <p>$a_4 = -50.22$</p> <p>$a_5 = 9.59$</p> <p>$a_6 = -0.73$</p>
<p>Wall temperature profile (K)</p> $T_w(z) = \sum_{i=0}^6 b_i z^i$	<p>$b_0 = 1146.50$</p> <p>$b_1 = 40.50$</p> <p>$b_2 = -129.23$</p> <p>$b_3 = 137.01$</p> <p>$b_4 = -62.89$</p> <p>$b_5 = 13.14$</p> <p>$b_6 = -1.04$</p>	<p>$b_0 = 1110.44$</p> <p>$b_1 = 61.59$</p> <p>$b_2 = -226.77$</p> <p>$b_3 = 246.25$</p> <p>$b_4 = -106.20$</p> <p>$b_5 = 20.58$</p> <p>$b_6 = -1.52$</p>

4.3. Approximation of the Freeboard as a 3 – D Radiation Problem

In order to apply the radiation models to the freeboard, it is required to provide temperatures and radiative properties of the medium and surrounding surfaces properly. The physical system under consideration is the freeboard region of METU 0.3 MW_t Atmospheric Bubbling Fluidized Bed Combustor (ABFBC). Freeboard is treated as a 3-D rectangular enclosure containing grey absorbing, emitting gas with grey absorbing, emitting and non/isotropically/anisotropically scattering particles surrounded by grey/black diffuse walls. The cooler boundary at the top, which consists of gas lanes and cooler tubes, is represented by an equivalent grey surface of effective emissivity and temperature related to area weighted average emissivity and emissive power of the components, respectively. Details of the treatment of tube-row/gas lane combination can be found elsewhere [20]. The boundary with the bed section at the bottom is represented as a black surface due to Hohlraum effect [20]. The side walls are taken as grey, diffuse walls. Table 4.6 shows the radiative properties of the surrounding surfaces. The physical system and the treatment of the freeboard section are schematically illustrated in Figure 4.4.

Table 4.6 Radiative properties of the surrounding surfaces

	Test case 1	Test case 2
Temperature of top surface, T_{top} (K)	908	940
Temperature of bottom surface, T_{bottom} (K)	1144	1103
Emissivity of top surface, ϵ_{top}	0.87	0.87
Emissivity of bottom surface, ϵ_{bottom}	1.00	1.00
Emissivity of side surfaces, ϵ_w	0.33	0.33



The physical system: Freeboard of the ABFBC and its boundaries Treatment of the freeboard as a 3-D rectangular enclosure Solution domain and boundary conditions used in MOL solution of DOM

Figure 4.4 Treatment of freeboard as a 3-D enclosure and solution domain [48]

In addition to radiative properties of the surrounding surfaces, estimation of radiative properties of the particle laden combustion gases consisting of CO₂, H₂O and fly ash particles bounded by the freeboard walls is necessary to provide accurate representation of radiative heat transfer. The radiative properties of the medium are assumed to be uniform and constant throughout the freeboard. This assumption is based on uniform CO₂ and H₂O concentrations measured along the freeboard and the fact that particle concentration and size distribution can be represented by the material sampled from the cyclone and baghouse filter [113]. For calculating the radiative properties of the particle laden combustion gases within the METU ABFBC Test Rig, temperature and gas composition data are obtained from [113].

CO₂ and H₂O concentrations are important for radiative heat transfer due to the fact that these gases have strong absorption bands in the spectrum at high temperatures. Therefore, only CO₂ and H₂O are taken into account for radiative transfer in this study. Table 4.2 shows concentration of CO₂ and H₂O in the freeboard region. Several studies have shown that radiative heat flux and source term predictions are not much affected by spectral gas property models in the presence of particles [28-30] as the particle radiation dominates total radiation [31-34]. Therefore, gas properties are approximated as grey and estimated by using Grey Gas model (see section 3.1.1) throughout the study. Table 4.7 and Table 4.8 show required input data for calculation of radiative properties and estimated radiative properties of the participating combustion gases, respectively.

Table 4.7 Input data for calculation of radiative properties of the participating combustion gases

	Test case 1	Test case 2
P_{CO2} (bar)	0.10	0.10
P_{H2O} (bar)	0.10	0.11
L_m (m)	0.38	0.38
T_{gas} (K)	1144	1163

Table 4.8 Radiative properties of the gases

	Test case 1	Test case 2
Transmissivity of gas, τ_g	0.847	0.847
Emissivity of gas, ε_g	0.153	0.153
Gas absorption coefficient, κ_g (m^{-1})	0.438	0.437

Radiative properties of the particles depend on particle loading, refractive index, shape and size of the particles. The ash content of the fly ash particles determined by chemical analysis was 98 % indicating that particles are treated as pure ash in radiative property estimation. For grey particle properties, both Mie theory and geometric optics approximations (GOA) are used considering that over 88 and 78 wt % of the fly ash particles have a size parameter greater than 25 in test case 1 and test case 2, respectively (see section 3.2). In grey Mie calculations, wavelength independent refractive index of $m = 1.5-0.02i$ is used [114] and size parameter is calculated by using a representative wavelength of $3 \mu m$ as suggested in [35]. In GOA, total hemispherical reflectivity of particles is found as 0.854 by numerically integrating directional-hemispherical reflectivities obtained from the Fresnel's relations over all directions [42]. Particle radiative properties predicted by Mie theory and GOA are illustrated in Table 4.9 and Table 4.10, respectively. Anisotropic scattering of radiation by the grey particles are taken into consideration by deploying Henyey-Greenstein phase function because of its mathematical simplicity and its ability to represent acute forward scattering peaks of particles accurately (see section 3.2.3.1). Phase function normalization method proposed by Hunter and Guo [107] is applied to conserve both the scattered energy and shape of the phase function (see section 3.2.3.2). Furthermore, independent scattering is assumed to take place in the freeboard region of the test rig considering the size parameter and particle volume fraction, which is in the order of 10^{-5} and 10^{-4} for test case 1 and 2, respectively.

Table 4.9 Radiative properties of the fly ash particles predicted by Mie theory

	Test case 1	Test case 2
Absorption coefficient of the particles, κ_p (m^{-1})	0.43	3.78
Scattering coefficient of the particles, σ_s (m^{-1})	1.36	8.34
Asymmetry factor, g	0.76	0.82

Table 4.10 Radiative properties of the fly ash particles predicted by GOA

	Test case 1	Test case 2
Absorption coefficient of the particles, κ_p (m^{-1})	0.66	4.68
Scattering coefficient of the particles, σ_s (m^{-1})	0.89	6.28
Asymmetry factor, g	0.91	0.94

4.4. Input Data for the Radiation Model

Radiative properties of particle laden combustion gases and surrounding surfaces are summarized in Tables 4.11 and 4.12. These data together with medium and side wall temperature profiles given in Figure 4.3 provide the input data supplied to the radiation models.

Table 4.11 Input data for radiation model with Mie theory

	Test case 1	Test case 2
Particle load, B (kg/m ³)	0.011	0.13
Particle density, ρ_p (kg/m ³)	1007	927
Absorption coefficient of the gas, κ_g (m ⁻¹)	0.44	0.44
Absorption coefficient of the particles, κ_p (m ⁻¹)	0.43	3.78
Scattering coefficient of the particles, σ_s (m ⁻¹)	1.36	8.34
Extinction coefficient of the medium, β (m ⁻¹)	2.23	12.56
Scattering albedo of the medium, ω	0.61	0.66
Asymmetry factor, g	0.76	0.82
Mean beam length, L_m (m)	0.38	0.38
Optical thickness, τ	0.85	4.77
Size parameter, x	23.3	40.5
Particle volume fraction	10^{-5}	10^{-4}
Temperature of top surface, T_{top} (K)	908	940
Temperature of bottom surface, T_{bottom} (K)	1144	1103
Emissivity of top surface, ϵ_{top}	0.87	0.87
Emissivity of bottom surface, ϵ_{bottom}	1.00	1.00
Emissivity of side surfaces, ϵ_{side}	0.33	0.33

Table 4.12 Input data for radiation model with GOA

	Test case 1	Test case 2
Particle load, B (kg/m ³)	0.011	0.13
Particle density, ρ_p (kg/m ³)	1007	927
Absorption coefficient of the gas, κ_g (m ⁻¹)	0.44	0.44
Absorption coefficient of the particles, κ_p (m ⁻¹)	0.66	4.68
Scattering coefficient of the particles, σ_s (m ⁻¹)	0.89	6.28
Extinction coefficient of the medium, β (m ⁻¹)	1.98	11.40
Scattering albedo of the medium, ω	0.45	0.55
Asymmetry factor, g	0.91	0.94
Mean beam length, L_m (m)	0.38	0.38
Optical thickness, τ	0.75	4.33
Size parameter, x	23.3	40.5
Particle volume fraction	10^{-5}	10^{-4}
Temperature of top surface, T_{top} (K)	908	940
Temperature of bottom surface, T_{bottom} (K)	1144	1103
Emissivity of top surface, ϵ_{top}	0.87	0.87
Emissivity of bottom surface, ϵ_{bottom}	1.00	1.00
Emissivity of side surfaces, ϵ_{side}	0.33	0.33

CHAPTER 5

RESULTS AND DISCUSSION

In this chapter, GOA and scattering phase function simplifications are evaluated from the viewpoints of predictive accuracy and computational efficiency by applying them to the test cases described in Chapter 4. Performance of GOA and scattering phase function simplifications are assessed by comparing their predictions with measurements available in the literature [63]. The effects of angular and spatial discretization on the predictions of incident heat flux and source term, validation of the model predictions against measurements and predictive accuracy and computational efficiency of both GOA and scattering phase function simplifications for the test cases involving different optical thicknesses are presented in the following sections of this chapter.

For all test cases, which are described in Chapter 4, the S_N angular quadrature scheme proposed by Carlson and Lathrop [81] is selected. The choice is based on an assessment study carried out by Selçuk and Kayakol [69]. Radiation code based on MOL solution of DOM with Grey Gas model developed by Selçuk and her coworkers [114] is used. Further details of the code can be found in [115]. The ODE solver utilized is ROWMAP which is based on the ROW-methods of order 4 and uses Krylov techniques for the solution of linear systems. The computational parameters related to the ODE solver subroutine are summarized in Appendix F.

All simulations are carried out on a computer with Intel® Core™ 5i CPU 4200 1.60 GHz processor having 4.00 GB of RAM. CPU times are recorded for an error tolerance of 0.001 throughout the analyses.

5.1. Angular and Spatial Discretization Refinement

The accuracy of the MOL solution of DOM depends on the accuracy of both the angular and spatial discretization. For discretization study, radiative properties of particle laden combustion gases are calculated by using Grey Gas (GG) model for the gas and geometric optics approximation (GOA) for the fly ash particles due to its computational efficiency. Henyey-Greenstein (HG) phase function with normalization [107] is used for anisotropic scattering of radiation by the particles. Anisotropic scattering phase function has recently been shown to be more sensitive to the angular discretization than isotropic scattering phase function in terms of source term predictions [28]. Therefore, implementation of anisotropic scattering phase function necessitates re-evaluation of the previously determined angular (S_4) and spatial ($5 \times 5 \times 35$ grids in x, y and z directions, respectively) resolution for grid independent solution in the case of isotropically scattering particles [48]. Angular and spatial grid refinement study is performed only on test case 2 where particle loading is one order of magnitude higher than test case 1 as finer angular and spatial discretizations are required for higher particle loading in RTE solution.

For the angular discretization, different orders ($N = 4, 6, 8, 10, 12$) of approximation of DOM are studied to evaluate the predictive accuracy of order of S_N method by comparing its predictions against the highest order, $N=12$. For the numerical solution, $5 \times 5 \times 35$ spatial grid resolution [48] is selected. For the difference relations of spatial derivatives, three point upwind differencing scheme (DSS014), assessed previously for accuracy [22, 87, 117, 118], is deployed.

Figure 5.1 shows predicted incident heat fluxes along the centerline of the side wall and source term along the centerline of the freeboard for test case 2. As can be seen from the figure, incident wall heat fluxes are not affected by the angular discretization whereas the source term predictions are sensitive to angular discretization.

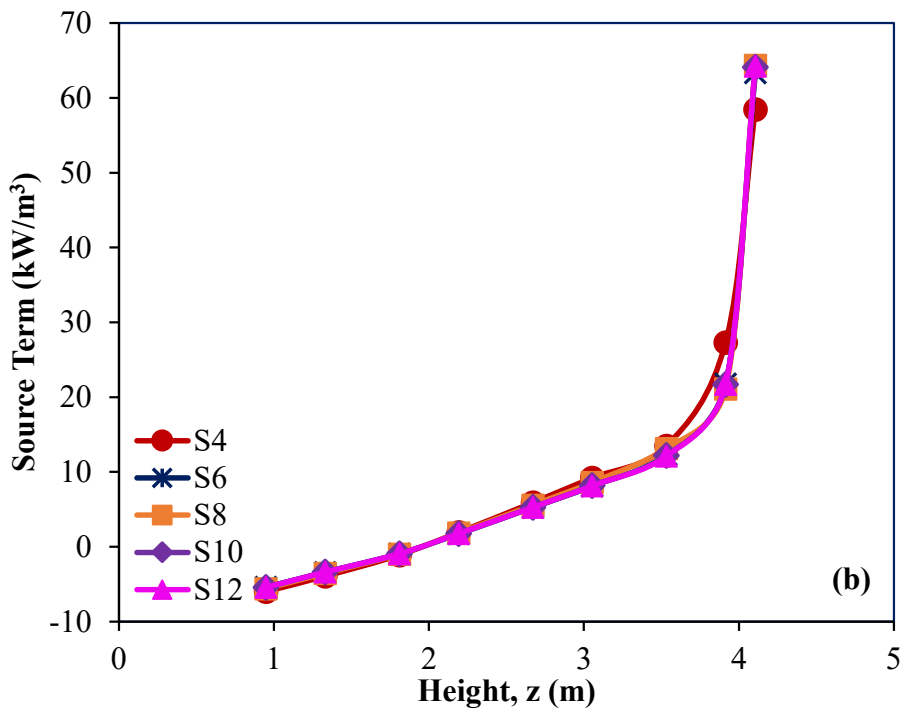
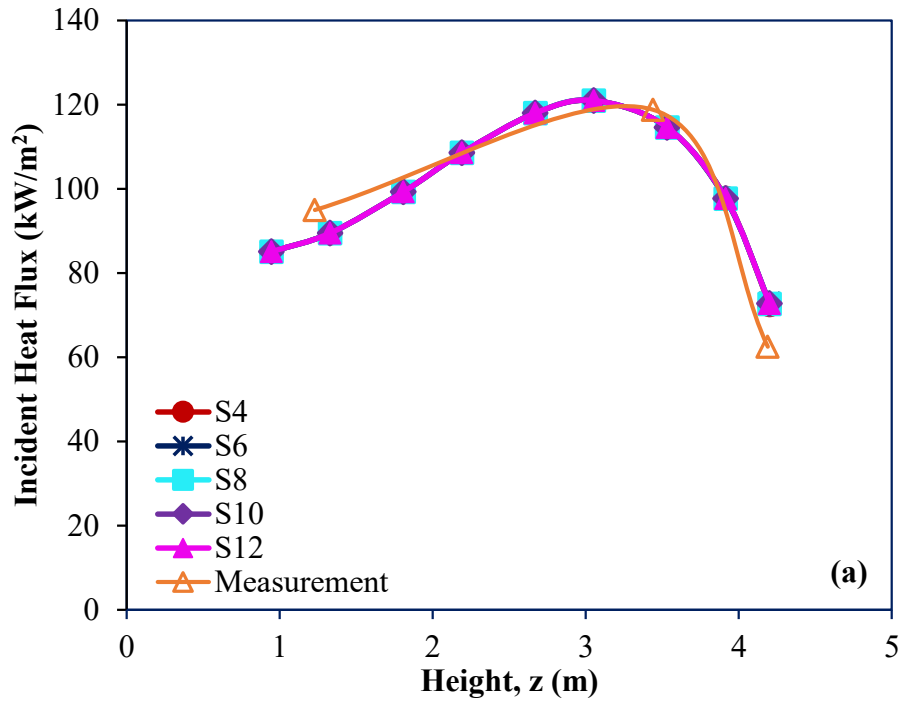


Figure 5.1 Effect of angular discretization on (a) incident wall heat flux and (b) source term predictions for test case 2

Table 5.1 illustrates relative errors for incident heat flux and source term predictions with corresponding CPU times. The use of lower order quadrature (S4) leads to

unrealistic source term predictions due to the ray effect (see section 2.2.1). Figure 5.2 shows average relative % error in source term predictions with respect to angular scheme refinement at spatial grid of 5x5x35. Increasing number of rays per quadrature is expected to improve accuracy of the predictions; however, oscillatory behaviour was observed in source term predictions as shown in Table 5.1 and Figure 5.2.

Table 5.1 Effect of angular discretization on predictive accuracy and CPU efficiency for test case 2 at spatial grid of 5x5x35

S_N	Average relative % error*		CPU time (s)
	Incident Heat Flux	Source Term	
S_4	0.0	12.3	2
S_6	0.0	-0.6	6
S_8	0.0	6.0	10
S_{10}	0.0	0.3	26
S_{12}	Reference solution		41

*Relative % Error = $[(\text{predicted} - \text{reference solution})/\text{reference solution}] \times 100$

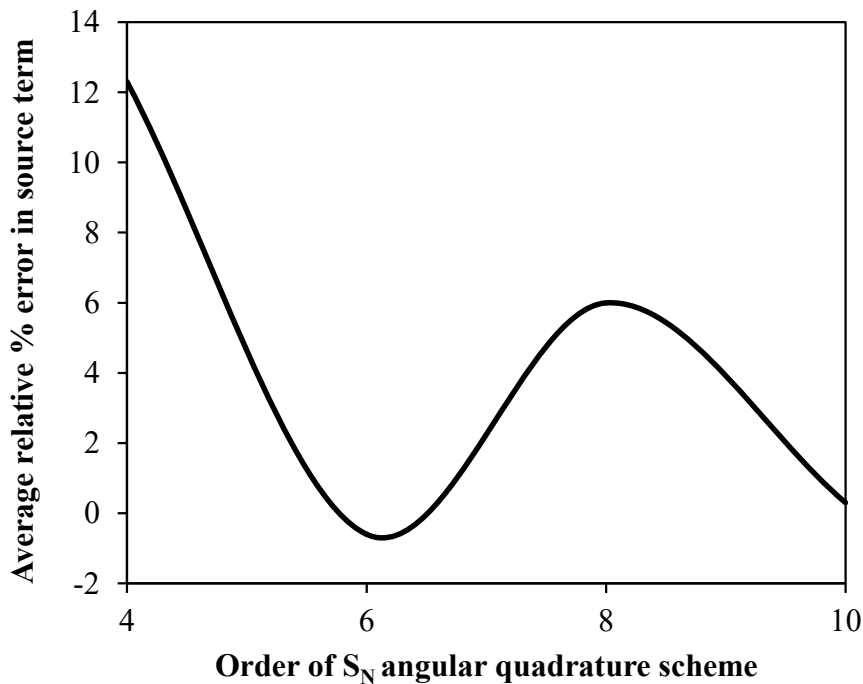


Figure 5.2 Comparison of average relative % error in source term predictions for test case 2 at spatial grid of 5x5x35

According to Equation 2.14, accuracy of solution is directly proportional to the ratio of spatial grid size to direction cosine magnitude. As higher order S_N quadrature necessitates finer spatial grid to achieve a converged solution, spatial grid resolution is increased and finer spatial grids ($7 \times 7 \times 53$, $9 \times 9 \times 67$, $11 \times 11 \times 81$, $13 \times 13 \times 96$ and $15 \times 15 \times 110$ grids in x, y and z directions, respectively) are tested. Angular quadrature scheme is chosen as S_{10} to study spatial grid independency. It should be highlighted that solutions were provided with three point upwind differencing scheme so far in the study. However, it is observed that the solution does not converge at finer grid resolution with three point upwind differencing scheme. A previous work on effect of spatial differencing schemes on the performance of MOL solution of DOM in anisotropically scattering medium shows that increasing the number of spatial grids enables utilization of lower order finite differencing scheme at the expense of CPU time [26]. In the light of this information, two point upwind differencing scheme (DSS012) is implemented from now on to alleviate convergence problem at finer grid resolutions. Incident wall heat fluxes and source terms are illustrated in Figure 5.3. It is found that coarser grids do not affect the incident heat fluxes along the side wall while they lead to over prediction of the source term along the centerline of the freeboard.

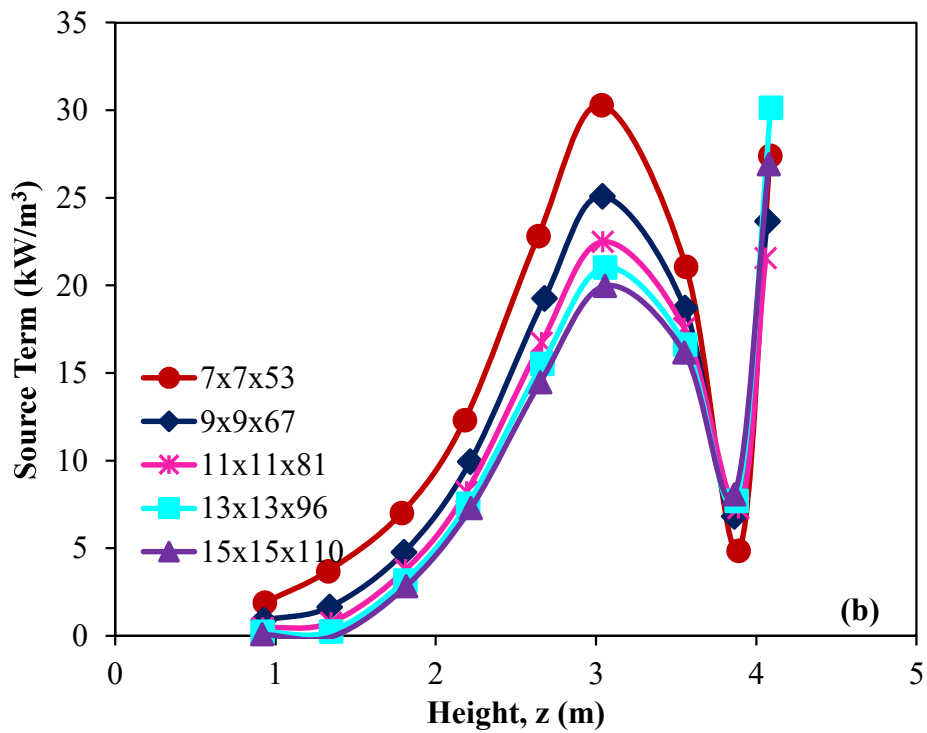
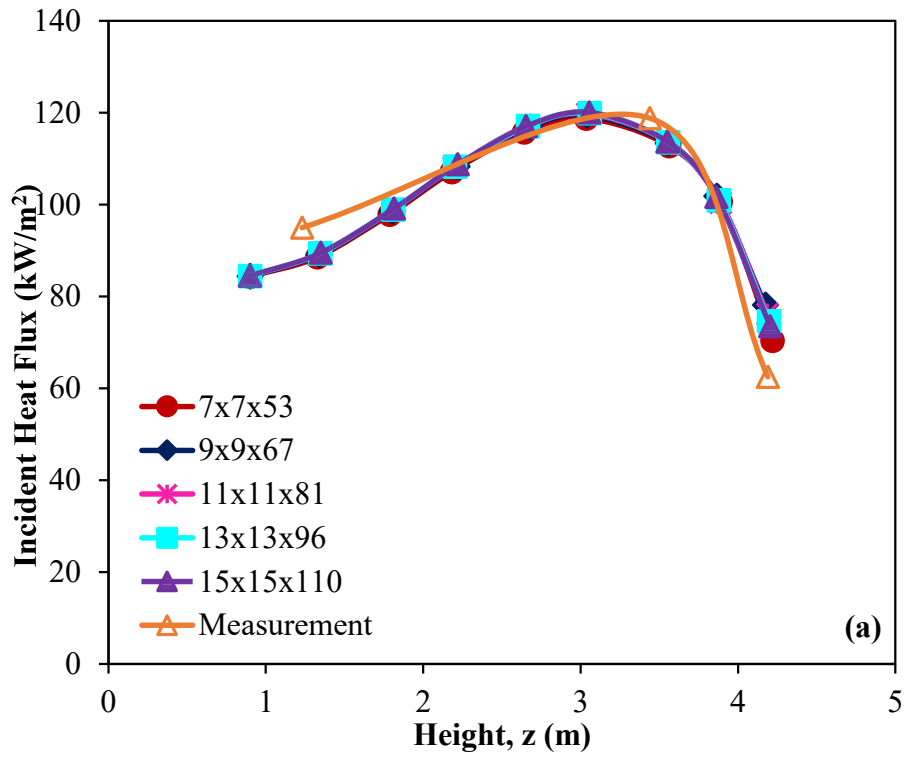


Figure 5.3 Effect of spatial discretization on (a) incident wall heat flux and (b) source term predictions for test case 2

Relative errors for the incident wall heat fluxes and source terms with corresponding CPU times are tabulated in Table 5.2.

Table 5.2 Effect of spatial discretization on predictive accuracy and CPU efficiency for test case 2

Number of control volumes	Average relative % error*		CPU time (s)
	Incident heat flux	Source term	
7×7×53	-0.9	61.1	42
9×9×67	-0.5	26.8	218
11×11×81	-0.3	14.8	230
13×13×96	-0.1	5.8	323
15×15×110	Reference solution		907

*Relative % Error = [(predicted – reference solution) / reference solution] ×100

As can be seen from the table, errors decrease with increasing number of grids at the expense of computational time. Therefore, from the viewpoints of accuracy and computational economy, the use of 13×13×96 control volumes is found to be sufficient for the system under consideration. Based on this fine grid resolution (13×13×96), angular discretization schemes (N = 4, 6, 8, 10, 12) are re-evaluated in order to find out whether the oscillation problem is alleviated or not. Calculated incident wall heat fluxes and source terms are illustrated in Figure 5.4. Incident wall heat fluxes are found to be not affected by angular discretization whereas the source term predictions are sensitive to angular discretization.

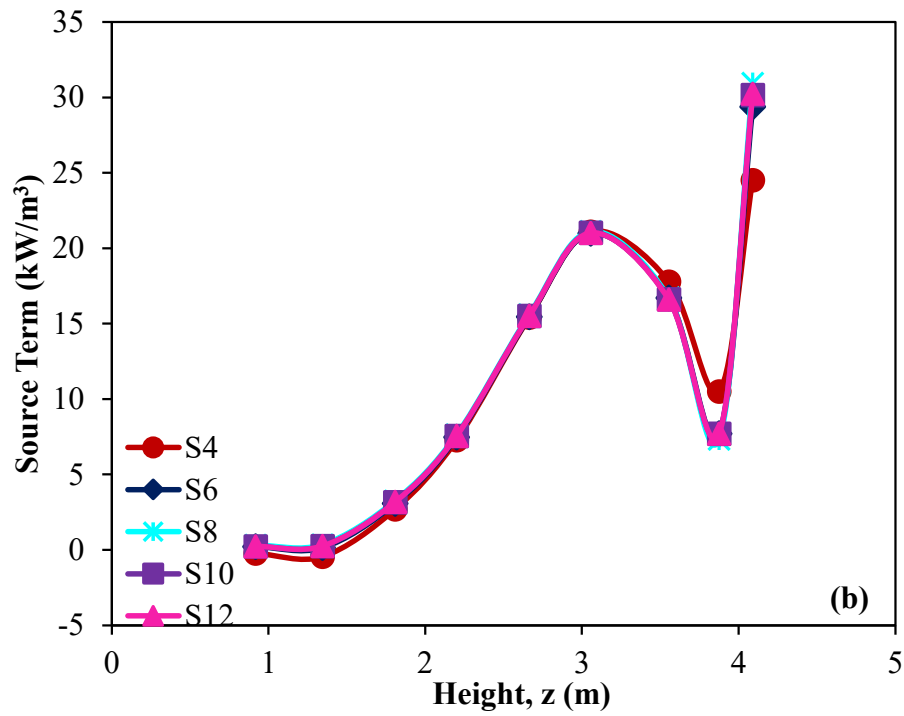
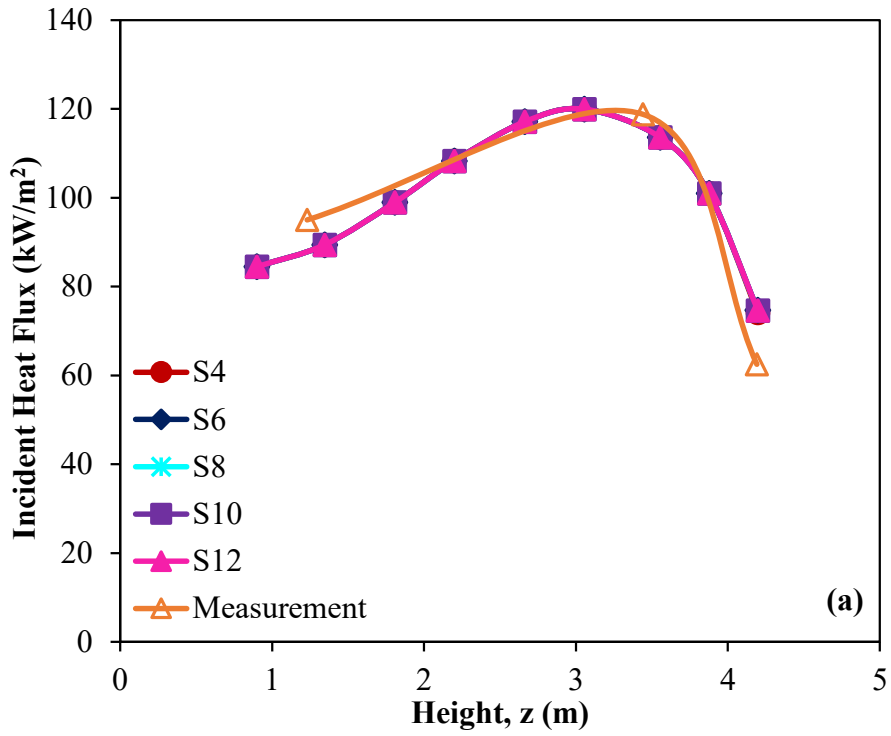


Figure 5.4 Effect of angular discretization on (a) incident wall heat flux and (b) source term predictions for test case 2

Relative errors for the incident heat flux and source term with corresponding CPU times are tabulated in Table 5.3. It is seen that the percentage errors with the fine

grid (13x13x96) is much smaller compared to that of coarse grid (5x5x35) and oscillatory behavior is eliminated (Figure 5.5). Hence, S_{10} provides satisfactory solutions in terms of both accuracy and computational efficiency and is utilized as the angular quadrature scheme in the rest of the study.

Table 5.3 Effect of angular discretization on predictive accuracy and CPU efficiency for test case 2 at spatial grid of 13x13x96

S_N	Average relative % error*		CPU time (s)
	Incident heat flux	Source term	
S_4	0.0	-1.9	67
S_6	0.0	-0.8	88
S_8	0.0	0.8	268
S_{10}	0.0	0.0	323
S_{12}	Reference solution		972

*Relative % Error = [(predicted - reference solution) / reference solution] \times 100

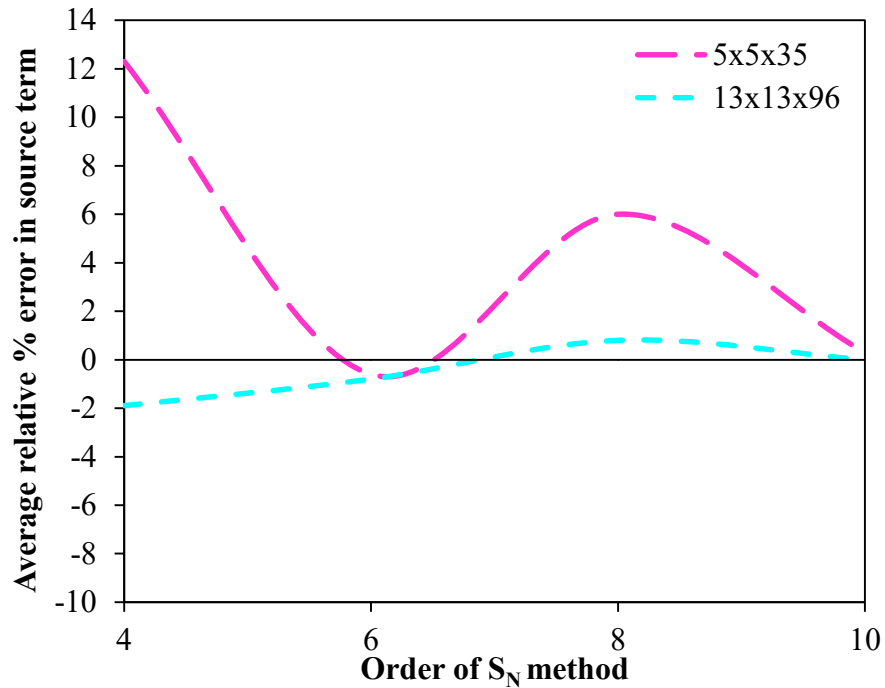


Figure 5.5 Comparison of average relative % error in source term predictions for test case 2 at different spatial grids

Therefore, from the viewpoints of accuracy and computational economy, the use of two point upwind differencing scheme (DSS012) with $13 \times 13 \times 96$ control volumes and S_{10} approximation is utilized throughout the study.

5.2. Validation of the Model against Experimental Data

Measurements used for benchmarking predictions of the radiation model have previously been carried out on the 0.3 MW_t ABFBC Test Rig of Chemical Engineering Department of METU. Furthermore, accuracy and CPU efficiency of GOA (GOA3) are also assessed for different optical thicknesses ($\tau_1 = 0.75$, $\tau_2 = 4.33$) involved in the bubbling fluidized bed combustion test cases under consideration as GOA3 has previously been shown to provide acceptable accuracy with minimum CPU time under CFBC conditions [42]. While assessing the accuracy and CPU efficiency of GOA, Mie solution is used for benchmarking and anisotropic scattering of radiation by the particles is taken into consideration.

Figure 5.6 illustrates comparison between incident radiative heat fluxes predicted by the radiation model coupled with absorbing, emitting grey gases (GG) and absorbing, emitting and anisotropically scattering grey particles (Mie / GOA) and measurements for both test cases. As can be seen from the figure, GOA predictions are in excellent agreement with those of Mie theory, which agree well with the measurements.

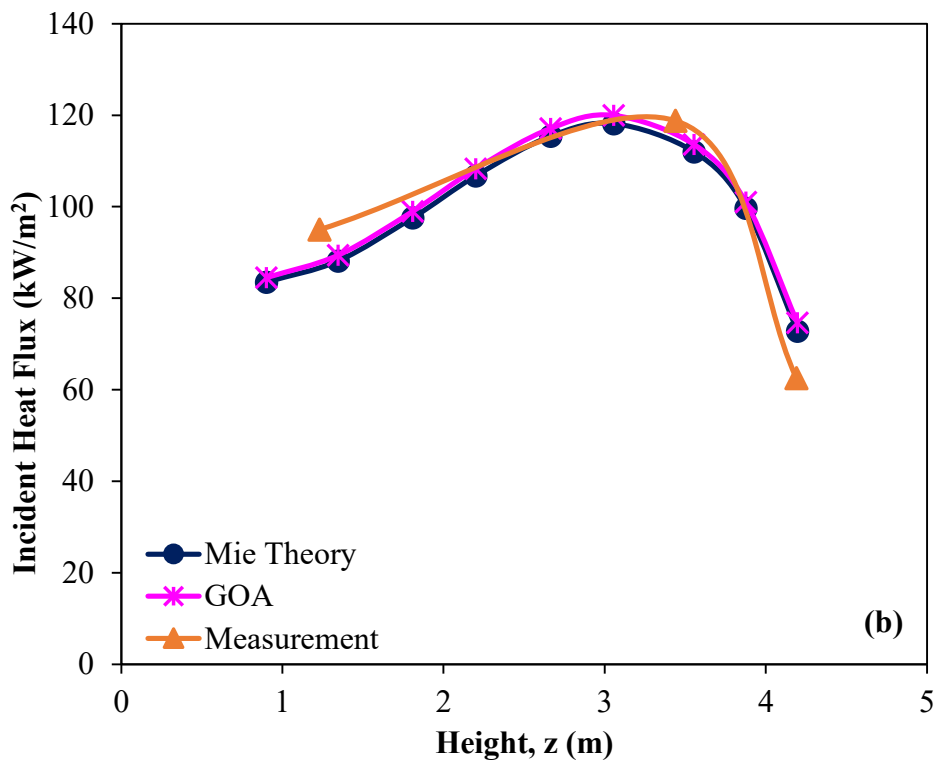
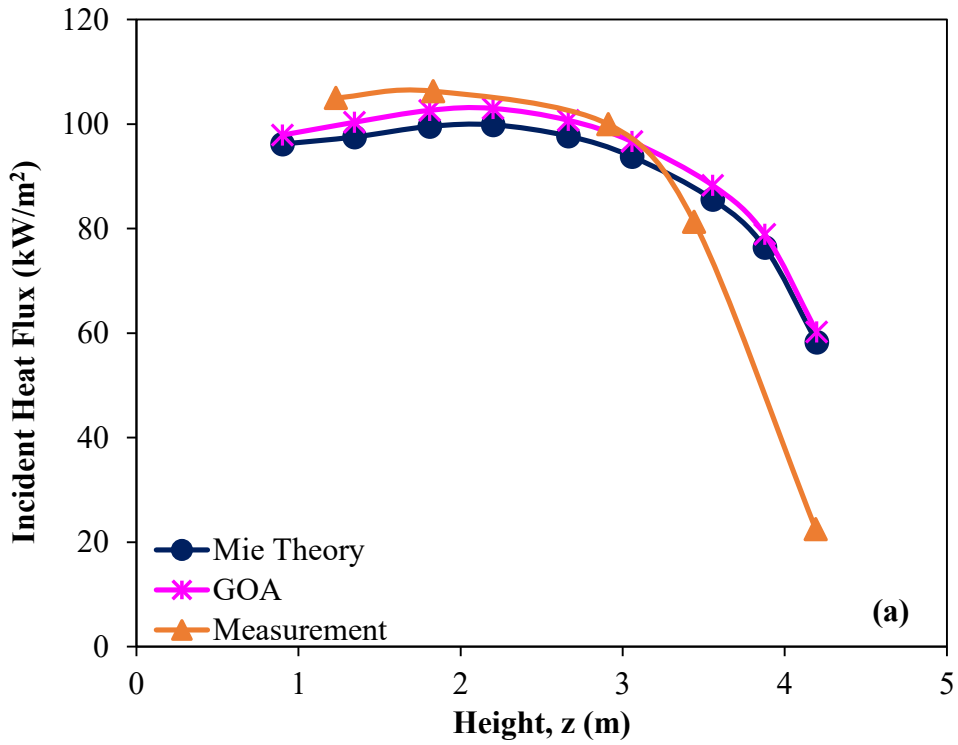


Figure 5.6 Measured and predicted incident radiative heat fluxes for (a) test case 1 and (b) test case 2

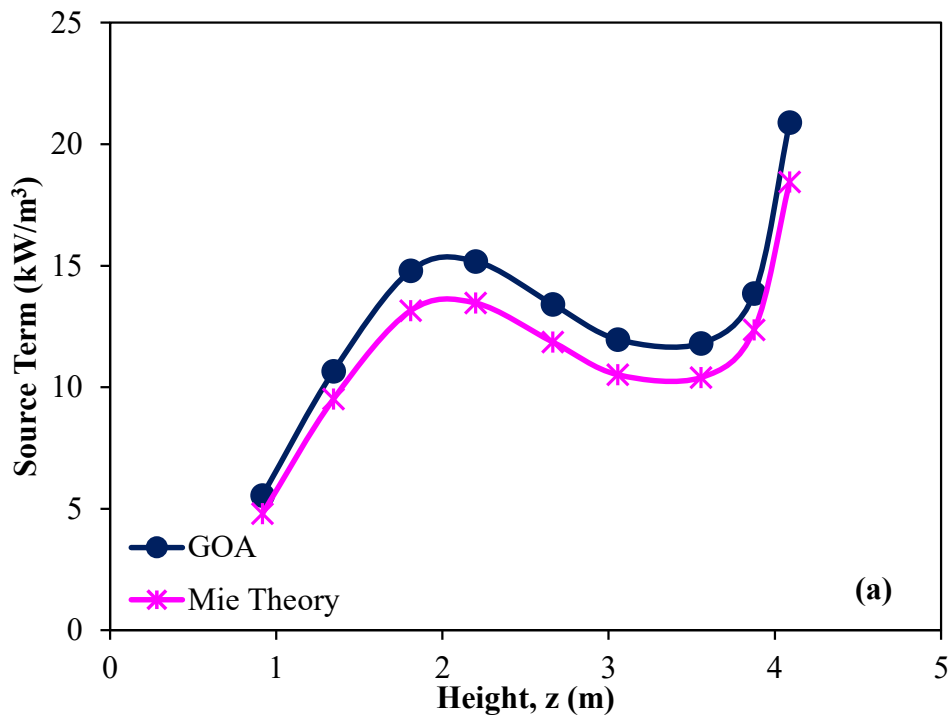
For comparative testing purposes, point values of the predicted fluxes are compared with the measurements at discrete points. Table 5.4 shows the relative percentage errors in incident wall heat fluxes predicted by utilizing Mie theory and GOA and measurements. As can be seen from the table, predictions are in good agreement with measurements and percentage errors are of the same order of magnitude for both test cases. The increase in freeboard temperature of the test case with recycle of fine particles is considered to lead to 46 % increase in the heat flux of test case 2 at 3.44 m height. The reason behind the increase in temperature from test case 1 ($T_m=1137$ K) to test case 2 with recycle ($T_m=1202$ K) is one order of magnitude increase in particle load, from 0.011 to 0.131 at this elevation. Large discrepancy between the predictions and the measurement at the uppermost port for test case 1 is considered to be due to lower particle load ($B_1=0.011$) and location of the radiometer probe very close to cooling tubes, which affects the radiative intensity measurement at this port. Smaller discrepancy in test case 2, however, is considered to be due to increased radiative emissions from higher particle load, which compensates the effect of cooling tubes.

Table 5.4 Incident radiative heat fluxes on freeboard side walls for test case 1 and test case 2

Height (m)	Measurements (kW/m ²)	Predictions (kW/m ²)		Relative % Error*	
		GOA	Mie Theory	GOA	Mie Theory
Test case 1 (w/o recycle)					
1.23	105.0	99.7	99.4	-5.0	-5.3
1.83	106.3	102.8	102.3	-3.3	-3.8
2.91	100.0	98.4	98.0	-1.6	-2.0
3.44	81.3	90.6	90.2	11.4	10.9
4.19	22.5	59.7	59.7	165.4	165.3
Test case 2 (with recycle)					
1.23	95.0	87.8	87.7	-7.6	-7.6
3.44	118.8	116.8	116.0	-2.3	-2.4
4.19	62.5	74.6	73.9	19.4	18.3

* Relative % Error = [(predicted - measured) / measured] × 100

Despite the fact that there is excellent agreement between the wall fluxes predicted by GOA and Mie theory under consideration, it was also considered necessary to investigate the source term predictions to be used in the solution of energy conservation equation in CFD codes. Figure 5.7 illustrates the comparison between the source term distributions predicted by GOA and Mie theory along the centerline of the freeboard for both test cases. As can be seen from the figure, GOA leads to over-prediction of the source term especially for test case 1. It is worth noting that the source term profiles predicted by both models are found to follow similar trend for both test cases, as physically expected. Local differences in predicted source terms between two test cases, however, is due to the differences in gas and boundary temperatures.



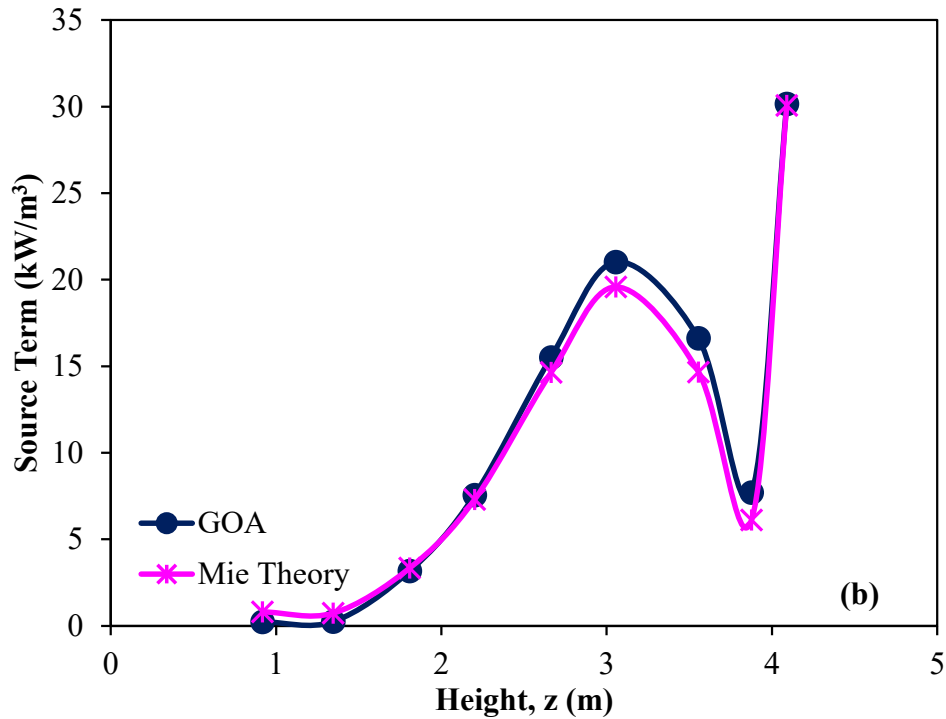


Figure 5.7 Effect of utilizing GOA as particle property model on radiative energy source term for (a) test case 1 and (b) test case 2

The performance of GOA with respect to Mie theory in terms of incident heat fluxes and source term predictions with corresponding CPU times are tabulated in Table 5.5. As can be seen from the table, error in utilizing GOA is large for test case 1 in terms of source term. For GOA to be applicable, size parameter of the particles are expected to be larger than 25 and as a matter of fact surface mean diameter (Sauter mean diameter) gives a size parameter of 23.4. Despite this agreement, utilizing GOA fails in source term predictions for test case 1. This poor performance is attributed to the presence of fine particles which dominate geometric cross sectional area distribution due to their high number densities. As can be seen in Figure 5.8, fine particles constitute 78 % of the cumulative cross sectional area despite their low weight fraction which is around 23 % (Figure 5.9). For test case 2 in which fine particles constitute a lower percentage (54 %) of the total cross sectional area, Mie and GOA predictions become closer to one another. Therefore, it is recommended to base applicability of GOA on cumulative cross sectional area distribution rather than surface mean diameter or cumulative weight percent distribution of particles if

PSD involves both fine and coarse particles. Moreover, GOA is found to increase CPU efficiency of solution for only test case 2 and no noticeable difference is observed between GOA and Mie solutions in test case 1. This is considered to be due to the fact that less number of iterations is sufficient for numerical convergence, leading to lower number of equations to be solved, owing to higher optical thickness of test case 2.

Table 5.5 Effect of GOA on incident heat fluxes and source terms for test case 1 and test case 2

	Test case 1			Test case 2		
	Relative % Error*			Relative % Error*		
	Incident Heat Flux	Source Term	CPU time (s)	Incident Heat Flux	Source Term	CPU time (s)
GOA	0.4	13.1	733	0.1	5.2	323
Mie Theory	Reference solution		720	Reference solution		527

* Relative % Error = [(prediction – reference solution) / reference solution] × 100

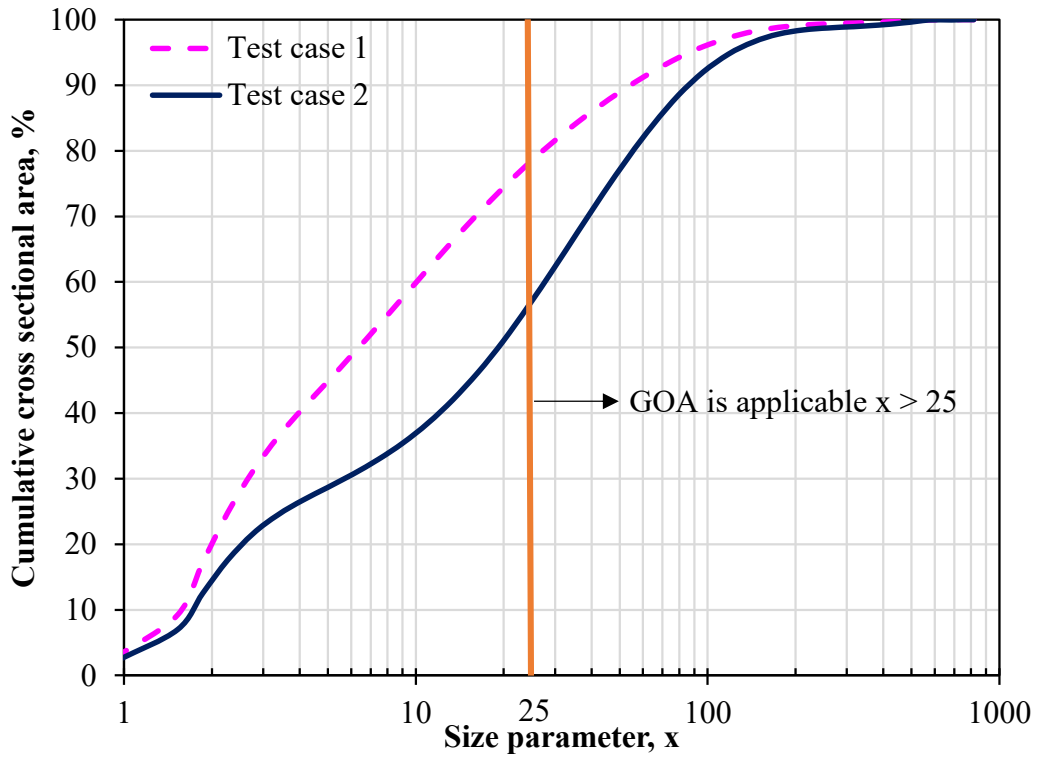


Figure 5.8 Applicability of GOA limit based on cumulative cross sectional area for test case 1 and test case 2

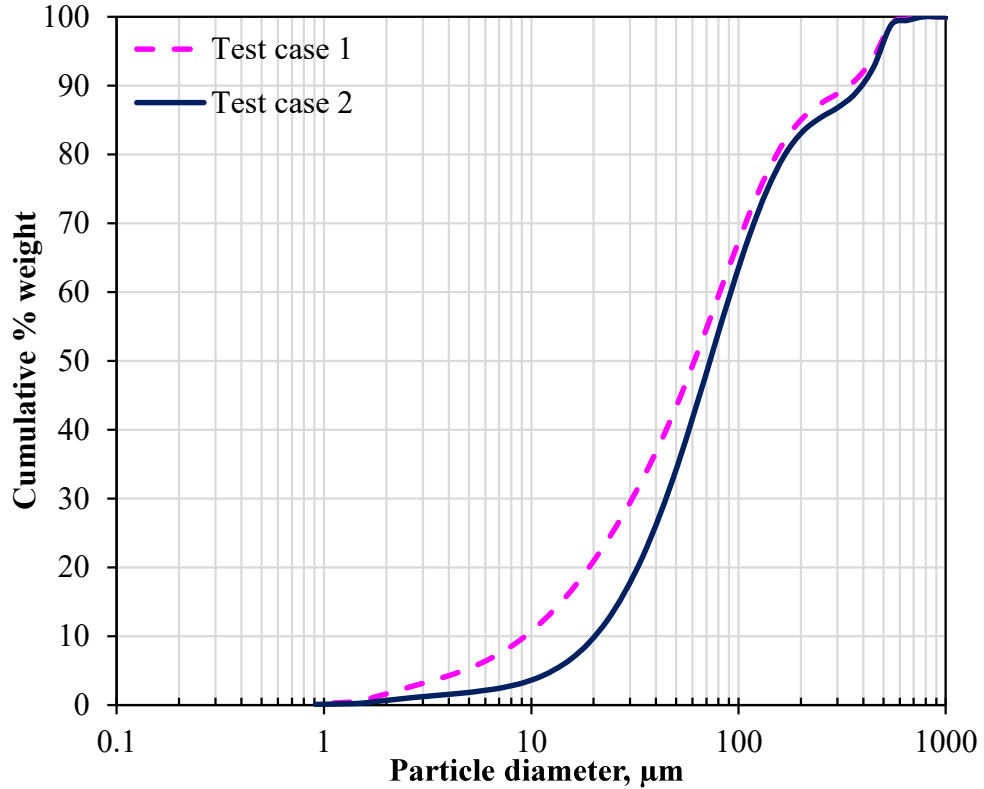
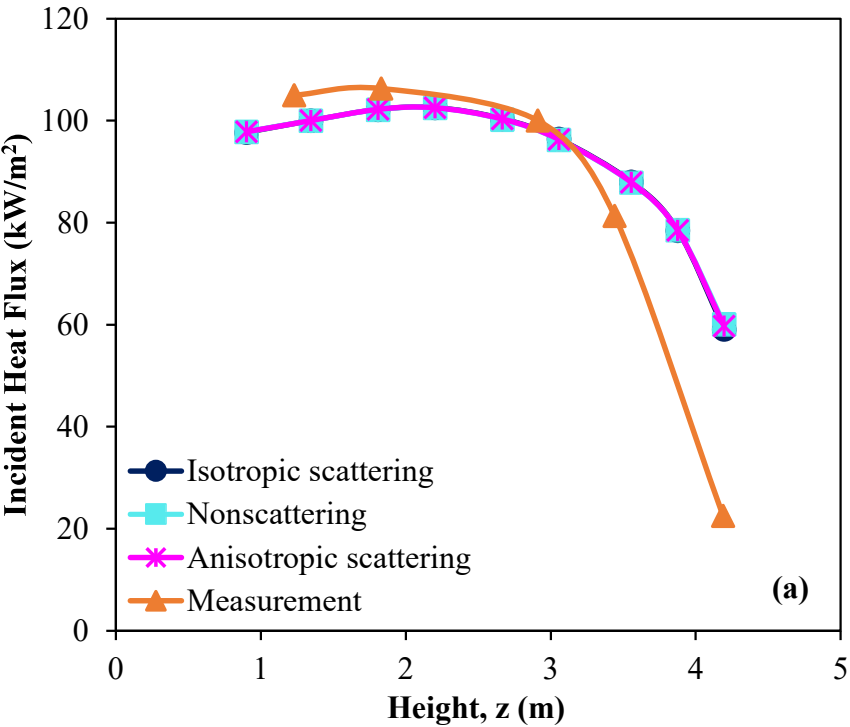


Figure 5.9 Cumulative particle size distribution for test case 1 and test case 2

5.3. Assessment of Accuracy of Scattering Phase Function Simplifications

It is well known that presence of highly forward scattering fly ash particles in high temperature combustion systems requires extensive computational effort when solution of RTE is coupled with the solution of conservation equations. Although Mie scattering is simplified by using approximate anisotropic phase function models (see Chapter 3), further simplifications, isotropic/non – scattering assumptions, can also be utilized to provide CPU efficient solutions. This is why it is considered necessary to investigate the predictive accuracy and computational efficiency of nonscattering and isotropic scattering cases by benchmarking their predictions against those of forward scattering represented by Henyey-Greenstein phase function with the normalization [107]. Particle properties implemented for this study is obtained from Mie theory since utilizing GOA leads to over-prediction of source term, especially for test case 1. Effect of scattering on predictions of incident heat

fluxes along the side walls and radiative energy source term along the centerline of the freeboard are shown in Figures 5.10 and 5.11, respectively. Incident heat flux distributions of nonscattering and isotropic scattering cases are found to be in good agreement with the forward scattering solution for both test cases. As seen in Figure 5.11, both simplifications give reasonable accuracy in source term predictions in optically thin media of test case 1 while discrepancy in the source term predictions due to phase function simplifications are found to increase as the optical thickness of the medium increases.



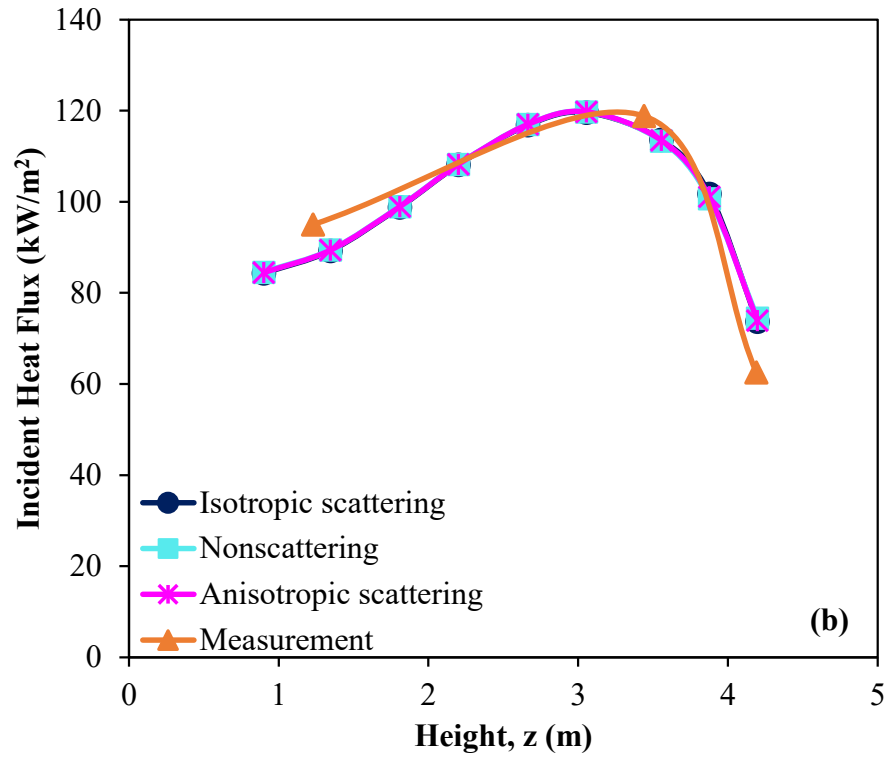


Figure 5.10 Effect of phase function simplifications on incident heat fluxes for (a) test case 1 and (b) test case 2

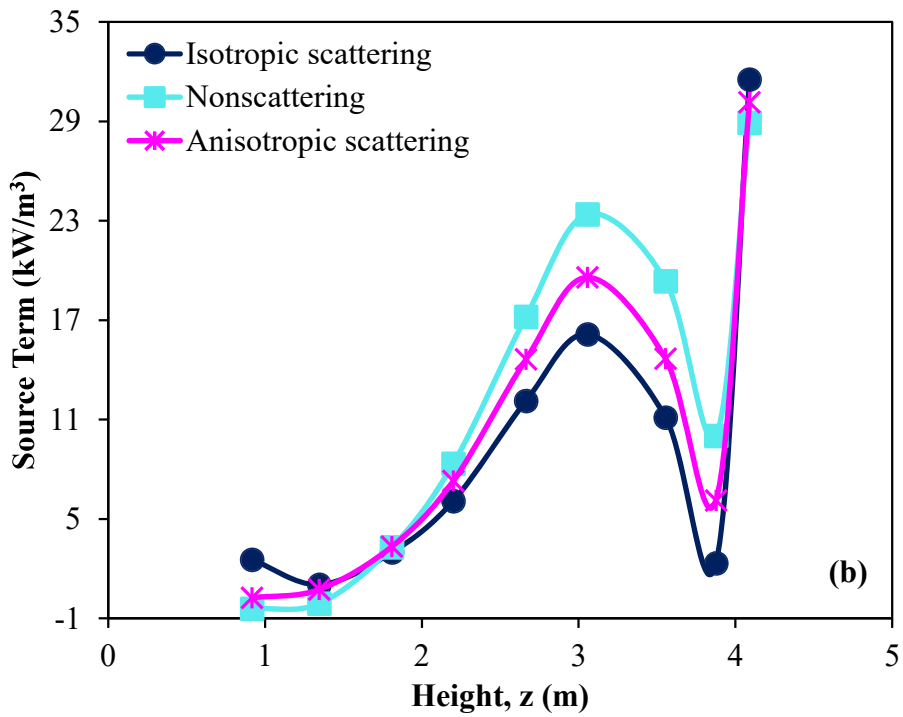
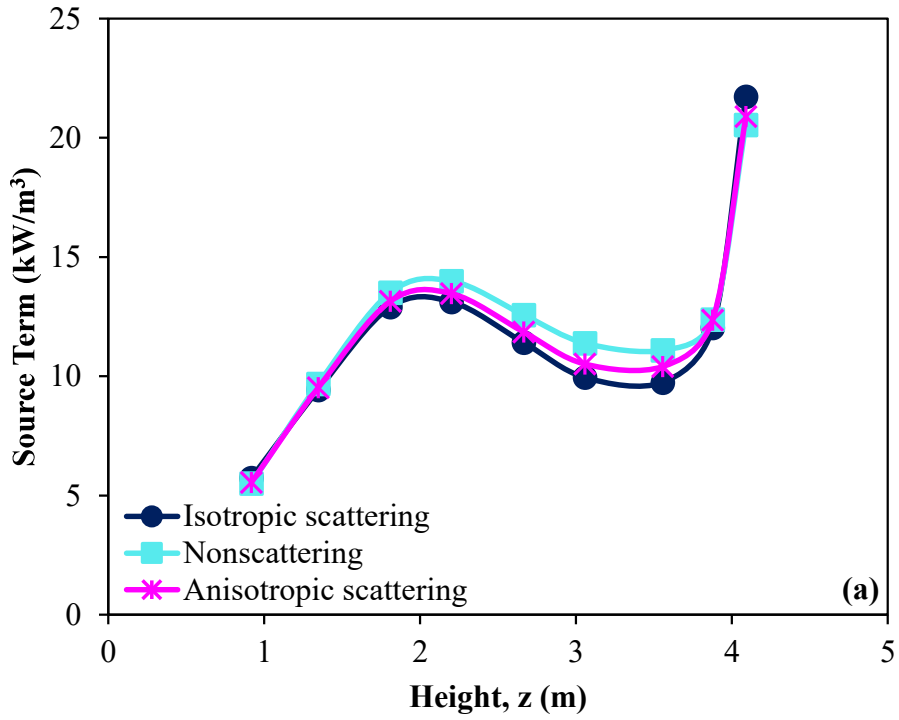


Figure 5.11 Effect of phase function simplifications on radiative source terms for (a) test case 1 and (b) test case 2

The percentage errors in the incident heat fluxes and source term predictions with corresponding CPU times are given in Table 5.6. It is seen from the table, an order

of magnitude higher particle loading observed in the case with recycle ($B_1 = 0.011$ and $B_2 = 0.131$) leads to an order of magnitude increase in average percent error in source term predictions. This behaviour is due to the fact that radiative properties of the particles are directly proportional to the particle loading. Therefore, as the particle loading increases, contribution of particles to radiative heat transfer increases accordingly, which necessitates representation of particle behaviour more accurately. Thus, any approximation to simplify scattering phase function results in inaccurate radiative heat transfer predictions as the optical thickness of the medium increases. Furthermore, one of the main reasons for phase function simplifications is to reduce computational effort in RTE solution. However, no improvement in CPU economy is observed in test case 1. Nevertheless, comparison between isotropic / nonscattering and forward scattering phase functions with regard to algorithm development and its implementation shows that isotropic / nonscattering assumptions require significantly less set-up time to program and hence can be implemented for optically thin media. Although CPU efficiency of scattering phase function simplifications is observed in test case 2, predictions are not sufficiently accurate as these simplifications do not represent the actual scattering behavior of the particles and this discrepancy becomes significant at higher particle load.

Table 5.6 Effect of phase function simplifications on incident heat fluxes and source terms for test case 1 and test case 2

	Phase function	Average Relative % Error*		CPU Time (s)
		Incident Heat Flux	Source Term	
Test case 1 ($\tau = 0.85$)	Nonscattering	-0.0	5.1	964
	Isotropic	0.1	-3.7	699
	Forward	Reference Solution		720
Test case 2 ($\tau = 4.77$)	Nonscattering	0.0	16.3	454
	Isotropic	-0.1	-16.9	405
	Forward	Reference Solution		527

* Relative % Error = [(approximation - reference solution)/reference solution] \times 100

CHAPTER 6

CONCLUSIONS

Predictive accuracy and CPU efficiency of geometric optics approximation (GOA) and scattering phase function simplifications in the freeboard of lignite-fired METU 0.3 MW_t ABFBC Test Rig were tested by applying them to the modeling of radiative heat transfer and comparing their predictions against measurements and benchmark solutions. The freeboard was treated as a 3-D rectangular enclosure containing grey, absorbing, emitting gas with grey, absorbing, emitting, non/isotropically/anisotropically scattering particles surrounded by diffuse grey/black walls. Incident heat fluxes along the side walls and source terms along the centerline of the freeboard were predicted by the MOL solution of DOM with Leckner's correlations for gas, Mie theory / GOA for particles and normalized Henyey-Greenstein for the phase function. The input data required for the model and its validation were provided from the experimental data, which was previously taken from METU 0.3 MW_t ABFBC Test Rig operating with and without recycle of fine particles.

Firstly, effect of spatial and angular discretizations on the accuracy and computational economy of the model predictions was investigated by utilizing different number of spatial grids ($7 \times 7 \times 53$, $9 \times 9 \times 67$, $11 \times 11 \times 81$, $13 \times 13 \times 96$ and $15 \times 15 \times 110$ grids in x, y and z directions, respectively) and different orders (N = 4, 6, 8, 10, 12) of approximation of DOM and comparing their predictions with those obtained with the finest spatial/angular discretization on the test case with recycle of fine particles. In order to provide grid independent solutions, radiative properties of the particle laden combustion gases were estimated by using Leckner's correlations for gas and GOA for particles. Henyey-Greenstein phase function with

normalization was used for anisotropic scattering of radiation by the particles. Comparisons revealed that source term predictions are more sensitive to spatial and angular discretizations compared to those of incident heat fluxes. As a result of this parametric study, the use of $13 \times 13 \times 96$ control volumes with S_{10} angular quadrature scheme was selected for the system under consideration.

Having validated the incident heat flux predictions of the model with anisotropic scattering against experimental data, predictive accuracy and computational efficiency of GOA were then assessed by benchmarking its source term predictions against those of Mie theory for different optical thicknesses involved in the bubbling fluidized bed combustion test cases under consideration and following conclusions have been reached.

- Applicability of GOA should be based on cumulative cross sectional area distribution rather than surface mean diameter or cumulative weight percent distribution of particles if PSD involves both fine and coarse particles.
- If the majority of cumulative cross sectional area is constituted by large particles which fall into geometric optics limit, GOA can yield satisfactory results.
- GOA improves CPU efficiency of the solution as the optical thickness of the medium increases.

Finally, predictive accuracy and computational economy of nonscattering and isotropic scattering were tested by comparing their predictions with those of anisotropic scattering represented by Henyey-Greenstein phase function. Conclusions drawn from the effect of phase function simplifications on incident heat fluxes and source terms are as follows:

- Phase function simplifications have insignificant effect on incident heat fluxes.
- Source terms are found to be sensitive to phase function simplifications regardless of the optical thickness of the medium and the sensitivity of phase function simplifications increases with increasing optical thickness. Error in source term predictions due to phase function simplifications leads to acceptable accuracy for optically thin medium while the error becomes significant as the optical thickness of the medium increases.

- Source term predictions of forward scattering lie between those of nonscattering and isotropic scattering.
- Accurate representation of particle scattering that is forward scattering is vital in combusting systems involving high particle loads.
- Isotropic / non – scattering assumptions have an insignificant effect on CPU economy for optically thin medium whereas phase function simplifications reduce CPU requirement as the optical thickness of the medium increases.

6.1. Suggestions for Future Work

Based on the experience gained in this study, the following recommendations for future extension of the work are suggested:

- Modification of the radiation code for the incorporation of particle load profile along the freeboard region is necessary since the radiative properties of particles depend on particle load.
- The accuracy of the model predictions can be improved by using spectral radiative properties for particles.

REFERENCES

- [1] 2015 Coal (Lignite) Sectoral Report (May 2016). Retrieved June 16, 2017, from <http://www.tki.gov.tr/depo/2017/KomurSektorRaporu2015.pdf>
- [2] Selçuk, N., and Kirmizigul, U., “Characteristics of a Fluidized Bed Combustor Burning Low-Quality Lignite”, *Journal of the Energy Institute*, vol. 64, pp. 151-156, 1991.
- [3] Selçuk, N., and Tezgorucu, O., “Combustion Characteristics of Low Quality Turkish Lignites In Fluidized Bed Combustors”, *Proceedings of 7th International Conference on Fluidization*, New York, pp. 505-513, 1992.
- [4] Selçuk, N., Atamer, S., Eroglu, I., Onal, I., and Kirmizigül, U., “2 MW_t Lignite Fired Atmospheric Fluidized Bed Boiler: Fundamental Process Design Philosophy”, *Proceedings of the 12th International Conference on Fluidized Bed Combustion*, ASME, vol. 1, pp. 303-308, 1993.
- [5] Selçuk, N., “Fluidized Bed Combustion Technologies for Existing Thermal Power Plants”, Invited Paper, *Workshop on Possibilities of Refurbishing Fossil- Fired Power Stations taking into Account Environmental Requirements*, Turkish Electricity Authority, Ankara, pp. 241-254, 1993.
- [6] Oymak, O., Selçuk, N. and Önal, I., “Testing of a Mathematical Model for the Combustion of Lignites in an AFBC”, *Fuel*, vol. 72, pp. 261-266, 1993.
- [7] Selçuk, N., Oymak, O., and Barlas, D, “Investigation of Sulfation Characteristics of AFBC Ashes Using SEM-EDX Technique”, *Proceedings of the 13th International Conference on Fluidized Bed Combustion*, ASME, vol. 1, pp. 351-359, 1995.
- [8] Barlas, D., Oymak, O., and Selçuk, N., “Sulfur Capture Behavior of Lignite Ash and Sorbent in AFBC’s”, *Preprints of International Symposium on Coal-Fired Power Generation, The Environment and Public Acceptance*, Ministry of Energy and Natural Resources and Turkish Electricity Generation-Transmission Corporation, Ankara, pp. 259-276, 1995.
- [9] Kirmizigul, U., Barlas, D., and Selçuk, N., “METU 0.3 MW AFBC Test Rig”, *Preprints of International Symposium on Coal-Fired Power Generation, The Environment and Public Acceptance*, Ministry of Energy and Natural

Resources and Turkish Electricity Generation-Transmission Corporation, Ankara, pp. 257-295, 1995.

- [10] Selçuk, N., Degirmenci, E., and Oymak, O., “Evaluation of an Improved Code for Performance of AFBCs”, *Journal of the Energy Institute*, vol. 70, pp. 3150, 1997.
- [11] Selçuk, N., Degirmenci, E., and Oymak, O., “Simulation of 0.3 MW_t AFBC Test Rig Burning Turkish Lignites”, *Proceedings of the 14th International Conference on Fluidized Bed Combustion*, ASME, vol. 2, pp. 1163-1174, 1997.
- [12] Degirmenci, E., and Selçuk, N., “Dynamic Behavior of an AFBC Test Rig: An Experimental Study”, *Proceedings of 15th International Conference on Fluidized Bed Combustion*, May 16-19, Savannah, GA, ASME, Paper No. FBC99-0100 (in CD-ROM), 1999.
- [13] Organ, L., and Selçuk, N., “Transient Sulfation Behavior Limestone Particles in an AFBC Test Rig: Data for Validation Studies”, *Proceedings of 15th International Conference on Fluidized Bed Combustion*, May 16-19, Savannah, GA, (Ed. R.B. Reuther), ASME, Paper No. FBC99-0101 (in CD-ROM), 1999.
- [14] Degirmenci, E., Gogebakan, Y., and Selçuk, N., “Assessment of Catalyst Deactivation Model for Sulfur Retention in Fluidized Bed Combustors”, *Combustion Science and Technology Journal*, vol. 153, pp. 95-111, 2000.
- [15] Selçuk, N., Degirmenci, E., and Gogebakan, Y., “Modeling of a Bubbling AFBC with Volatiles Release”, *Proceedings of 16th International Conference on Fluidized Bed Combustion*, May 13-16, Reno, Nevada, USA, ASME, Paper No. FBC01-0134, (in CD-ROM), 2001.
- [16] Selçuk, N., and Degirmenci, E., “Dynamic Simulation of Fluidized Bed Combustors and its Validation against Measurements”, *Combustion Science and Technology*, vol. 167, pp. 1-27, 2001.
- [17] Lindsay, J.J., Morton, W., and Newey, D.C., “Radiative Heat Transfer in the Freeboard of a fluidized Bed”, *Proceedings of the Fifth Engineering Foundation Conference on Fluidization*, Engineering Foundation, New York, N.Y., pp. 385-392, 1986.
- [18] Andersson, B.-A., Johnsson, F., and Leckner, B., “Heat Flow Measurements in Fluidized Bed Boilers”, *The 9th Int. Conf. on Fluidized Bed Combustion*, ASME Book No 10232, 1, New York, pp. 592-598, 1987.
- [19] Filla, M., and Scalabrin, A., “Influence of Scattering of Thermal Radiation by Suspended Particles on the Rate of Heat Transfer in the Freeboard of a 1 MW_t

Fluidized Bed Combustor”, *Proceedings of the Eurotherm Seminar: Heat Transfer Radiating and Combusting System-2*, pp. 37-49, 1994.

- [20] Kozan, M., and Selçuk, N., “Investigation of Radiative Heat Transfer in Freeboard of a 0.3 MW_t AFBC Test Rig”, *Combustion Science and Technology*, vol. 153, pp. 113-126, 2000.
- [21] Selçuk, N., Batu, A., and Ayrancı, I., “Performance of method of lines solution of discrete ordinates method in the freeboard of a bubbling fluidized bed combustor”, *Journal of Quantitative Spectroscopy & Radiative Transfer*, vol. 73, pp. 503-516, 2002.
- [22] Selçuk, N., and Kırbas, G., “The Method of Lines Solution of Discrete ordinates Method for Radiative Heat Transfer in Enclosures”, *Numerical Heat Transfer, Part B: Fundamentals: An International Journal of Computation and Methodology*, vol. 37:3, pp. 379-392, 2000.
- [23] Demirkaya, G., Arınç, F., Selçuk, N., and Ayrancı, I., “Comparison between performances of monte carlo method and method of lines solution of discrete ordinates method”, *Journal of Quantitative Spectroscopy & Radiative Transfer*, vol. 93, pp. 115-124, 2005.
- [24] Ayrancı, I., and Selçuk, N., “MOL solution of DOM for transient radiative transfer in 3-D scattering media”, *Journal of Quantitative Spectroscopy & Radiative Transfer*, vol. 84, pp. 409-422, 2004.
- [25] Selçuk, N., and Ayrancı, I., “The Method of Lines Solution of the Discrete Ordinates Method for Radiative Heat Transfer in Enclosures Containing Scattering Media”, *Numerical Heat Transfer, Part B: Fundamentals: An International Journal of Computation and Methodology*, vol. 43:2, pp. 179-201, 2003.
- [26] Ayrancı, I., and Selçuk, N., “Effect of spatial differencing schemes on the performance of MOL solution of DOM in anisotropically scattering medium”, *Proceedings of 12th Int. Heat Transfer Conference*, Grenoble, France, pp. 639-644, 2002.
- [27] Harmandar, S., and Selçuk, N., “The Method of Lines Solution of Discrete Ordinates Method for Radiative Heat Transfer in Cylindrical Enclosures”, *Journal of Quantitative Spectroscopy & Radiative Transfer*, vol. 84, pp. 395-407, 2004.
- [28] Ates, C., Ozen, G., Selçuk, N., and Kulah, G., “Radiative heat transfer in strongly forward scattering media of circulating fluidized bed combustors”, *Journal of Quantitative Spectroscopy & Radiative Transfer*, vol. 182, pp. 264-276, 2016.

- [29] Yin, C., “On gas and particle radiation in pulverized fuel combustion furnaces”, *Applied Energy*, vol. 157, pp. 554-561, 2015.
- [30] Crnomarkovic, N., Sijercic, M., Belosevic, S., Tucakovic, D., and Zivanovic, T., “Numerical investigation of processes in the lignite-fired furnace when simple gray gas and weighted sum of gray gases models are used”, *Int. J. Heat Mass Transfer*, vol. 56, pp. 197–205, 2013.
- [31] Andersson, K., Johansson, R., Hjærtstam, S., Johnsson, F., and Leckner, B., “Radiation intensity of lignite-fired oxy-fuel flames”, *Experimental Thermal and Fluid Sciences*, vol. 33, pp. 67–76, 2008.
- [32] Yin, C., “Effects of moisture release and radiation properties in pulverized fuel combustion: A CFD modeling study”, *Fuel*, vol. 165, pp. 252–259, 2016.
- [33] Zhang, J., Ito, T., Ito, S., Riechelmann, D., and Fujimori, T., “Numerical investigation of oxy-coal combustion in a large-scale furnace: Non-gray effect of gas and role of particle radiation”, *Fuel*, vol. 139, pp. 87–93, 2015.
- [34] Hjærtstam, S., Johansson, R., Andersson, K., and Johnsson, F., “Computational Fluid Dynamics Modeling of Oxy-Fuel Flames: The Role of Soot and Gas Radiation”, *Energy Fuels*, vol. 26, pp. 2786–2797, 2012.
- [35] Modest, M. F., *Radiative Heat Transfer*, Third edition, Academic Press, New York, 2013.
- [36] Butler, B. W., Denison, M. K., and Webb, B. W., “Radiation Heat Transfer in a Laboratory-Scale, Pulverized Coal-Fired Reactor”, *Experimental Thermal and Fluid Sciences*, vol. 9, pp. 69-79, 1994.
- [37] Viskanta, R., and Mengüç, M. P., “Radiation Heat Transfer in Combustion Systems”, *Progress in Energy and Combustion Science*, vol. 13, pp. 97-160, 1987.
- [38] Ruan, L.M., Tan, H.P. and Yan, Y.Y., “A Monte Carlo (MC) Method Applied to the Medium with Nongray Absorbing-Emitting-Anisotropic Scattering Particles and Gray Approximation”, *Numerical Heat Transfer, Part A: Applications*, vol. 42, pp. 253– 268, 2002.
- [39] Wu, B., Roy, S.P., Zhao, X., and Modest, M.F., “Effect of multiphase radiation on coal combustion in a pulverized coal jet flame”, *Journal of Quantitative Spectroscopy & Radiative Transfer*, vol. 197, pp. 154-165, 2017.
- [40] Buckius, R. W., and Hwang, D. C., “Radiation Properties for Polydispersions: Application to Coal”, *Journal of Heat Transfer*, vol. 102, pp. 99-103, 1980.

- [41] Johansson, R., Gronarz, T., and Kneer, R., “Influence of Index of Refraction and Particle Size Distribution on Radiative Heat Transfer in a Pulverized Coal Combustion Furnace”, *Journal of Heat Transfer*, vol. 139(4), 042702, 2017.
- [42] Ates, C., Selcuk, N., Ozen, G., and Kulah, G., “Benchmarking gray particle approximations against nongray particle radiation in circulating fluidized bed combustors”, *Numerical Heat Transfer, Part B: Fundamentals: An International Journal of Computation and Methodology*, vol. 71(5), pp. 467-484, 2017.
- [43] Kim, M. Y., “Assessment of the axisymmetric radiative heat transfer in a cylindrical enclosure with the finite volume method”, *International Journal of Heat and Mass Transfer*, vol. 51, pp. 5144-5153, 2008.
- [44] Doner, N., and Selçuk, N., “An application of Spectral line-based weighted sum of grey gases (SLW) model with geometric optics approximation for radiative heat transfer in 3-D participating media”, *Applied Thermal Engineering*, vol. 50, pp. 89-93, 2013.
- [45] Crnomarkovic, N., Sijercic, M., Belosevic, S., Tucakovic, D., and Zivanovic, T., “Radiative heat exchange inside the pulverized lignite fired furnace for the gray radiative properties with thermal equilibrium between phases”, *International Journal of Thermal Sciences*, vol. 85, pp. 21–28, 2014.
- [46] Zedtwitz, P., Lipinski, W., and Steinfeld, A., “Numerical and experimental study of gas-particle radiative heat exchange in a fluidized-bed reactor for steam-gasification of coal”, *Chemical Engineering Science*, vol. 62, pp. 599-607, 2007.
- [47] Adzerikho, K. S., Nogotov, E. F., and Trofimov, V. P., *Radiative Heat transfer in Two-Phase Media*, CRC Press, Boca Raton, 1993.
- [48] Ayranci, I., *The Method of Lines Solution of Discrete Ordinates Method for Radiative Heat Transfer in 3-D Rectangular Enclosures Containing Scattering Media*, M.Sc. Thesis, METU, Ankara, 2001.
- [49] Yuen, W. W. and Wong, L.W., “A Parametric Study of Radiative Transfer with Anisotropic Scattering in a One-Dimensional System”, *Journal of Quantitative Spectroscopy & Radiative Transfer*, vol. 22, pp. 231-238, 1979.
- [50] Mengüç, M.P., and Viskanta, R., “A Sensitivity Analysis for Radiative Heat transfer in a Pulverized Coal-Fired Furnace”, *Combustion Science and Technology*, vol. 51:1-3, pp. 51-74, 1987.
- [51] Marakis, J. G., Papapavlou, C., and Kakaras, E., “A parametric study of radiative heat transfer in pulverized coal furnaces”, *International Journal of Heat and Mass Transfer*, vol. 43, pp. 2961-2971, 2000.

- [52] Liu, F., and Swithenbank, J., “Modeling Radiative Heat Transfer in Pulverised Coal-Fired Furnaces”, *Heat Transfer in Radiating and Combusting Systems Volume 17 of the series EURO THERM Seminars*, pp. 358-373, 1991.
- [53] Selçuk, N., Ayranci, I., and Gogebakan, Y., “Effect of Recycle on Radiative Heat Transfer in the Freeboard of a Fluidized Bed Combustor”, *Proceedings of 18th International Conference on Fluidized Bed Combustion*, ASME, 2005.
- [54] Caliot, C., Eymet, V., Hafi, M.E., Maoult, Y.L., and Flamant, G., “Parametric study of radiative heat transfer in participating gas-solid flows”, *International Journal of Thermal Sciences*, vol. 47, pp. 1413-1421, 2008.
- [55] Johansson, R., Leckner, B., Andersson, K., and Johnsson, F., “Influence of particle and gas radiation in oxy-fuel combustion”, *International Journal of Heat and Mass Transfer*, vol. 65, pp. 143–152, 2013.
- [56] Bäckström, D., Gall, D., Pushp, M., Johansson, R., Andersson, K., and Pettersson, J.B.C., “Particle composition and size distribution in coal flames – The influence on radiative heat transfer”, *Experimental Thermal and Fluid Science*, vol. 64, pp. 70–80, 2015.
- [57] Bäckström, D., Johansson, R., Andersson, K., Wiinikka, H., and Fredriksson, C., “On the use of alternative fuels in rotary kiln burners — An experimental and modeling study of the effect on the radiative heat transfer conditions”, *Fuel Processing Technology*, vol. 138, pp. 210–220, 2015.
- [58] Ozen, G., and Selçuk, N., “Sensitivity of Radiation Modeling to Property Estimation Techniques in the Freeboard of Lignite-Fired Bubbling Fluidized Bed Combustors (BFBCs)”, *Combustion Science and Technology*, vol. 186, pp. 684–697, 2014.
- [59] Pallarés, J., Gil, A., Cortés, C., and Herce, C., “Numerical study of co-firing coal and *Cynara cardunculus* in a 350 MWe utility boiler”, *Fuel Processing Technology*, vol. 90, pp. 1207–1213, 2009.
- [60] Bhuiyan, A. A., and Naser, J., “CFD modeling of co-firing of biomass with coal under oxy-fuel combustion in a large scale power plant”, *Fuel*, vol. 159, pp. 150–168, 2015.
- [61] Kangwanpongpan, T., Silva, R. C., and Krautz, H. J., “Prediction of oxy-coal combustion through an optimized weighted sum of gray gases model”, *Energy*, vol. 41, pp. 244-251, 2012.
- [62] Hashimoto, N., and Watanabe, H., “Numerical analysis on effect of furnace scale on heat transfer mechanism of coal particles in pulverized coal combustion field”, *Fuel Processing Technology*, vol. 145, pp. 20–30, 2016.

- [63] Selçuk, N., Gogebakan, Y., Harmandar, H., and Altindag, H., “Effect of Recycle on Combustion and Emission Characteristics of High Sulfur Lignite”, *Combustion Science and Technology*, vol. 176:5-6, pp. 959-975, 2004.
- [64] Fiveland, W. A., “Discrete Ordinates Solutions of the Radiative Transport Equation for Rectangular Enclosures”, *Journal of Heat Transfer*, vol. 106, pp. 699-706, 1984.
- [65] Selçuk, N., and Kayakol, N., “Evaluation of Discrete Ordinates Method for Radiative Transfer in Rectangular Furnaces”, *International Journal of Heat and Mass Transfer*, vol. 40, pp. 213-222, 1997.
- [66] Truelove, J. S., “An Evaluation of the Discrete Ordinates Approximation for Radiative Transfer in an Absorbing, Emitting, and Scattering Planar Medium”, HTFS Report No.R8478, 1976.
- [67] Fiveland, W.A., “Discrete Ordinate Methods for Radiative Heat Transfer in Isotropically and Anisotropically Scattering Media”, *Journal of Heat Transfer*, vol. 109, pp. 809-812, 1987.
- [68] Kim, T., and Lee, H., “Effect of Anisotropic Scattering on Radiative Heat Transfer in Two-Dimensional Rectangular Enclosures”, *International Journal of Heat and Mass Transfer*, vol. 31, pp. 1711-1721, 1988.
- [69] Selçuk, N., and Kayakol, N., “Evaluation of Angular Quadrature and Spatial Differencing Schemes for Discrete Ordinates Method in Rectangular Furnaces”, *Proceedings of 31st National Heat Transfer Conference*, ASME HDT, vol. 325, pp. 151-158, 1996.
- [70] Selçuk, N., and Kayakol, N., “Evaluation of Discrete Transfer and Discrete Ordinates Methods for Radiative Heat Transfer in Rectangular Furnaces”, Invited Lecture, *Proceedings of International Symposium on Glass Problems*, ICG, vol. 1, pp. 255-276, 1996.
- [71] Kayakol, N., and Selçuk, N., “Effect of Angular Quadrature Schemes on the Predictive Accuracy of Discrete Ordinates Method for Radiative Transfer”, *CHMT 99, Proc .of International Conference on Computational Heat and Mass Transfer* (Ed. A. A. Mohamad and I. Sezai), Gazimağusa, Northern Cyprus, pp. 347-357, Eastern Mediterranean University Printing House, Gazimağusa, Northern Cyprus, 1999.
- [72] Kim, S. H., and Huh, K. Y., “Assessment of the Finite-Volume Method and the Discrete Ordinate Method for Radiative Heat Transfer in a Three-Dimensional Rectangular Enclosure”, *Numerical Heat Transfer, Part B: Fundamentals: An International Journal of Computation and Methodology*, vol. 35, pp. 85-112, 1999.

- [73] Ströhle, J., Knaus, H., Schnell, U., and Hein, K. R. G., “A Radiation Model for the Numerical Simulation of Coal-Fired Furnaces Using Body-Fitted Grids”, *Proceedings of Mediterranean Combustion Symposium* (Ed. F. Beretta), Antalya, Turkey, pp. 607-617, Tipolitografia Enzo Albano, Napoli, Italy, 1999.
- [74] Truelove, J. S., “Three-dimensional Radiation in Absorbing-Emitting-Scattering Media using the Discrete-Ordinates Approximation”, *Journal of Quantitative Spectroscopy & Radiative Transfer*, vol. 39, pp. 27-31, 1988.
- [75] Jamaluddin, A. S., and Smith, P. J., “Predicting Radiative Heat Transfer in Rectangular Enclosures using the Discrete Ordinates Method”, *Combustion Science and Technology*, vol. 59, pp. 321-340, 1988.
- [76] Fiveland, W. A., “Three-Dimensional Radiative Heat-Transfer Solutions by Discrete-Ordinates Method”, *Journal of Thermophysics and Heat Transfer*, vol. 2, pp. 309-316, 1988.
- [77] Hunter, B., and Guo, Z., “Numerical smearing, ray effect, and angular false scattering in radiation transfer calculation”, *International Journal of Heat and Mass Transfer*, vol. 81, pp. 63-74, 2015.
- [78] Coelho, P.J., “The role of ray effects and false scattering on the accuracy of standard and modified discrete ordinates method”, *Journal of Quantitative Spectroscopy & Radiative Transfer*, vol. 73, pp. 231-238, 2002.
- [79] Chai, J.C., HaeOk, S.L., and Patankar, S.V., “Ray Effect and False Scattering in the Discrete Ordinates Method”, *Numerical Heat Transfer, Part B: Fundamentals: An International Journal of Computation and Methodology*, vol. 24:4, pp. 373-389, 1993.
- [80] Karamehmetoğlu, S., *The Method of Lines Solution of Discrete Ordinates Method for Radiative Heat Transfer in Cylindrical Enclosures*, M.Sc. Thesis, METU, Ankara, 2002.
- [81] Carlson, B. G., and Lathrop, K.D., *Transport Theory-The Method of Discrete Ordinates in Computing Methods in Reactor Physics* (Edited by H. Greenspan, C. N. Kelber and D. Okrent), pp.165-266, Gordon & Breach, New York, 1968.
- [82] Fiveland, W. A., “The Selection of Discrete Ordinate Quadrature Sets for Anisotropic Scattering, Fundamentals of Radiation Heat Transfer”, *ASME HTD-vol. 160*, pp. 89-96, 1991.
- [83] Wakil, N. E., and Sacadura, J. F., “Some Improvements of Discrete Ordinates Method for the Solution of the Radiative Transport Equation in Multi-

- Dimensional Anisotropically Scattering Media”, *Developments in Radiative Heat Transfer, ASME HTD-vol. 203*, pp. 119-127, 1992.
- [84] Kayakol, N., *Discrete Transfer and Discrete Ordinates Methods for Radiative Heat Transfer in Furnaces*, Ph.D. Thesis, METU, Ankara, 1998.
- [85] Jessee, J. P., and Fiveland, W. A., “Bounded, High Resolution Differencing Schemes Applied to the Discrete Ordinates Method”, *ASME HTD-Vol. 325, National Heat Transfer Conference*, vol. 3, pp. 133-141, 1996.
- [86] Liu, F., Becker, H. A., and Pollard, A., “Spatial Differencing Schemes the Discrete Ordinates Method”, *Numerical Heat Transfer, Part B: Fundamentals: An International Journal of Computation and Methodology*, vol. 30, pp. 23-43, 1996.
- [87] Yucel, A., “Solution of the Discrete Ordinates Equations for a Radiatively Participating Medium by the Method of Lines”, *Proceedings of Advances in Computer Methods for Partial Differential Equations VII*, New Brunswick: IMACS, pp. 838-844, 1992.
- [88] Schiesser, W. E., *The Numerical Method of Lines in Integration of Partial Differential Equations*, Academic Press Inc. 1991.
- [89] Saucez, P., Schiesser, W. E., and Wouver, A. V., “Upwinding in the Method of Lines”, *Mathematics and Computers in Simulation*, vol. 56, pp. 171-185, 2001.
- [90] Weiner, R., Schmitt, B.A., and Podhaisky, H., “Rowmap-A Row Code with Krylov techniques for Large Stiff Odes”, *Applied Numerical Mathematics*, vol. 25(2-3), pp. 303-319, 1997.
- [91] Agarwal, B.W., and Menguc, M.P., “Forward and inverse analysis of single and multiple scattering of collimated radiation in an axisymmetric system”, *International Journal of Heat and Mass Transfer*, vol. 34(3), pp. 633-647, 1991.
- [92] Bohren, C.F., and Huffman, D.R., *Absorption and Scattering of Light by Small Particles*, New York: Wiley, 1983.
- [93] Brewster, M.Q., *Thermal Radiative Transfer and Properties*, Wiley, 1992.
- [94] Dombrovsky, L.A., “The use of transport approximation and diffusion-based models in radiative transfer calculations”, *Computational Thermal Sciences*, vol. 4(4), pp. 297-315, 2012.
- [95] Howell, J. R., Siegel R., and Mengüç, M. P., *Thermal Radiation Heat Transfer* (5th ed.). CRC press, 2010.

- [96] van de Hulst, H.C., *Light Scattering by Small Particles*, Dover, 1981.
- [97] Yu, H., Shen, J., and Wei, Y., “Geometrical optics approximation for light scattering by absorbing spherical particles”, *Journal of Quantitative Spectroscopy & Radiative Transfer*, vol. 110, pp. 1178-1189, 2009.
- [98] Granate, P., Coelho, P.J., and Roger, M., “Radiative heat transfer in strongly forward scattering media using the discrete ordinates method”, *Journal of Quantitative Spectroscopy & Radiative Transfer*, vol. 172, pp. 110-120, 2016.
- [99] Boulet, P., Collin, A., and Consalvi, J.A., “On the finite volume method and the discrete ordinates method regarding radiative heat transfer in acute forward scattering media”, *Journal of Quantitative Spectroscopy & Radiative Transfer*, vol. 104, pp. 460-473, 2007.
- [100] Wiscombe, W.J., “The Delta-M Method: Rapid Yet Accurate Radiative Flux Calculations for Strongly Asymmetric Phase Functions”, *Journal of the Atmospheric Sciences*, vol. 34, pp. 1408- 1422, 1977.
- [101] Crosbie, A.L., and Davidson, G.W., “Dirac-Delta Function Approximations to the Scattering Phase Function”, *Journal of Quantitative Spectroscopy & Radiative Transfer*, vol. 33, pp. 391-409, 1985.
- [102] Menguc, M. P., and Viskanta, R., “Radiative Transfer in Three-Dimensional Rectangular Enclosures Containing Inhomogeneous, Anisotropically Scattering Media”, *Journal of Quantitative Spectroscopy & Radiative Transfer*, vol. 33, pp. 533-549, 1985.
- [103] Wiscombe, W.J., and Grams, G.W., “The Backscattered Fraction in Two-Stream Approximations”, *Journal of the Atmospheric Sciences*, vol. 33, pp. 2440-2451, 1976.
- [104] Hunter, B., and Guo, Z., “Conservation of asymmetry factor in phase function discretization for radiative transfer analysis in anisotropic scattering media”, *International Journal of Heat and Mass Transfer*, vol. 55, pp. 1544-1552, 2012.
- [105] Hunter, B., and Guo, Z., “Phase-function normalization for accurate analysis of ultrafast collimated radiative transfer”, *Applied Optics*, vol. 51, pp. 2192-2201, 2012.
- [106] Coelho, P.J., “Advances in the discrete ordinates and finite volume methods for the solution of radiative heat transfer problems in participating media”, *Journal of Quantitative Spectroscopy & Radiative Transfer*, vol. 145, pp. 121-146, 2014.

- [107] Hunter, B., and Guo, Z., “A New and Simple Technique to Normalize the HG Phase Function for Conserving Scattered Energy and Asymmetry Factor”, *Numerical Heat Transfer, Part B: Fundamentals: An International Journal of Computation and Methodology*, vol. 65, pp. 195-217, 2014.
- [108] Mishchenko, M.I., Dlugach, J.M., Yanovitskij, E.G., and Zakharova, N.T., “Bidirectional reflectance of flat, optically thick particulate layers: an efficient radiative transfer solution and applications to snow and soil surfaces”, *Journal of Quantitative Spectroscopy & Radiative Transfer*, vol. 63, pp. 409-432, 1999.
- [109] Hunter, B., and Guo, Z., “Reduction of angle splitting and computational time for the finite volume method in radiative transfer analysis via phase function normalization”, *International Journal of Heat and Mass Transfer*, vol. 55, pp. 2449-2460, 2012.
- [110] Hunter, B., and Guo, Z., “Phase Function Normalization in 3-D Discrete-Ordinates Solution of Radiative Transfer-Part I”, *Numerical Heat Transfer, Part B: Fundamentals: An International Journal of Computation and Methodology*, vol. 62, pp. 203-222, 2012.
- [111] Hunter, B., and Guo, Z., “Phase Function Normalization in 3-D Discrete-Ordinates Solution of Radiative Transfer-Part II”, *Numerical Heat Transfer, Part B: Fundamentals: An International Journal of Computation and Methodology*, vol. 62:4, pp. 223-242, 2012.
- [112] Kozan, M., *Investigation of Radiative Heat Transfer in Freeboard of a 0.3MW_i AFBC Test Rig*, M.Sc. Thesis, METU, Ankara, 1999.
- [113] Harmandar, H., *Effect of Recycling on the Performance of Bubbling Fluidized Bed Combustors*, M.Sc. Thesis, METU, Ankara, 2003.
- [114] Çayan, F. N., and Selçuk, N., “A comparative study of modeling of radiative heat transfer using MOL solution of DOM with gray gas, wide-band correlated-k, and spectral line-based weighted sum of gray gases models” *Numerical Heat Transfer, Part B: Fundamentals*, vol. 52 (3), 231-246, 2007.
- [115] Çayan, F. N., *The Method of Lines Solution of Discrete Ordinates Method for Nongray Media*, M. Sc. Thesis, METU, Ankara, 2006.
- [116] Viskanta, R., Urgan, A., and Menguc, M.P., “Predictions of Radiative Properties of Pulverized Coal and Fly-ash Polydispersions”, *ASME*, No. 81-HT-24, 1981.
- [117] Kırbaş, G., *The Method of Lines Solution of Discrete Ordinates Method for Radiative Heat Transfer in Enclosures*, M. Sc. Thesis, METU, Ankara, 1999.

- [118] Selçuk, N., Kırbaş, G., and Tarhan, T., “Evaluation of Method of Lines Solution of Discrete Ordinates Method and Finite Volume Method in a Planar Medium”, CHMT 99, *Proceedings of International Conference on Computational Heat and Mass Transfer* (Ed. A. A. Mohamad and I. Sezai), Gazimağusa, Northern Cyprus, pp. 358-364, Eastern Mediterranean University Printing House, Gazimağusa, Northern Cyprus, 1999.

APPENDIX A

ORDINATES AND WEIGHTS FOR S_N APPROXIMATION

In this study, S_N angular quadrature scheme was used. The ordinates and weights for various orders of S_N approximation are presented in Table A.1.

Table A.1 Discrete ordinates for the S_N approximation for 3-D geometry

Order of Approximation	Ordinates			Weights
	μ_m	η_m	ξ_m	w_m
S_2	0.5773503	0.5773503	0.5773503	1.5707963
	0.2958759	0.2958759	0.9082483	0.5235987
S_4	0.9082483	0.2958759	0.2958759	0.5235987
	0.2958759	0.9082483	0.2958759	0.5235987
S_6	0.1838670	0.1838670	0.9656013	0.1609517
	0.6950514	0.1838670	0.6950514	0.3626469
	0.1838670	0.6950514	0.6950514	0.3626469
	0.9656013	0.1838670	0.1838670	0.1609517
	0.6950514	0.6950514	0.1838670	0.3626469
	0.1838670	0.9656013	0.1838670	0.1609517
S_8	0.1422555	0.1422555	0.9795543	0.1712359
	0.5773503	0.1422555	0.8040087	0.0992284
	0.1422555	0.5773503	0.8040087	0.0992284
	0.8040087	0.1422555	0.5773503	0.0992284
	0.5773503	0.5773503	0.5773503	0.4617179
	0.1422555	0.8040087	0.5773503	0.0992284
	0.9795543	0.1422555	0.1422555	0.1712359
	0.8040087	0.5773503	0.1422555	0.0992284
	0.5773503	0.8040087	0.1422555	0.0992284
	0.1422555	0.9795543	0.1422555	0.1712359

Table A.1 Discrete ordinates for the S_N approximation for 3-D geometry (cont'd)

Order of Approximation	Ordinates			Weights
	μ_m	η_m	ξ_m	w_m
S_{10}	0.1372719	0.1372719	0.9809754	0.0944411
	0.5046889	0.1372719	0.8523177	0.1483950
	0.1372719	0.5046889	0.8523177	0.1483950
	0.7004129	0.1372719	0.7004129	0.0173701
	0.5046889	0.5046889	0.7004129	0.1149972
	0.1372719	0.7004129	0.7004129	0.0173701
	0.8523177	0.1372719	0.5046889	0.1483950
	0.7004129	0.5046889	0.5046889	0.1149972
	0.5046889	0.7004129	0.5046889	0.1149972
	0.1372719	0.8523177	0.5046889	0.1483950
	0.9809754	0.1372719	0.1372719	0.0944411
	0.8523177	0.5046889	0.1372719	0.1483950
	0.7004129	0.7004129	0.1372719	0.0173701
	0.5046889	0.8523177	0.1372719	0.1483950
	0.1372719	0.9809754	0.1372719	0.0944411
S_{12}	0.1281651	0.1281651	0.9834365	0.0802616
	0.4545003	0.1281651	0.8814778	0.1082299
	0.1281651	0.4545003	0.8814778	0.1082299
	0.6298529	0.1281651	0.7660671	0.0451194
	0.4545003	0.4545003	0.7660671	0.0713859
	0.1281651	0.6298529	0.7660671	0.0451194
	0.7660671	0.1281651	0.6298529	0.0451194
	0.6298529	0.4545003	0.6298529	0.0652524
	0.4545003	0.6298529	0.6298529	0.0652524
	0.1281651	0.7660671	0.6298529	0.0451194
	0.8814778	0.1281651	0.4545003	0.1082299
	0.7660671	0.4545003	0.4545003	0.0713859
	0.6298529	0.6298529	0.4545003	0.0652524
	0.4545003	0.7660671	0.4545003	0.0713859
	0.1281651	0.8814778	0.4545003	0.1082299
	0.9834365	0.1281651	0.1281651	0.0802616
	0.8814778	0.4545003	0.1281651	0.1082299
	0.7660671	0.6298529	0.1281651	0.0451194
0.6298529	0.7660671	0.1281651	0.0451194	
0.4545003	0.8814778	0.1281651	0.1082299	
0.1281651	0.9834365	0.1281651	0.0802616	

APPENDIX B

CALCULATION OF ABSORPTION COEFFICIENT OF GASES USING LECKNER'S CORRELATIONS

Absorption coefficient of gases in the medium of the enclosure is calculated from Equation 3.1 in which gas emissivity, κ_g , is estimated by Leckner's correlations [35] given as:

$$\varepsilon_a(p_a L, p = 1\text{bar}, T_g) = \exp \left[\sum_{i=0}^M \sum_{j=0}^N c_{ji} \left(\frac{T_g}{T_0} \right)^j \left(\log_{10} \frac{p_a L_m}{(p_a L)_0} \right)^i \right] \quad (\text{B.1})$$

where $a = \text{H}_2\text{O}$ or CO_2 , T_g is the gas temperature, p_a is partial pressure of radiating gas (CO_2 or H_2O), L_m is the mean beam length and c_{ji} are correlation constants given in Table B.1 for water vapor and carbon dioxide.

Total emissivity of gas mixture is obtained from:

$$\varepsilon_g = \varepsilon_{\text{CO}_2} + \varepsilon_{\text{H}_2\text{O}} - \Delta\varepsilon \quad (\text{B.2})$$

where $\Delta\varepsilon$ represents overlap correction factor and expressed by

$$\Delta\varepsilon = \left[\frac{\zeta}{10.7 + 101\zeta} - 0.0089\zeta^{10.4} \right] \left(\log_{10} \frac{(p_{\text{H}_2\text{O}} + p_{\text{CO}_2}) L_m}{(p_a L)_0} \right)^{2.76} \quad (\text{B.3})$$

where

$$\zeta = \frac{p_{\text{H}_2\text{O}}}{p_{\text{H}_2\text{O}} + p_{\text{CO}_2}} \quad (\text{B.4})$$

Table B.1 Leckner's correlation constants for water vapor and carbon dioxide [35]

Gas	Water Vapor	Carbon Dioxide
M,N	2,2	2,3
C_{00}	-2.2118	-3.9893
C_{N0}	-1.1987	2.7669
\vdots		
C_{0M}	0.85667	-1.1090
\vdots	0.93048	1.2710
C_{NM}	-0.17156	-0.23678
\vdots		
	0.035596	0.19731
	-0.14391	-2.1081
	0.045915	1.0195
		-0.19544
		0.39163
		-0.21897
		0.044644
$T_0 = 1000\text{K}$ $(p_a L)_0 = 1\text{barcm}$		

APPENDIX C

TABULATED SIZE DISTRIBUTIONS OF SOLID STREAMS

Table C.1 Size distribution of cyclone ash of test case 1 [113]

ASTM Mesh #	Sieve Opening, mm	Differential Weight, %	Cumulative Weight, %
12	1.7000	0.00	0.00
14	1.4000	0.00	0.00
16	1.1800	0.00	0.00
18	1.0000	0.00	0.00
20	0.8500	0.00	0.00
25	0.7100	0.37	0.37
30	0.6000	0.64	1.01
	0.4925	5.21	6.21
	0.4042	3.37	9.58
	0.3318	2.05	11.63
	0.2723	1.64	13.27
	0.2235	2.17	15.44
	0.1834	3.44	18.88
	0.1506	4.95	23.83
	0.1236	6.20	30.02
	0.1014	7.03	37.05
	0.0833	7.40	44.46
	0.0683	7.33	51.78
	0.0561	6.84	58.62
	0.0460	6.18	64.80
	0.0378	5.50	70.30
	0.0310	4.91	75.21
	0.0255	4.41	79.62
	0.0209	3.92	83.54
	0.0172	3.43	86.97
	0.0141	2.93	89.90
	0.0116	2.44	92.34
	0.0095	1.95	94.29
	0.0078	1.50	95.79
	0.0064	1.11	96.90
	0.0052	0.76	97.66
	0.0043	0.49	98.16
	0.0035	0.35	98.51
	0.0029	0.30	98.80
	0.0024	0.30	99.10
	0.0020	0.32	99.42
	0.0016	0.30	99.71
	0.0013	0.21	99.92
	0.0005	0.08	100.00

Table C.2 Size distribution of baghouse filter ash of test case 1 [113]

Sieve Opening, mm	Differential Weight, %	Cumulative Weight, %
0.4925	0.00	0.00
0.4042	0.00	0.00
0.3318	0.00	0.00
0.2723	0.00	0.00
0.2235	0.00	0.00
0.1834	0.00	0.00
0.1506	0.00	0.00
0.1236	0.00	0.00
0.1014	0.02	0.02
0.0833	0.07	0.09
0.0683	0.15	0.24
0.0561	0.26	0.50
0.0460	0.37	0.87
0.0378	0.47	1.34
0.0310	0.62	1.96
0.0255	0.85	2.81
0.0209	1.21	4.02
0.0172	1.71	5.73
0.0141	2.35	8.08
0.0116	3.20	11.28
0.0095	4.30	15.58
0.0078	5.60	21.18
0.0064	6.97	28.15
0.0052	8.18	36.33
0.0043	9.12	45.45
0.0035	9.91	55.36
0.0029	10.48	65.84
0.0024	10.58	76.42
0.0020	9.83	86.25
0.0016	7.91	94.16
0.0013	4.84	99.00
0.0005	1.00	100.00

Table C.3 Size distribution of cyclone ash of test case 2 [113]

ASTM Mesh #	Sieve Opening, mm	Differential Weight, %	Cumulative Weight, %
12	1.7000	0.00	0.00
14	1.4000	0.00	0.00
16	1.1800	0.00	0.00
18	1.0000	0.00	0.00
20	0.8500	0.00	0.00
25	0.7100	0.53	0.53
30	0.6000	0.65	1.18
	0.4925	6.24	7.41
	0.4042	3.81	11.23
	0.3318	2.12	13.35
	0.2723	1.53	14.89
	0.2235	2.04	16.92
	0.1834	3.43	20.35
	0.1506	5.20	25.55
	0.1236	6.76	32.31
	0.1014	7.93	40.23
	0.0833	8.62	48.85
	0.0683	8.75	57.60
	0.0561	8.25	65.85
	0.0460	7.36	73.21
	0.0378	6.30	79.51
	0.0310	5.19	84.70
	0.0255	4.12	88.82
	0.0209	3.15	91.98
	0.0172	2.30	94.28
	0.0141	1.61	95.89
	0.0116	1.10	96.99
	0.0095	0.72	97.71
	0.0078	0.46	98.17
	0.0064	0.31	98.48
	0.0052	0.21	98.69
	0.0043	0.16	98.84
	0.0035	0.15	98.99
	0.0029	0.17	99.16
	0.0024	0.21	99.37
	0.0020	0.23	99.59
	0.0016	0.21	99.80
	0.0013	0.15	99.95
	0.0005	0.05	100.00

Table C.4 Size distribution of baghouse filter ash of test case 2 [113]

Sieve Opening, mm	Differential Weight, %	Cumulative Weight, %
0.4925	0.00	0.00
0.4042	0.00	0.00
0.3318	0.00	0.00
0.2723	0.00	0.00
0.2235	0.00	0.00
0.1834	0.00	0.00
0.1506	0.00	0.00
0.1236	0.00	0.00
0.1014	0.00	0.00
0.0833	0.00	0.00
0.0683	0.00	0.00
0.0561	0.12	0.12
0.0460	0.45	0.57
0.0378	1.01	1.58
0.0310	1.87	3.45
0.0255	3.05	6.50
0.0209	4.43	10.93
0.0172	5.87	16.80
0.0141	7.07	23.87
0.0116	7.95	31.82
0.0095	8.42	40.24
0.0078	8.49	48.73
0.0064	8.22	56.95
0.0052	7.60	64.55
0.0043	6.84	71.39
0.0035	6.20	77.59
0.0029	5.74	83.33
0.0024	5.34	88.67
0.0020	4.76	93.43
0.0016	3.77	97.20
0.0013	2.31	99.51
0.0005	0.49	100.00

APPENDIX D

CALCULATION OF PARTICLE REFLECTIVITY USING FRESNEL'S RELATIONS

Absorption and scattering efficiencies of the fly ash particles in the medium can be calculated from Equation 3.32 and 3.33 in which reflectivity, ρ , is estimated by using Fresnel's relations [35]. By using complex index of refraction at spectral range of interest, required variables to yield reflectivity, p and q , can be calculated as

$$p^2 = \frac{1}{2} \left[\sqrt{(n_2^2 - k_2^2 - n_1^2 \sin^2 \theta)^2 + 4n_2^2 k_2^2} + (n_2^2 - k_2^2 - n_1^2 \sin^2 \theta) \right] \quad (D.1)$$

$$q^2 = \frac{1}{2} \left[\sqrt{(n_2^2 - k_2^2 - n_1^2 \sin^2 \theta)^2 + 4n_2^2 k_2^2} - (n_2^2 - k_2^2 - n_1^2 \sin^2 \theta) \right] \quad (D.2)$$

After determining the required variables, p and q , correlation for directional-hemispherical reflectivity is as follows:

$$\rho = \frac{\rho_{\parallel} + \rho_{\perp}}{2} \quad (D.3)$$

where ρ_{\perp} and ρ_{\parallel} are expressed by

$$\rho_{\perp} = \frac{(n_1 \cos \theta - p)^2 + q^2}{(n_1 \cos \theta + p)^2 + q^2} \quad (D.4)$$

$$\rho_{\parallel} = \frac{(p - n_1 \sin\theta \tan\theta)^2 + q^2}{(p + n_1 \sin\theta \tan\theta)^2 + q^2} \rho_{\perp} \quad (\text{D.5})$$

In GOA3 calculations, reflectivity over all directions are calculated by numerically integrating Equation D.3. Integration is performed with 1° intervals between 0-180°.

APPENDIX E

SCATTERING REGIME MAP FOR INDEPENDENT AND DEPENDENT SCATTERING

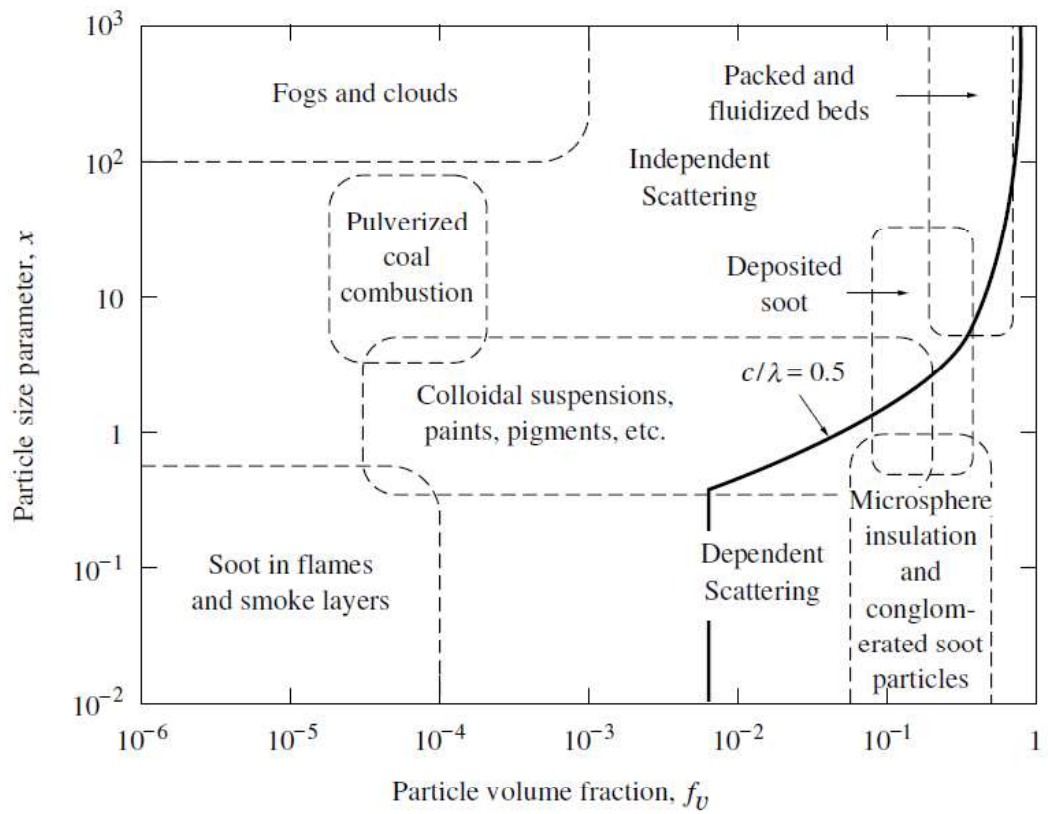


Figure E.2 Scattering regime map for independent and dependent scattering [35]

APPENDIX F

INITIAL PARAMETERS FOR THE ODE SOLVER (ROWMAP) SUBROUTINE

The radiation code extended in this study require specifications of certain input parameters for the ODE solver subroutine in addition to the input data relevant with the physical system and subdivisions of angular and spatial domains which are presented in the text. Initial parameters for the ODE solver are the absolute and relative error tolerances (ABSERR and RELERR), time interval for printing (TP), and convergence criteria for terminating the integration. Table F.1 presents the input parameters utilized to obtain solutions for the system under consideration.

Table F.1 Initial parameters utilized for ROWMAP subroutine for the system under consideration

Test Case	ABSERR	RELERR	TP	ϵ
1	0.001	0.001	1.0	0.01
2	0.001	0.001	1.0	0.01